Shape coexistence and shape evolution of neutron-deficient bismuth nuclei

Christopher Keith Raison

Doctor of Philosophy

University of York

Physics

July 2020

Abstract

The neutron-deficient lead region contains the most well known examples of shape coexistence, to this day. As a result, this part of the Segrè chart has been subject to extensive laser spectroscopy studies. In this thesis, the results from the in-source laser spectroscopy investigation of neutron-deficient Bi isotopes, taken at the ISOLDE, CERN facility, will be presented.

During this experiment the hyperfine structures and isotope shifts of short lived α-decaying states in $^{187-189,191}$Bi were measured with the changes in mean-square charge radius and electromagnetic moments extracted for each nuclear state. These charge radii values reveal that unlike the early interpretation that the $9/2^-$ ground states are spherical in the odd-A Bi nuclei, a trend towards a weakly deformed ground state was observed in ^{187,189,191}Bi. This is in contrast to the ground states of the Tl isotopes, which follow the near spherical trend of the Pb nuclei. The most spectacular result from this investigation was the strong shape staggering observed between the high-spin and low-spin isomeric states of ^{188}Bi. This indicates that the low-spin isomer is much more deformed in shape in comparison to both the high-spin isomer in ^{188}Bi and the $9/2^-$ ground states of the neighbouring isotopes ^{187,189}Bi. This observation implies a large difference in the structure of states in odd-odd and odd-A Bi nuclei near the N=104 midshell. This staggering effect between ^{188ls}Bi and ^{187gs,188hs,189gs}Bi resembles the long known staggering seen in the mercury isotopes $^{181-185}$Hg, with both starting at the same neutron number (N=105). In 2018, Monte Carlo Shell Model calculations were used to confirm the underlying proton and neutron configurations responsible for the shape staggering in the Hg isotopes. It was found that the shape staggering is correlated with the staggering in the shell-model states occupation. It is thought that these configurations are also producing this staggering effect in the Bi chain.

Contents

List of Tables

List of Figures

Acknowledgements

During my time as a PhD student I have had a great chance to work with amazing people and lifelong friends. The list I need to thank is rather long so I will try my best to summarise.

Firstly, Andrei, my supervisor, for your patience and expert guidance throughout the project, as well as the amazing opportunities throughout my PhD project. The travels to experiments, conferences and meetings were very insightful from an educational standpoint as well as experiencing other countries. Your devotion and strong work ethic is a credit to all at the ISOLDE collaboration and I wish you well for the future!

Anatoly at Gatchina, thank you for taking your time to thoroughly read my thesis and explain the fundamental physics. Both your and Maxim's input was essential for the final analysis of the project.

My colleagues at ISOLDE. Special thanks to both James Cubiss and Boris Andel for their help throughout the PhD project with both the use of the ROOT analysis code and helping to develop my practical skills at ISOLDE, hope you keep up the cycling James!

The nuclear group at York. I'd like to thank both Luke Morris and Ryan Llewellyn for helping me out lots in the past four years. The socials were great fun.

Declaration

I declare that this thesis is a presentation of original work and I am the sole author. This work has not previously been presented for an award at this, or any other, University. All sources are acknowledged as References.

Chapter 1

Introduction

The atomic nucleus, being a many body quantum system, is a somewhat difficult object to characterize. Amongst the multiple complications is the nuclear shape, a property of paramount importance since it defines the potential which binds the nucleons housed within it, thus also determining the half lives and decay modes of each nuclear state. The "magic" numbers are the numbers of protons or neutrons needed to make a closed valence shell, akin to electrons in an atom producing a noble gas. The initial postulation of a spherical shape holds true only for nuclei which possess these "magic" numbers of protons and neutrons (e.g. ^{16}O with N,Z=8 and ^{40}Ca with N,Z=20). However, there are exceptions to the rule in singly magic nuclei (magic N or Z, but not both), including the island of inversion at N=20 (^{32}Mg), where due to intruder configurations appearing at low excitation energies, the ground state becomes deformed [1]. Quadrupole deformation provides us with a measure of the deformation of the nuclear charge distribution. Venturing further away from the magic numbers, many nuclei have some level of quadrupole deformation, as can be seen in Fig. 1.1.

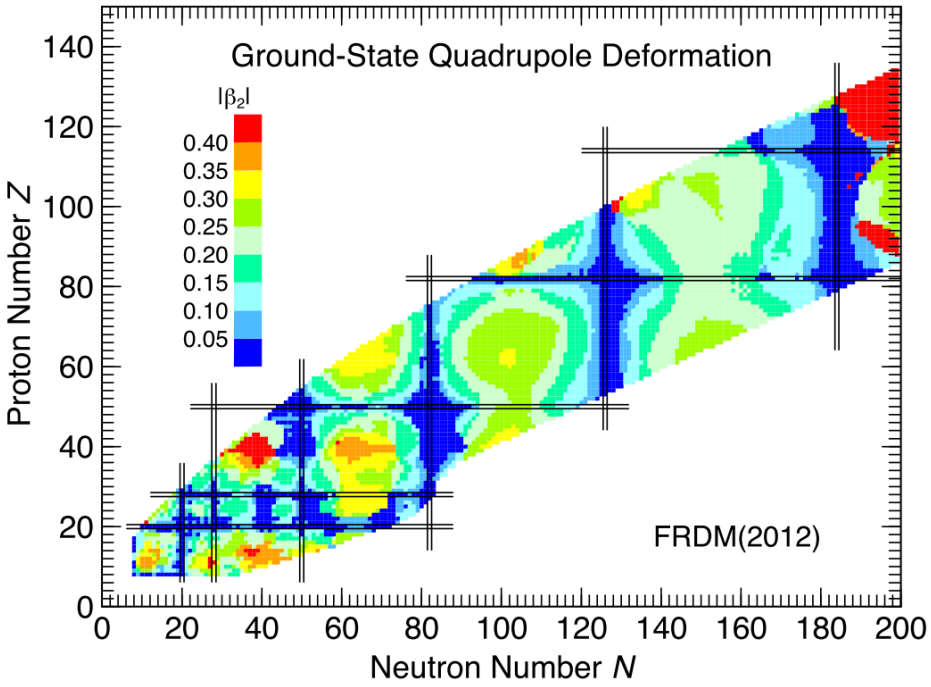

Figure 1.1: Ground state quadrupole deformation (shown with deformation parameter, β_2) of all nuclei below N=200, with black lines indicating major shell closure for protons and neutrons. Figure taken from [2].

Besides nuclear deformation, is another phenomenon known as shape coexistence. This effect, is the ability of different states with various shapes to exist at low excitation energies within the same nucleus. This was first observed in 1956 in ^{16}O [3], when a rotational band was found. Since its initial discovery, shape coexistence has been observed in multiple regions of the nuclear chart. A recent review in 2011 by Heyde and Wood coined it as occurring in all except the lightest of nuclei as well as its understanding being one of the greatest challenges for nuclear theorists to date [4].

This work in this document represents part of a long campaign of laser spectroscopy studies at ISOLDE which aims to probe nuclear deformation and shape coexistence in and around the Z=82 shell closure. To this day, this region of the nuclear chart displays the largest array of shape coexistence [4, 5, 6]. The experiment, IS608, made use of the CERN ISOLDE facility in 2016 and 2017, utilising α-decay tagged in-source laser spectroscopy. The intent of this investigation was to measure the hyperfine structure and isotope shifts of neutron-deficient Bi isotopes in order to determine their respective electromagnetic moments

and change in mean-square charge radius. This thesis will present the results and outcomes of this investigation.

Chapter 2

Nuclear models

When one tries to model the nucleus, several fundamental difficulties arise. One of the major obstacles being due to the nucleus being a complicated many-body quantum system, consisting of protons and neutrons (collectively known as nucleons). Another major issue arises due to the not yet fully understood nucleon-nucleon potential, and even for light nuclei, one needs to consider many-body forces. These challenges have resulted in no theory to date being able to describe the nuclear properties universally across the nuclear chart. Instead, one constructs a nuclear model by selecting a simplified theory. If this theory can successfully describe some nuclear properties, it can then be improved by adding additional terms. This section of the thesis describes some of these well-known models as well as their impact on the field.

2.1 Liquid drop and droplet model

The Liquid Drop Model (LDM) is a macroscopic model used to describe multiple nuclear properties. In this approach, the nucleus is considered to behave like an incompressible liquid drop, with uniform nucleon density and a sharp radius given by:

$$r = r_0 A^{1/3} \tag{2.1}$$

where A is the number of nucleons and r_0 is a constant derived from experimental data, typically given as 1.2 fm. A major outcome of the LDM was the reproduction of the experimental trend in binding energies of nuclei, B(Z,N), when the Bethe-Weiszacker formula was produced

in 1935 [7]. The latter is used to calculate the binding energy of a nucleus and is given as:

$$B(Z,N) = a_v A - a_s A^{2/3} - a_c \frac{Z(Z-1)}{A^{1/3}} - a_{sym} \frac{(A-2Z)^2}{A} + \delta(A,Z) \tag{2.2}$$

This equation has 5 terms, the nuclear volume term (a_v), surface term (a_s), Coulomb term (a_c), symmetry term (a_{sym}) and the pairing term δ. The volume term accounts for the attractive nature of the strong nuclear force which acts on both protons and neutrons. The surface term is a correction for the volume term as the nucleons close to the surface have less neighbouring nucleons, thus reducing the binding energy. The repulsive Coulomb force further reduces the binding energy and the asymmetry term favours nuclei which have an equal number of protons and neutrons in contrast to nuclei with a large proton-neutron asymmetry. The pairing term adds to the binding energy for even-even nuclei, has no contribution for odd-A nuclei, and reduces the binding energy for odd-odd isotopes.

The Droplet Model (DM) is a refinement to the LDM, with a fundamental modification. In this model, the nucleon density distribution is no longer considered constant. As a result, instead of a sharp boundary, there is a diffuse surface region at the edge of the nucleus in which the nucleon densities reduce smoothly to zero [8]. It is important to note that both the LDM and DM are macroscopic models. As such, calculations from these two models can only reproduce with some precision global trends such as the binding energy of the nucleus. In order for one to obtain a more detailed description of the nucleus, the introduction of the shell correction is necessary. This is done in the nuclear shell model, which is discussed in detail in section 2.2.

2.2 The spherical shell model

Just like an atom has electronic energy levels, nuclei display characteristics of a shell-like structure for the ordering of their nucleons. Experimental evidence to support this was the measured proton and neutron separation energies shown in Fig. 2.1. One can clearly see that the two-proton (S_{2p}) and two-neutron (S_{2n}) separation energies increase steadily with Z and N, respectively except for sharp drops which occur at the specific proton and neutron numbers. These sharp discontinuities correspond to the filling of major shells, the so called

'magic numbers' (Z or N = 2, 8, 20, 28, 50, 82 and 126) which represent the filling of major shells.

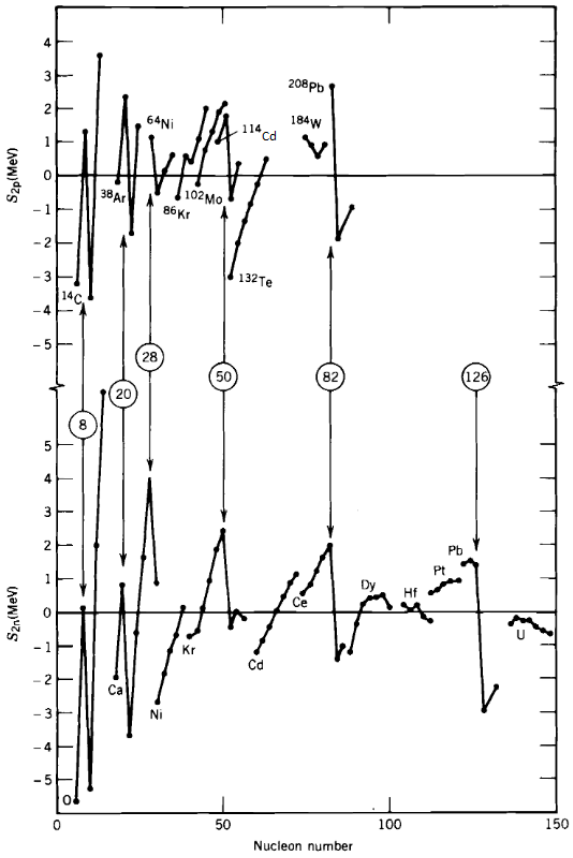

Figure 2.1: (Top) Two-proton separation energies of different isotones, with the lightest isotope noted by its mass and element symbol. (Bottom) Two-neutron separation energies of different sequences of isotopes. Figure taken from [9].

The first step in the development of the shell model was the choice of the potential which binds the constituent nucleons. This potential is important as it determines the ordering of the nucleon states, therefore defining properties such as electromagnetic moments and spin. A good first approximation, is the Woods-Saxon potential $V_N(r)$, which is given by:

$$V_N(r) = \frac{-V_0}{1 + \exp(\frac{r - r_{sph}}{a})} \tag{2.3}$$

where V_0 is the well depth (typically around 50 MeV), r is the distance from the centre of the nucleus, r_{sph} is the nuclear radius given by equation 2.1 and a is the nuclear diffuseness with a typical value of a=0.524 fm. As the nucleons are fermions, they fill states within the nucleus in accordance with the Pauli exclusion principle, meaning no two identical nucleons

can occupy the same quantum state simultaneously. The states nucleons may occupy are labelled by quantum numbers, nl, where n is an integer giving the order of the state with an orbital angular momentum, l, which is an integer relating to the spectroscopic notation by:

$$l = 0, 1, 2, 3...s, p, d, f \tag{2.4}$$

these states have a degeneracy $2(2l+1)$. The use of this Woods-Saxon potential produces the magic numbers 2, 8 and 20, but the higher numbers are not reproduced. It was not until 1949 that it was shown that the addition of the spin-orbit potential produces the magic numbers [10]. The spin-orbit potential, $V_{l\cdot s}$, arises due to the coupling of the intrinsic spin of the individual nucleon and its orbital angular momentum. $V_{l\cdot s}$ is defined as the derivative of the nuclear potential:

$$V_{l\cdot s} = -V_{ls}\frac{\partial V_N(r)}{\partial r}\mathbf{l}\cdot\mathbf{s} \tag{2.5}$$

where $V_N(r)$ is the Woods-Saxon potential, V_{ls} is a strength constant and s is the intrinsic angular momentum of each nucleon ($s = 1/2$). Due to the presence of the spin-orbit interaction, states with $l > 0$ are split into two states, denoted by the total spin quantum number ,j, $\mathbf{j} = \mathbf{l} + \mathbf{s}$. This gives the possible values of $\mathbf{j}$ as $j = l + 1/2$ and $j = l - 1/2$, of which the former is lowered in energy and the latter is raised. Since the energy splitting between these two levels is proportional to $(2l + 1)$, a higher degree of splitting occurs for states with large values of l. It is this splitting effect which results in the reordering of the states such that the shell closures occur at the correct magic numbers. This can be seen in Fig. 2.2.

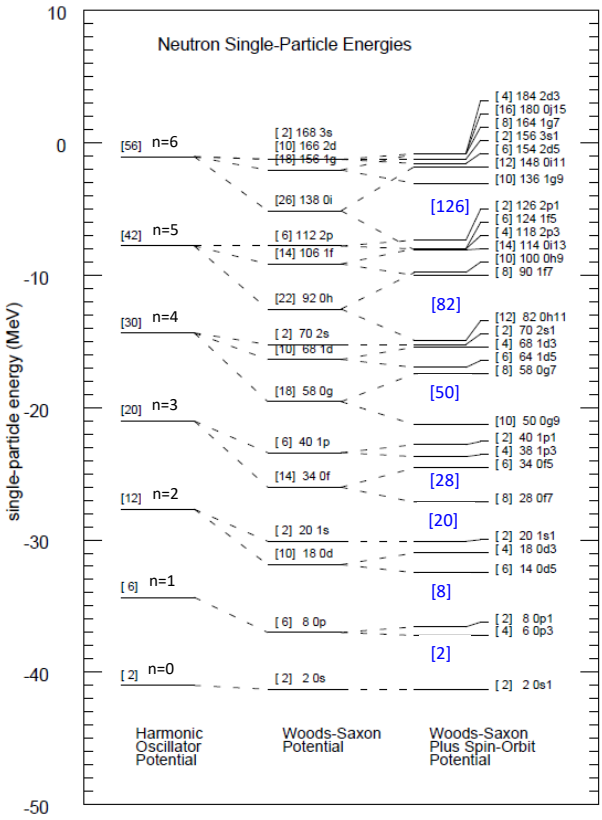

Figure 2.2: Single-particle energy levels. The states on the left are the solutions for a harmonic oscillator potential and are labelled with the quantum number n. The states in the middle are the solutions for a Woods-Saxon potential and are labelled with the n,l quantum numbers. The levels on the right are for the Woods-Saxon plus the spin-orbit term and are labelled with quantum numbers $n,l,2j$, reproducing the magic numbers, shown in blue. Figure taken from [9].

However, in order to produce the total nuclear potential, two other additional terms are required. Firstly, the centrifugal term, which accounts for the force the nucleons feel due to their orbital motion, acting like a potential which keeps them away from the origin when $l > 0$. It is written as:

$$V_{cent}(r) = \frac{l(l+1)\hbar^2}{2mr^2} \tag{2.6}$$

with m being the reduced mass of the system. Lastly, due to the repulsive nature of the Coulomb force, each proton experiences a Coulomb potential ($V_{coul}(r)$). If we consider the nucleus as a sphere of radius R, and charge Ze, we can approximate the Coulomb potential

as:

$$V_{coul}(r) = \begin{cases} \frac{Ze^2}{r}, & \text{for r>R,} \\ \frac{Ze^2}{2R}\left[3 - \frac{r^2}{R^2}\right], & \text{for r<R,} \end{cases} \tag{2.7}$$

Thus the total potential experienced by the protons can be written as:

$$V_{total,protons} = V_N(r) + V_{l\bullet s}(r) + V_{cent}(r) + V_{coul}(r) \tag{2.8}$$

and for neutrons:

$$V_{total,neutrons} = V_N(r) + V_{l\bullet s}(r) + V_{cent}(r) \tag{2.9}$$

Fig. 2.3 shows the form of each of these individual components as well as the summed potential for protons.

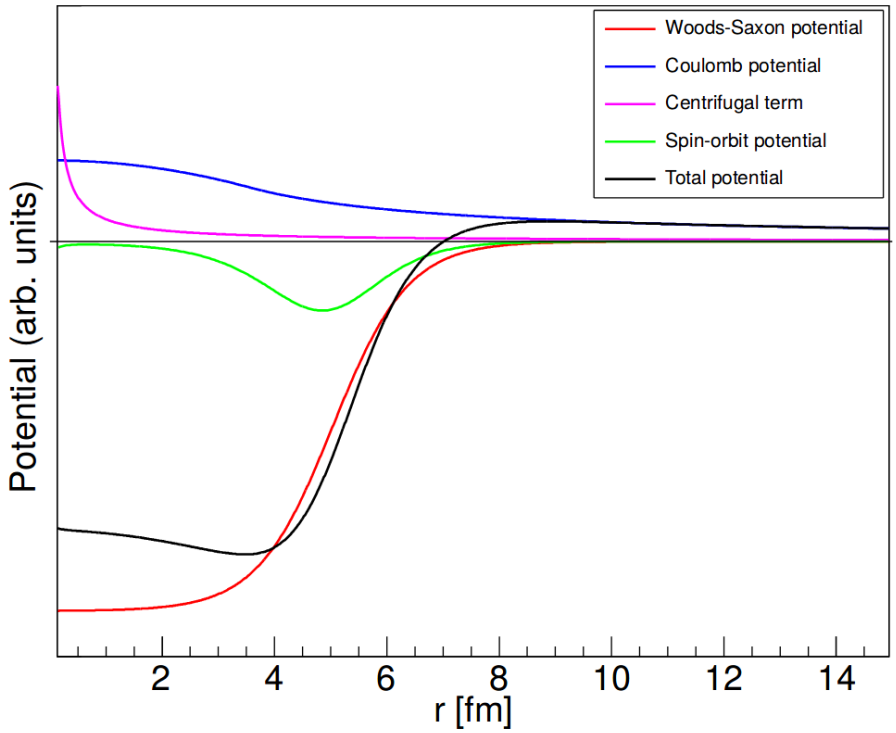

Figure 2.3: Plots of the Woods-Saxon(red), spin-orbit interaction (green), Coulomb (blue) and Centrifugal (pink) potential terms from equation 2.7 and the combined potential (black as a function of distance from the centre of the nucleus (r). Potentials are not to scale. Figure taken from [11].

2.3 The Nilsson model

The spherical shell model can describe many features of spherical nuclei. However, moving away from the magic numbers, nuclei can possess some level of deformation and the spherical shell model fails at reproducing the properties of such nuclei. By relaxing the constraint on the nuclear shape, it is possible to describe the motion of single particles in a deformed potential. The first example of such calculations was carried out by Nilsson in 1955 [12]. Since then, the Nilsson model has proven very successful at describing a large number of deformed nuclei across the Segre chart.

The Nilsson model modifies the nuclear potential by introducing quadrupole deformation. Unlike spherical nuclei, the potential each nucleon experiences has a dependency upon the orientation of the orbit. The degree of quadrupole deformation is determined from the quadrupole deformation parameter, β_2, given by:

$$\beta_2 = \frac{4}{3}\sqrt{\frac{\pi}{5}}\frac{\Delta R}{r_{sph}} \tag{2.10}$$

where ΔR is the difference between the semi-major and semi-minor axes and r_{sph} is the radius of a spherical liquid drop nucleus, determined using Eqn. 2.1. Nuclear shapes with $\beta_2 = 0$, $\beta_2 < 0$ and $\beta_2 > 0$ are known as spherical, oblate and prolate shapes as shown in figure 2.4.

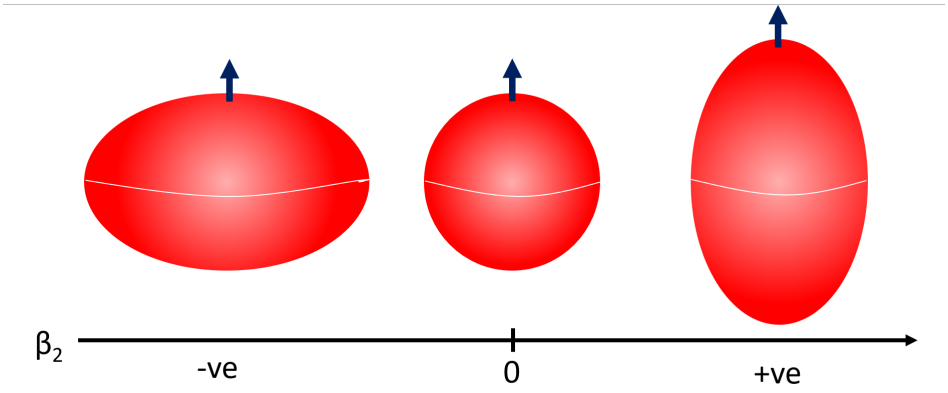

Figure 2.4: Schematic representation of the different spheroidal geometries as a function of the quadrupole deformation parameter, β_2.

The magnitude and direction of the shift in the energy levels is dependent upon the orientation of the orbit relative to the deformed core. Some orbits will have a greater overlap,

resulting in a stronger interaction and hence a reduction in the energy level due to the particle being more tightly bound. In contrast, particles occupying states with a small overlap with the core have a weaker interaction, and so are less tightly bound, resulting in an increase in the energy of the orbit. Figs. 2.5 and 2.6 show the Nilsson diagrams for the region of the nuclear chart where the Bi isotopes lie. These diagrams reveal the position of the single particle energy levels with respect to the deformation parameter ε_2. This parameter relates to the β_2 quadrupole deformation according to the equation:

$$\beta_2 = \sqrt{\frac{\pi}{5}}\left[\frac{4}{3}\varepsilon_2 + \frac{4}{9}\varepsilon_2^2 + \frac{4}{27}\varepsilon_2^3 + ...\right] \tag{2.11}$$

and is approximately equal to β_2 for large deformations. In a spherical nucleus, the energy levels of every single particle state have a degeneracy of $2j + 1$. However, for a deformed potential the energy levels are now dependent upon the orbit's spatial orientation, resulting in a degeneracy of 2. A Nilsson orbit is labelled with the following quantum numbers:

$$\mathrm{K}\,[Nn_z\Lambda] \tag{2.12}$$

where K is the projection of j along the symmetry axis, N is the principal quantum number denoting the major shell, n_z is the number of wavefunction nodes along the symmetry axis and Λ is the angular momentum projection along the symmetry axis.

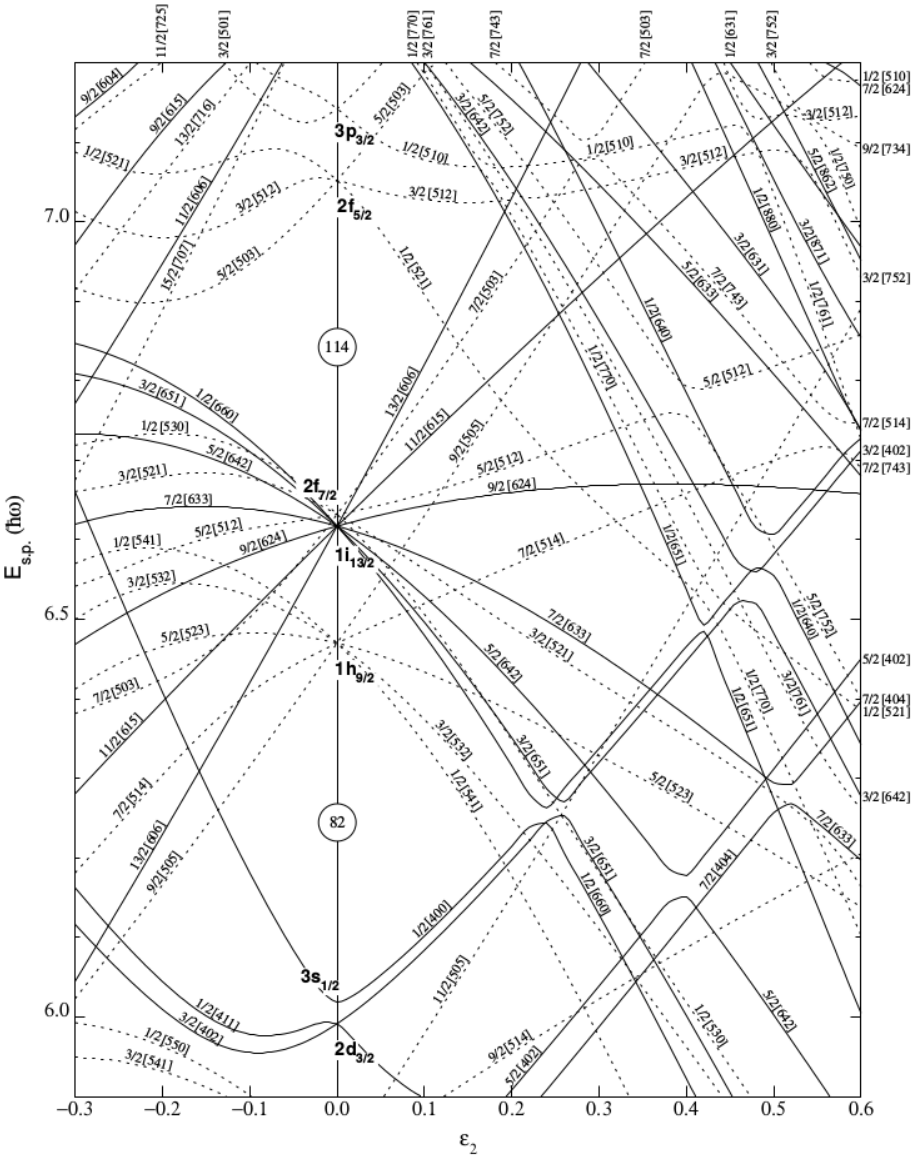

Figure 2.5: Nilsson model single particle energies for protons in nuclei in the vicinity of Z=82, as a function of the deformation parameter, ε_2. The solid and dashed lines correspond to positive and negative parity states, respectively [13].

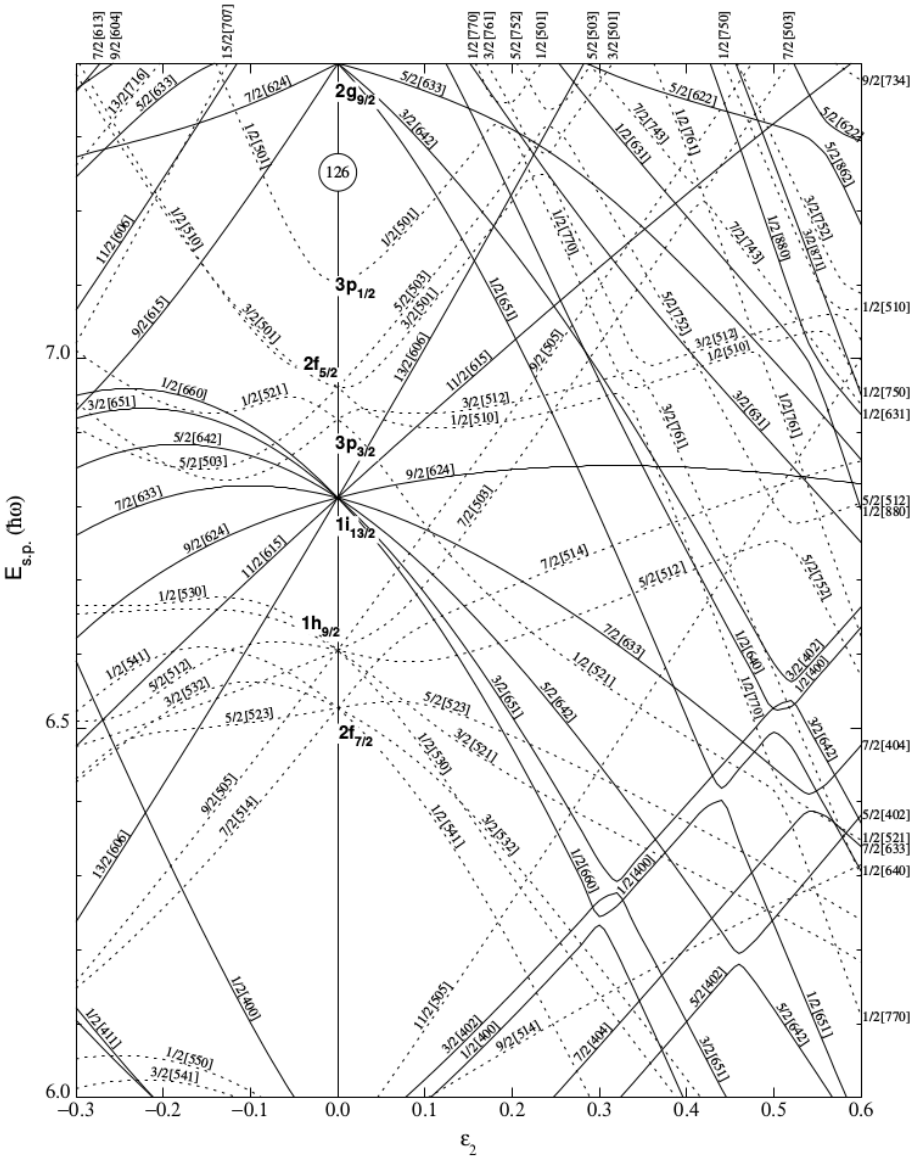

Figure 2.6: Nilsson model single particle energies for neutrons in nuclei with 82<N<126, as a function of the deformation parameter, ε_2. The solid and dashed lines correspond to positive and negative parity states, respectively [13].

2.4 Probing nuclear structure

Knowledge of the structure of a given nucleus can be gained by measuring quantities such as its electromagnetic moments and charge radius. In order to extract such measurements, we rely on multiple nuclear properties. One of these is to observe the nucleus decaying. This section summarises the different decay processes which can be used to measure the atomic hyperfine structure.

Alpha decay

Alpha decay is the spontaneous emission of an $^4_2$He nucleus from a parent nucleus. The process can be represented by the following equation:

$$ {}^{A}_{Z}X_N \rightarrow {}^{A-4}_{Z-2}X'_{N-2} + {}^{4}_{2}He, \tag{2.13} $$

Alpha emission arises due to the repulsive Coulomb force. As the number of protons increases, the Coulomb force increases with Z^2, with the attractive nuclear force increasing linearly with A. As a result, for heavier nuclei (typically $A \geq 150$), the Coulomb force is stronger than the nuclear force and so α decay is typically observed in heavier neutron deficient nuclei(β-decay is a competing process, discussed in Section. 2.5). The α particle, due to its tightly bound stable structure (doubly magic $^4_2$He nucleus), has a relatively small mass compared with the mass of its separate constituents. This keeps the disintegration products as light as possible, thus getting the largest possible release of kinetic energy. The total energy released in α emission (Q_α) is given by:

$$ Q_\alpha = (m_X - m_{X'} - m_\alpha)c^2 = E_\alpha + E_{X'} \tag{2.14} $$

where m_X and $m_{X'}$ are the atomic masses of the parent and daughter nuclei respectively, m_α is the atomic mass of the α particle, E_α and $E_{X'}$ are the kinetic energies of the α particle and daughter nucleus respectively. α decay occurs only if $Q_\alpha > 0$. Using the conservation of momentum and non-relativistic kinematics, the kinetic energy of the α particle can be written in terms of Q_α:

$$ E_\alpha = \frac{Q_\alpha}{1 + \dfrac{m_\alpha}{m_{X'}}} \tag{2.15} $$

typically, the α particle carries 98% of the energy released (thus the recoil energy is not entirely negligible). In addition to the requirement that $Q_\alpha > 0$, α decay also obeys angular

momentum and parity selection rules. The α particle consists of two protons and two neutrons all in 1s states with each of their spins coupling to zero. The spin of the α particle is therefore zero, and the total angular momentum carried away by the α particle is purely orbital. The range of values of orbital angular momentum of an α particle, l_α from an initial nuclear state I_i, to a final state I_f, is given by:

$$|I_i - I_f| \leq l_\alpha \leq I_i + I_f \tag{2.16}$$

The change in parity associated with α decay is $(-1)^{l_\alpha}$. The theory which accounted for the systematics of the variation in Q_α-value with half life was developed by George Gamow in 1928 [14]. This theory is based on the idea that the α particle 'preforms' inside the nucleus, with an energy of Q_α. Fig. 2.7 shows the expected variation of the potential energy of the α particle daughter nucleus system as a function of separation r. Quantum mechanically, it is possible for the α particle to tunnel through the potential barrier. The barrier penetration probability (P) is dependent upon the decay energy, Q_α, the barrier height B and the thickness of the barrier. The α particle bounces backwards and forwards inside the nucleus, colliding with the barrier. The transition probability is then written as the product of the barrier penetration probability (P) and frequency of collision with the barrier (f):

$$\lambda = f \cdot P \tag{2.17}$$

The values of half lives determined from the Gamow theory have qualitative agreement with the experimental data, with experimental half lives typically being 10-100 times longer. This so called "hindrance" is caused predominantly by the probability of the wavefunction of the parent nucleus overlapping with the wavefunction representing both the α particle and daughter nucleus. When there is no change in orbital angular momentum between the initial and final nuclear states ($l_\alpha = 0$), the wavefunctions overlap. Such decays are referred to as 'unhindered'. Changes in orbital angular momentum result in less overlap between the two wavefunctions. These are 'unhindered' decays, which have a lower transition probabilty.

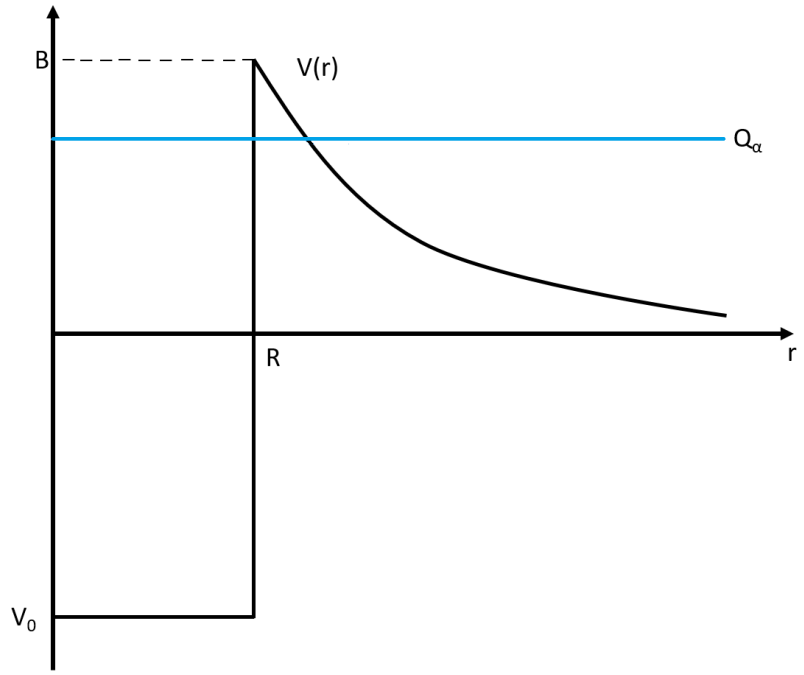

Figure 2.7: Relative potential energy of the α-particle, daughter-nucleus system as a function of their separation, r. Inside the nuclear surface (r<R), the potential is represented by a square well. Beyond the nuclear surface (r>R), only the coulomb repulsion operates. The α particle tunnels through the Coulomb barrier.

2.5 Beta decay

The most common form of radioactive disintegration is β decay, which occurs in isotopes of all elements. The term β decay encompasses three different mechanisms which are summarised below:

$$\begin{aligned} \beta^- &: {}^A_Z X_N \rightarrow {}^A_{Z+1} X'_{N-1} + e^- + \bar{\nu}_e \\ \beta^+ &: {}^A_Z X_N \rightarrow {}^A_{Z-1} X'_{N+1} + e^+ + \nu_e \\ \epsilon &: {}^A_Z X_N \rightarrow {}^A_{Z-1} X'_{N+1} + e^+ + \nu_e \end{aligned} \tag{2.18}$$

The β^- (β^+) process involves the conversion of a neutron (proton) into a proton (neutron) with the emission of an electron, e^- (positron, e^+). The total energy of the decay is shared amongst the daughter nucleus (X'), the β particle (e^- or e^+) and the electron neutrino ($\bar{\nu}_e$ or ν_e). The three body nature of these two types of decays means that unlike α or γ decay, the β particles are emitted with a continuous distribution of energy.

The electron capture process involves the nucleus uptaking an atomic electron, typically from one of the inner atomic orbitals, leaving a vacancy in this orbital. An electron in a higher atomic orbital then deexcites itself into this corresponding vacancy. This deexcitation results in the emission of an x-ray with energy equal to the energy difference between the initial and final states of the deexcited electron. This x-ray has a label corresponding to the orbital of the captured electron (K, L, M ... etc).

Just like α and γ decay, β decay also obeys angular momentum and parity selection rules:

$$\Delta I = L + S \tag{2.19}$$

where ΔI is the change in nuclear spin, L is the angular momentum carried away by the decay and S is the total coupled spin from the β particle and neutrino. Since the electron and neutrino have intrinsic spin s=1/2, they can couple anti-parallel, giving $S = 0$ (Fermi decay) or parallel, giving $S = 1$ (Gamow-Teller) decay. β-decay is further grouped into two categories: 'allowed' and 'forbidden'. Allowed decays have no change in parity (also no change in parity for second-forbidden decays), therefore $L = 0$ and so $\Delta I = 0, 1$. Forbidden transitions have significantly lower transition probabilities in comparison to allowed decays. There are multiple orders of forbidden transitions, with first order having $L = 1$, second order $L = 2$, and so on. For a particular set of β decays, there is strong overlap between the quantum mechanical wavefunction of the initial and final nuclear states, resulting in significantly shorter half lives. Such decays are known as 'superallowed' β decays.

2.6 Gamma decay

Gamma decay is the emission of a photon as the nucleus de-excites from an initial excited state to a final state. When excited states of a nucleus are populated, gamma rays almost always follow. γ-rays typically range from a few keV up to 10 MeV, characteristic of the energy difference between the nuclear states. The energy of the emitted photon (E_γ) is written as:

$$E_\gamma = E_i - E_f - T_R \tag{2.20}$$

where E_i and E_f are the energies of the initial and final nuclear states respectively and T_R is the recoiling nucleus's kinetic energy. The nucleus recoils with an equal and opposite momen-

tum that of the γ ray (P_γ). Taking this into account and using the relativistic relationship $E_\gamma = cP_\gamma$, T_R can be expressed as:

$$T_R = \frac{E_\gamma^2}{2M_R c^2} \tag{2.21}$$

where M_R is the mass of the recoiling nucleus and c is the speed of light. This recoil energy is typically negligible, amounting to a 10^{-5} correction which is typically much smaller than the experimental uncertainty.

A γ decay can arise from either a electric (E) or magnetic multipole (M). Just like α and β decay, γ emission also has spin and parity selection rules which are given as:

$$\begin{gathered} |I_i - I_f| \leq L \leq I_i + I_f \\ \pi(EL) = (-1)^L, \\ \text{or,} \\ \pi(ML) = (-1)^{L+1} \end{gathered} \tag{2.22}$$

Where L is the angular momentum of the γ ray. The half life for an emission of a γ ray from a nuclear state can be approximated using the Weisskopf estimates, shown in Table 2.1:

Table 2.1: Single particle Weisskopf estimates of half lives for γ transitions (corrected for internal conversion). Values taken from [13].

Electric $t_{1/2}$(s)	Magnetic $t_{1/2}$(s)
E1 $\dfrac{6.76 \times 10^{-6}}{E_\gamma^3 A^{2/3}}$	M1 $\dfrac{2.20 \times 10^{-5}}{E_\gamma^3}$
E2 $\dfrac{9.52 \times 10^{6}}{E_\gamma^5 A^{4/3}}$	M2 $\dfrac{3.10 \times 10^{7}}{E_\gamma^5 A^{2/3}}$
E3 $\dfrac{2.04 \times 10^{19}}{E_\gamma^7 A^{2}}$	M3 $\dfrac{6.66 \times 10^{19}}{E_\gamma^7 A^{4/3}}$
E4 $\dfrac{6.50 \times 10^{31}}{E_\gamma^9 A^{8/3}}$	M4 $\dfrac{2.12 \times 10^{32}}{E_\gamma^9 A^{2}}$

Internal conversion

Internal conversion is an electromagnetic process which competes with γ decay. In this case, a photon is not emitted, instead, the electromagnetic multipole fields of the nucleus interact

with the atomic electrons resulting in the emission of an electron from the atom. Unlike β decay, this electron exists in an atomic orbital before this mechanism occurs, as opposed to being created in the decay process. The electrons emitted in internal conversion have quantised kinetic energies (T_e) which can be deduced from the equation:

$$T_e(K, L, M...) = E_\gamma - E_B(K, L, M...) \tag{2.23}$$

where E_B is the binding energy of the electron which is dependent upon the atomic shell which it originates from. Thus, internal conversion is only possible if $E_\gamma > E_B$ and E_B is different for each electron shell (K,L,M,...). This means that if K-shell emission is not possible, internal conversion may still be possible via L- or M-shell emission. Similar to the electron capture process, the conversion electron leaves a vacancy in the lower atomic orbital which is subsequently filled by the deexcitation of an electron from a higher orbital and hence, the emission of a characteristic x-ray. By measuring the number of conversion of electrons, or x-rays, one can determine the total internal conversion coefficient, α, from the equation:

$$\alpha_{tot} = \frac{\lambda_e}{\lambda_\gamma} \tag{2.24}$$

where λ_e and λ_e are the decay probabilities of the internal conversion process and the γ transition, respectively. This gives the probability of internal conversion relative to γ decay. The total decay probability, λ_t, can then be written as:

$$\lambda_t = \lambda_\gamma(1 + \alpha_{tot}) \tag{2.25}$$

One can then define partial internal conversion coefficients representing the individual atomic shells:

$$\alpha_{tot} = \alpha_K + \alpha_L + \alpha_M + ... \tag{2.26}$$

To this end, the signature decay of a nucleus provides a means of particle identification. As discussed in Chapter 3, energy gates can be applied to the α or γ decay peaks, allowing for high selectivity and enabling the production of the hyperfine structure spectra necessary to extract the nuclear properties produced in this work.

Chapter 3

Laser spectroscopy

Laser spectroscopy is an excellent tool for studying nuclear shape, size and electromagnetic moments of ground and long-lived isomeric states. In particular, by measuring the isotope shifts, one can determine the change in nuclear mean-squared charge radius between isotopes. From measurements of the hyperfine structure, one can extract the nuclear spin, magnetic dipole moment and spectroscopic electric quadrupole moment [15, 6, 16].

3.1 Isotope and isomer shifts

The shift of frequency of an atomic transition between two isotopes A and A' is referred to as the Isotope Shift (IS):

$$\delta\nu_{is}^{AA'} = \nu^{A} - \nu^{A'} \tag{3.1}$$

where ν is taken to be the centre of gravity (cg) of all hyperfine structure (hfs) components of the optical line. In order to demonstrate how one can measure this shift, Fig. 3.1 shows the shift between even-even Hg isotopes. In even-even nuclei, the spin of the ground state is zero, therefore there is no coupling with the electron spin resulting in no hyperfine splitting.

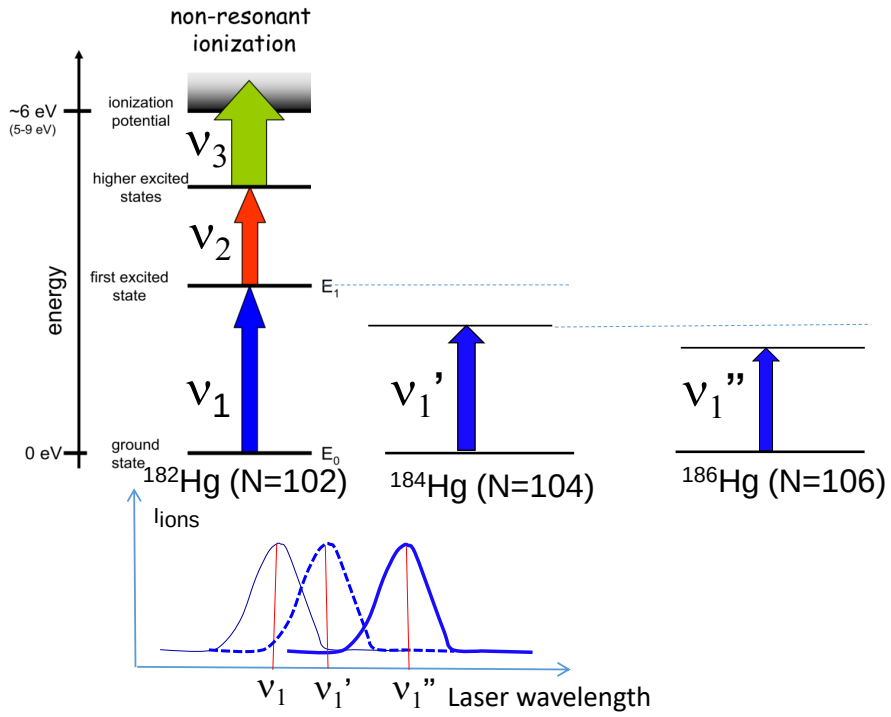

Figure 3.1: An example of IS for even-even Hg isotopes. A three-step laser scheme is used with the first transition scanned in Narrow-Band (NB) mode to determine how the ionisation efficiency varies with laser wavelength. From this one can determine the IS.

From scanning the first transition in the three-step laser scheme, one can measure the shift in atomic transition frequency in these Hg isotopes with respect to the reference isotope. The isotope shift can be written as the sum of two components [17]:

$$\delta\nu_{is}^{AA'} = \delta\nu_{ms}^{AA'} + \delta\nu_{fs}^{AA'} \tag{3.2}$$

where $\delta\nu_{ms}^{AA'}$ is the mass shift and $\delta\nu_{fs}^{AA'}$ is the field shift.

The mass shift occurs due to a change in the total mass of the system when the number of neutrons changes and can be expressed as:

$$\delta\nu_{ms}^{AA'} = \frac{A' - A}{AA'} M \tag{3.3}$$

where A' and A are the atomic masses of the isotopes and $M = M^{NMS} + M^{SMS}$, where M^{NMS} and M^{SMS} are the normal mass shift (NMS) and specific mass shift (SMS) constants. The SMS occurs due to electron-electron correlations in a multi-electron system and is calculated

either theoretically or calibrated using experimental data. The NMS, which is equivalent to the Bohr reduced mass correction [6], can be determined by the equation:

$$M^{NMS} = \frac{\nu m_e}{m_p} \tag{3.4}$$

where ν is the transition frequency, m_e and m_p are the mass of the electron and proton respectively.

The field shift, $\delta\nu_{fs}^{AA'}$, is a result of the influence of the finite extension of the nuclear charge distribution on the electronic binding energy [16]. It was shown, that the field shift is sensitive to the changes in mean-squared charge radii between different nuclides. The field shift is given by:

$$\delta\nu_{fs}^{AA'} = F\delta\langle r^2\rangle^{A,A'} \tag{3.5}$$

where F is an electronic factor and $\delta\langle r^2\rangle^{A,A'}$ is the change in the mean-squared charge radius between isotopes A and A'. Thus, combining the mass shift and field shift equations produces a final expression for the total isotope shift:

$$\delta\nu_{is}^{AA'} = \frac{A'-A}{AA'}M + F\delta\langle r^2\rangle^{A,A'} \tag{3.6}$$

From this expression, once the M and F factors have been determined, measurements of the isotope shift yield the change in the mean-squared charge radius between different isotopes. Furthermore, for long-lived isomers in a given nucleus, the isomer shift can also be determined (in this case, the mass shift is equal to zero). From this one can measure differences in the mean-squared charge radius between different states of the same nucleus. Thus, laser spectroscopy is a valuable tool in probing shape coexistence across the nuclear chart.

3.2 The hyperfine structure

The hyperfine structure (HFS) is a result of the coupling of the electronic spin J with nuclear spin I, resulting in the splitting of the electronic energy levels into hyperfine sub levels, which are identified by an operator, F:

$$\mathbf{F} = \mathbf{I} + \mathbf{J} \tag{3.7}$$

Figure 3.2 shows the scanning of the HFS of ^{179}Hg.

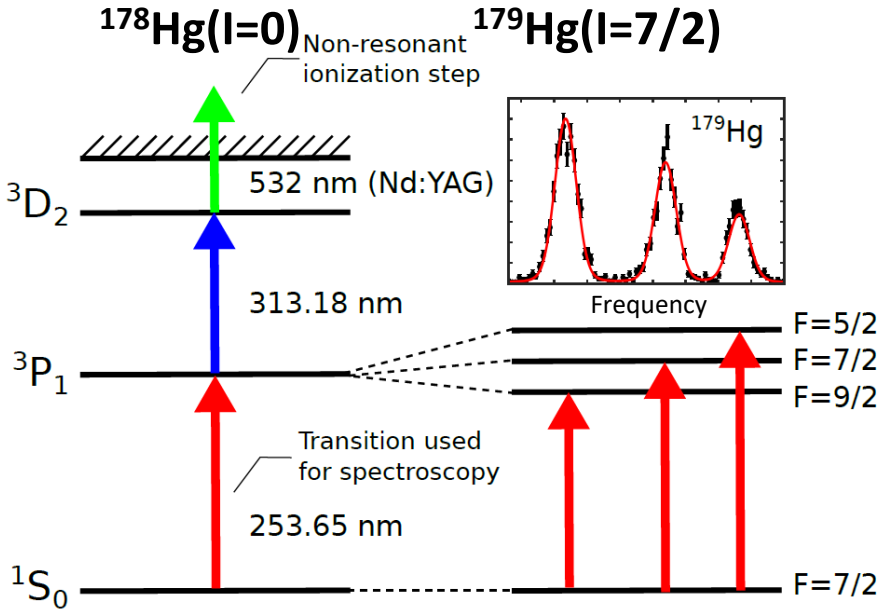

Figure 3.2: A comparison between the HFS of an even-even (^{178}Hg) and an odd-mass (^{179}Hg) Hg isotope. For the odd-mass case (on the right hand side), the spin of the nucleus is non-zero, resulting in coupling of the angular momenta of the atomic electrons and the nucleus, splitting the atomic energy levels into the hyperfine structure. The HFS spectra can be seen for ^{179}Hg, produced from scanning the 253.65nm transition.

Transitions between hyperfine levels are permitted if $\Delta F = 0, \pm 1$ with the exception of transitions between states with $F = 0$. The energy shift in each level is given by [18]:

$$\triangle E/h = \frac{K}{2}a + \frac{3K(K+1) - 4I(I+1)J(J+1)}{8I(2I-1)J(2J-1)}b \tag{3.8}$$

where $K = F(F+1) - I(I+1) - J(J+1)$ and a and b are the hyperfine constants relating to the nuclear magnetic dipole and electric quadrupole moments respectively. The parameter a is given by:

$$a = \frac{\mu B_e}{IJ} \tag{3.9}$$

This term accounts for the interaction between the magnetic dipole moment, μ, of the nucleus and the magnetic field, $B_e(0)$, produced at the site of the nucleus by the electrons. The parameter b is given by:

$$b = eQ_s\left\langle \frac{d^2V_e}{dz^2} \right\rangle \tag{3.10}$$

This term arises due to the interaction between the electric quadrupole moment of the nucleus, Q_s, and the electric field gradient, $\left\langle \frac{\delta^2 V_e}{\delta z^2} \right\rangle$, produced by the atomic electrons.

Magnetic dipole moment

The nuclear magnetic dipole moment arises primarily due to the orbital and spin angular momenta of its constituent nucleons, with modifications arising due to effects such as core polarization, which is when the unpaired nucleon polarizes the core resulting in deformation, as well as the rotational motion of the nucleus. In the ground state of an even-even nucleus, the pairing force favours the coupling of nucleons such that their orbital and spin angular momentum couple to zero and as a result, paired nucleons do not contribute to the magnetic moment and so the net magnetic dipole moment is zero. For an odd-mass nucleus, the total magnetic dipole moment results predominantly from both the intrinsic spin of the valence nucleon as well as its orbital angular momentum. Therefore, measurements of the magnetic dipole moment can provide information on the single particle nature of the nucleus. For odd-odd nuclei, both the unpaired proton and neutron contribute to the magnetic dipole moment and so the total magnetic dipole moment of the nucleus can be deduced using the additivity rule [19] (shown in Section. 8.4).

Electric Quadrupole moment

The electric quadrupole moment is dependent upon the distribution of charge within the nucleus. For well deformed nuclei, one can use the measurement of the spectroscopic electric quadrupole moment (Q_s) to determine the static deformation parameter, $\langle\beta_2\rangle$, via the strong coupling projection formula:

$$Q_s \cong \frac{I(2I-1)}{(I+1)(2I+3)} \frac{5Z\langle r^2_{sph}\rangle}{\sqrt{5\pi}} \langle\beta_2\rangle(1+0.36\langle\beta_2\rangle) \tag{3.11}$$

where $\langle r^2_{sph}\rangle$ is the mean square charge radius of the nucleus if it were spherical. $\langle r^2_{sph}\rangle$ can be determined using the Droplet Model [8, 20]. Specific application of these methods will be described in Sections. 8.1, 8.4 and 8.8.

Chapter 4

Previous work in the lead region

The neutron-deficient lead region is considered as having the largest manifestation of shape coexistence across the nuclear chart [4, 5, 6]. Within the microscopic shell model discussed in Section 2.2, shape coexistence may arise from energetically favourable particle-hole excitations across the shell gap. These excitations result in low lying intruder states of deformed nuclear shape. This phenomenon of low energy shape coexistence, as well as the manifestation of intruder states, will be discussed in Section 4.1.

4.1 Intruder states and low energy shape coexistence

Low energy shape coexistence is a phenomenon in which different configurations of protons and neutrons form low energy eigenstates within the same nucleus, with differing nuclear shapes. This effect was first discovered by Morinaga in 1956 [3] in ^{16}O. In this nucleus, the 0^+ ground state has a doubly-closed shell with a spherical shape. On top of the ground state is the first excited 0^+ state at 6.06 MeV, which has a different band structure, with a 2^+ rotational state at 6.91 MeV. Since then, extensive studies have been carried out across the Segre chart and a recent review by Heyde and Wood [4] comes to the conclusion that shape coexistence occurs throughout the nuclear chart, as opposed to being a localised phenomenon. The energy of intruder states in even-even nuclei, is given by the equation:

$$E_{intr} = 2(\epsilon_{j\pi} - \epsilon_{j'\pi}) - \Delta E_{pair} + \Delta E_M + \Delta E_Q \tag{4.1}$$

taken from [21]. The first term, $2(\epsilon_{j\pi} - \epsilon_{j'\pi})$, accounts for the energy required to excite a pair of protons across the shell gap. The second term, ΔE_{pair}, is due to the pairing correlation.

This is the energy gain arising from the coupling of particle (or hole) pairs to give spin zero. The third term (ΔE_M), is the monopole shift, which is the shift in the proton single-particle energy, which is dependent on neutron number and can be either attractive or repulsive. The final term, ΔE_Q, is the energy gain due to the quadrupole interaction. The quadrupole component breaks $I^\pi = 0^+$ proton-proton or neutron-neutron pairs into $I^\pi = 2^+$ pairs, an effect known as core polarization, driving quadrupole deformation. This effect is largest when the number of valence nucleons is maximal. Fig. 4.1 shows a schematic plot of these effects against neutron number, N, between the two closed neutron shells: N=82 and N=126.

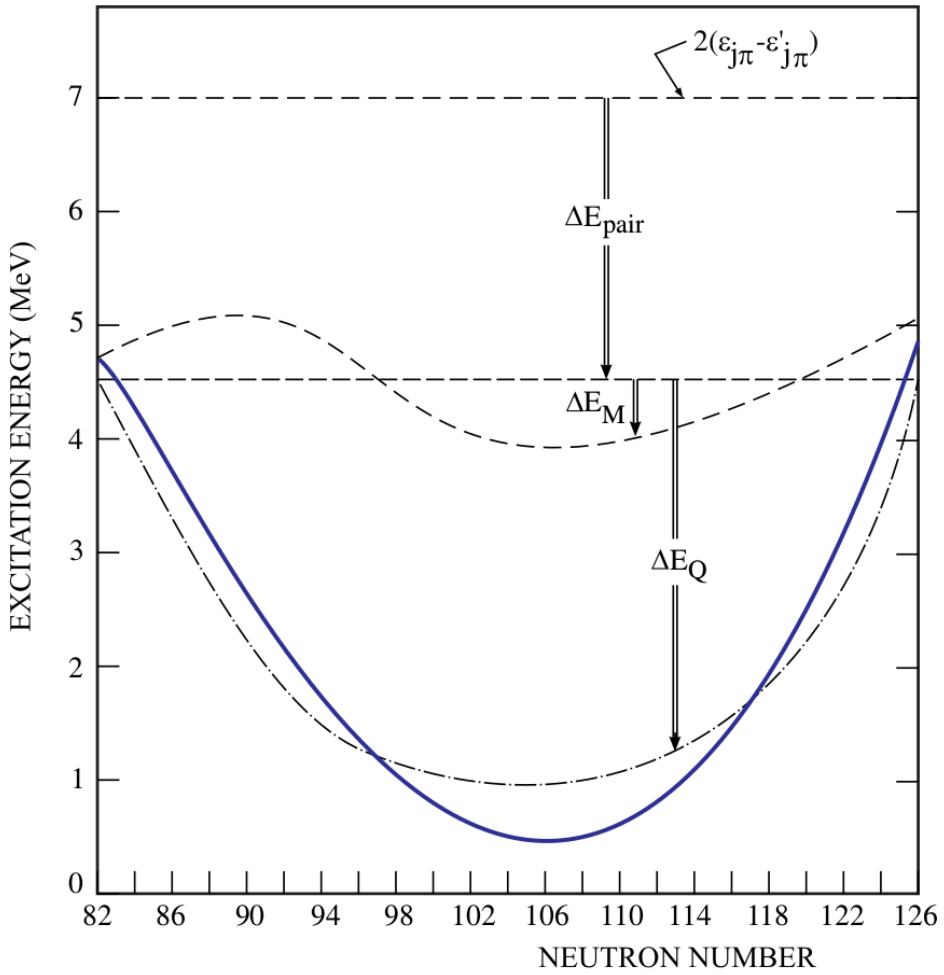

Figure 4.1: A schematic plot of 2^+ excitation energy against neutron number showing the unperturbed energy $2(\epsilon_{j\pi} - \epsilon_{j'\pi})$, the pairing energy ΔE_{pair}, the monopole shift ΔE_M and the quadrupole energy gain ΔE_Q,. The blue line represents the summation of all these different effects. Figure taken from [4].

In Section 2.3, the Nilsson model was discussed. In this model, energies of the Nilsson

orbitals have a strong dependence on the deformation. For example, if one considers the 9/2[505] proton Nilsson orbital shown in Fig. 2.5, the energy rapidly increases with decreasing deformation parameter, oblate side ϵ_2 (negative). In addition the 1/2[400] orbital increases in energy below $\epsilon_2 = 0$. These two effects reduce the energy necessary to allow a particle-hole excitation between the corresponding nuclear shell model states: $\pi 1h_{9/2}$ and $\pi 3s_{1/2}$. Hence, the equivalence of the spherical shell model and deformed nilsson model, can explain the emergence of shape coexistence for nuclei near Z=82 [22]. Perhaps the most famous example in this region is the case of ^{186}Pb, where three different 0^+ states with spherical, oblate and prolate shapes were found to lie within 1 MeV of each other as shown in Fig. 4.2 [23].

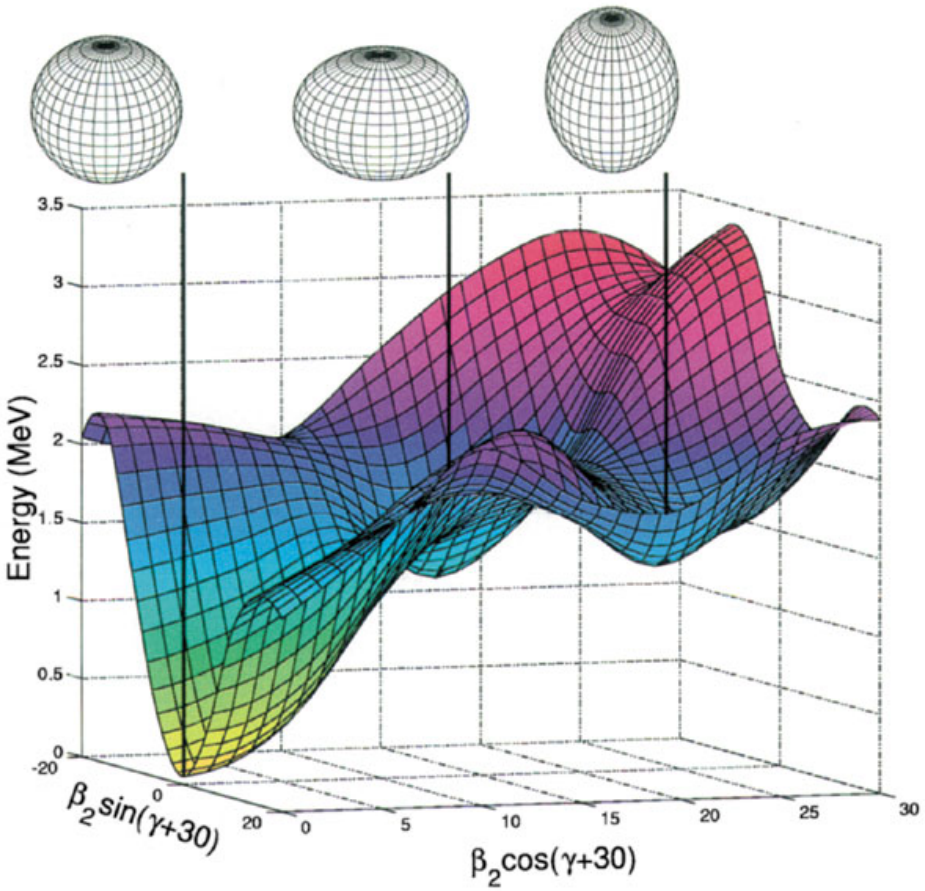

Figure 4.2: Calculated potential energy surface for ^{186}Pb. The β_2 parameter expresses the elongation of the nucleus along the symmetry axis, whilst the γ parameter expresses the degree of triaxiality in the deformation, such that $\gamma = 0°$ corresponds to a prolate shape, and $\gamma = 60°$ represents that of an oblate nucleus. Figure taken from [23].

The uniqueness of the lead region can be attributed to three different effects. Firstly, the proton energy gap of 3.9 MeV above the Z=82 shell closure favors a spherical shape in

their ground state. However, this energy is small enough to allow particle-hole excitations across the gap, producing valence proton particles and holes. Furthermore, a large valence neutron space is present between magic number N=82 and N=126. The residual interaction between valence protons and neutrons results in unusually low lying states of different shapes competing with the ground state in the vicinity of this neutron midshell [23].

4.2 Laser spectroscopy studies in the lead region

Laser spectroscopy is one of the techniques which enables us to investigate cases of shape coexistence in this region, via extraction of nuclear properties of the ground and isomeric states of nuclei along an isotopic chain in a model independent way. The first example of shape evolution within the lead region was discovered in 1972 by Bonn *et al.* [24], when a drastic shape change was observed between the nuclei ^{187}Hg and ^{185}Hg using β-radiation detection of optical pumping (β-RADOP). This is considered one of the most iconic discoveries in nuclear structure physics over the past 60 years [5]. Shortly afterwards, γ-ray spectroscopy revealed that this shape transition was not present in the even-mass neighbours ^{184,186}Hg [25, 26]. Thus the picture became clear, these Hg isotopes were undergoing a shape staggering between large and small deformations when moving between odd- and even-mass nuclei. Thereafter in 1976, Bonn *et al.* was able to establish that the isotopes ^{181,183}Hg were also heavily deformed [27]. The development of laser spectroscopy paved the way for measuring isotope shifts, hyperfine parameters and electromagnetic moments, but due to the inability to investigate below A=181, the picture for the neutron deficient Hg isotopes remained the same for over 30 years.

Over the past two decades, extensive laser spectroscopy studies have been carried out in the lead region by the Windmill-RILIS-ISOLTRAP collaboration. Fig. 4.3 shows the charge radii systematics of the ground states of isotopes in the vicinity of the Z=82 shell closure as of 2019. The method of decay tagged in-source laser spectroscopy, used in these studies, combines the high sensitivity of decay spectroscopy with the large efficiency of in-source laser ionisation, enabling the measurement of very short-lived nuclei far from stability. To this day, the highest sensitivity achieved using this method was the measurement of ^{191}Po, with an implantation rate of 0.01 ions/second [28].

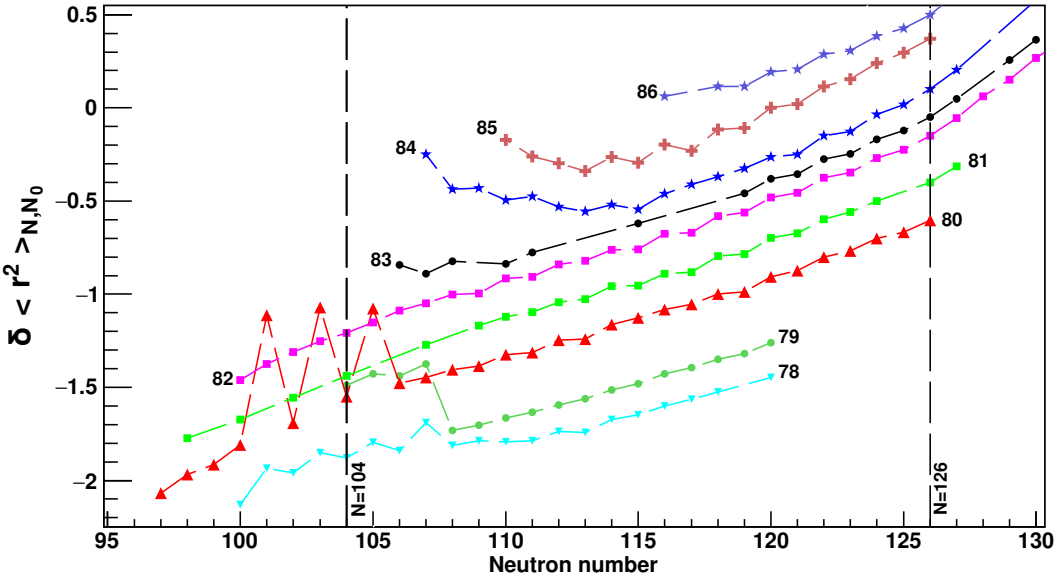

Figure 4.3: Ground state changes in mean-squared charge radii in the Pb region as of 2019. The numbers in black represent the proton number for each isotopic chain. Data taken from [29, 30, 31, 32, 33, 34, 35]

Between 2003 and 2014, the collaboration investigated the Tl, Pb, Po and At isotopic chains. The Pb isotopes, with a full Z=82 shell closure, were determined to be spherical in their ground state, including when crossing the N=104 neutron midshell [36]. On the other hand, the Po isotopes, situated two protons above the Z=82 shell closure, were observed to undergo a rapid onset of deformation upon approaching the neutron midshell [28, 37, 38]. The ground states of Tl isotopes, positioned one proton below the Z=82 shell closure, follow the same spherical trend of the Pb isotopic chain, with slight deformation observed in the $I^{\pi} = 9/2^{-}$ isomers [34]. Lastly, the At isotopes revealed a strong deviation from the charge radii systematics of the spherical Pb isotopes, interpreted as an onset of deformation, resembling the behaviour of the Po isotopes [35]. [1]

Since then, the collaboration has carried out in-source laser spectroscopy measurements of Au, Hg and Bi isotopic chain. The Hg isotopes were measured in 2015, revealing two crucial outcomes. Fig. 4.4 shows the measurements of the changes in mean-square

[1] In 2013-2017, the Fr isotopic chain was also investigated using Collinear Resonance Ionisation Spectroscopy (CRIS), a technique allowing one to extract the quadrupole moment of these isotopes with much greater accuracy [39, 40, 41, 42].

charge radii for these Hg isotopes, with the solid straight line showing the trend seen for spherical Pb nuclei [43].

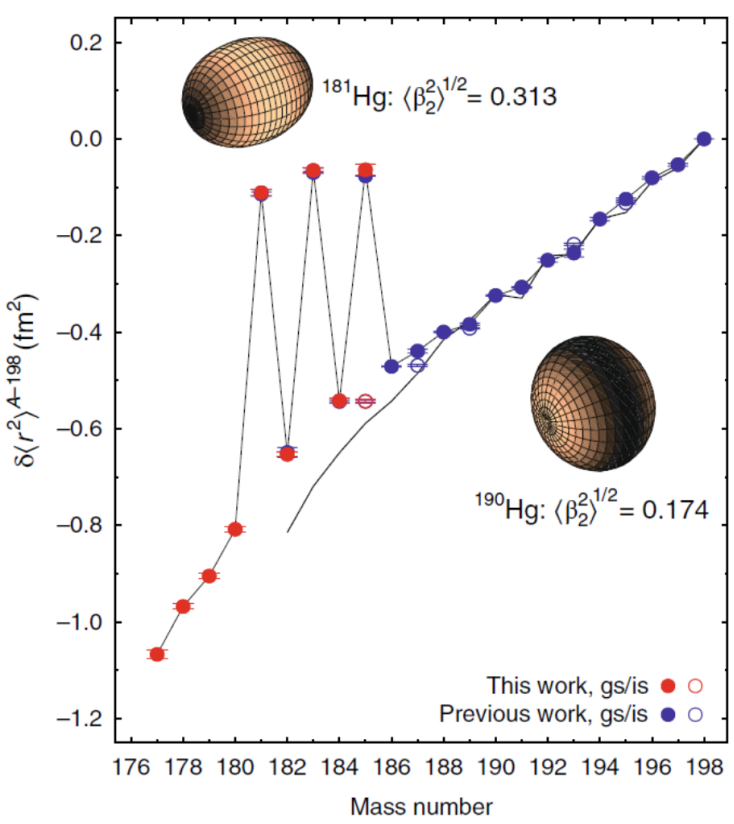

Figure 4.4: Changes in mean-square charge radii as a function of mass number for isotopes $^{177-198}$Hg. Figure taken from [43]. The results from B. Marsh *et al.* in 2019 [43] are shown in red with the previous results from Bonn *et al.* in 1972 [24] and G. Ulm *et al.* [44] shown in blue. The ground (gs) and isomeric (is) states are represented by filled and open circles respectively. The shapes of ^{190}Hg and ^{181}Hg are shown for comparison. The black line represents the trend in the previously measured spherical lead nuclei.

Firstly, the shape staggering effect seen in $^{181-185}$Hg by Bonn *et al.* was reproduced. Secondly, measurements were extended to below A=181. This revealed that this staggering phenomenon ceases at ^{181}Hg, with the lighter isotopes starting to approach near-spherical trend observed in the heavier isotopes (A >186). These data also agree well with in-beam spectroscopy measurements of even-even Hg isotopes [45, 46, 47], with systematics of excited states shown in Fig. 4.5. The excitation energies of even-even $^{190-198}$Hg isotopes show a constant behaviour associated with the weakly deformed oblate ground state. However, this trend is somewhat distorted in the lighter mercury isotopes around neutron mid-shell at

N=104 due to the intrusion of a strongly deformed prolate band. This band is built on top of a deformed excited 0_2^+ state which arises from proton excitations across the Z=82 shell gap. Both the laser and in-beam spectroscopy studies provide strong evidence for shape coexistence in the isotopes $^{181-185}$Hg. That is, within these nuclei, there are two states with different nuclear shapes, coexisting at low energy. Furthermore, based on in-beam studies one can see that the pattern of excited states in the lighter Hg isotopes e.g. ^{174}Hg indicates that its ground state becomes spherical again. This is expected when moving towards the next neutron shell closure at N=82.

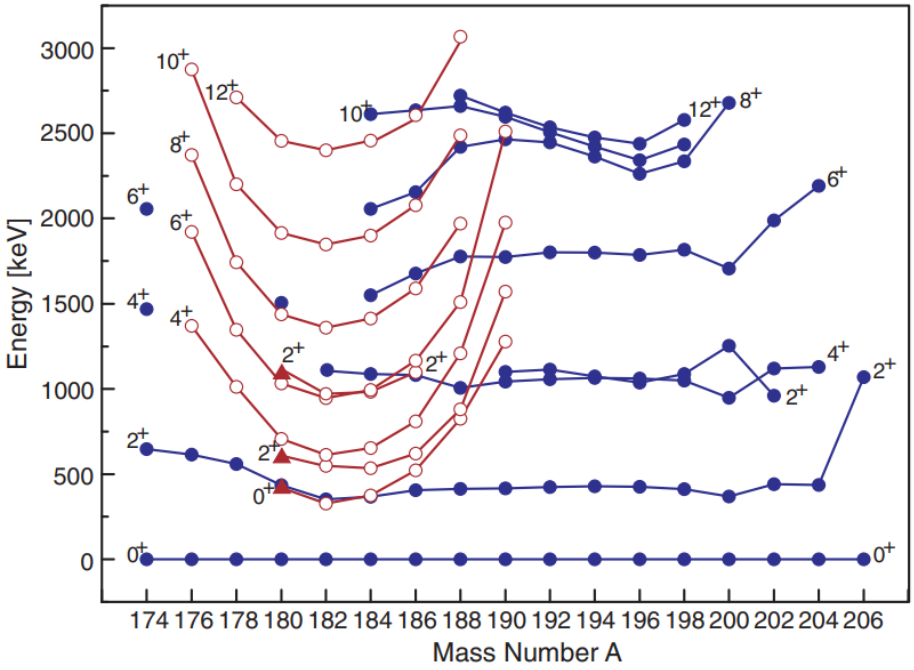

Figure 4.5: Excitation energy systematics for even-even neutron deficient Hg isotopes. Full and hollow symbols are the level energies of the ground and excited state bands respectively. Figure taken from [48].

Theoretical nuclear calculations allow one to probe the structure of these intruder states in nuclei. Recently, Monte Carlo Shell Model (MCSM) calculations were performed on the neutron deficient Hg isotopes [43], in order to further understanding of this shape staggering phenomenon seen in these nuclei. Fig. 4.6 shows a comparison of the experimental charge radii systematics, with that of the results of these MCSM calculations.

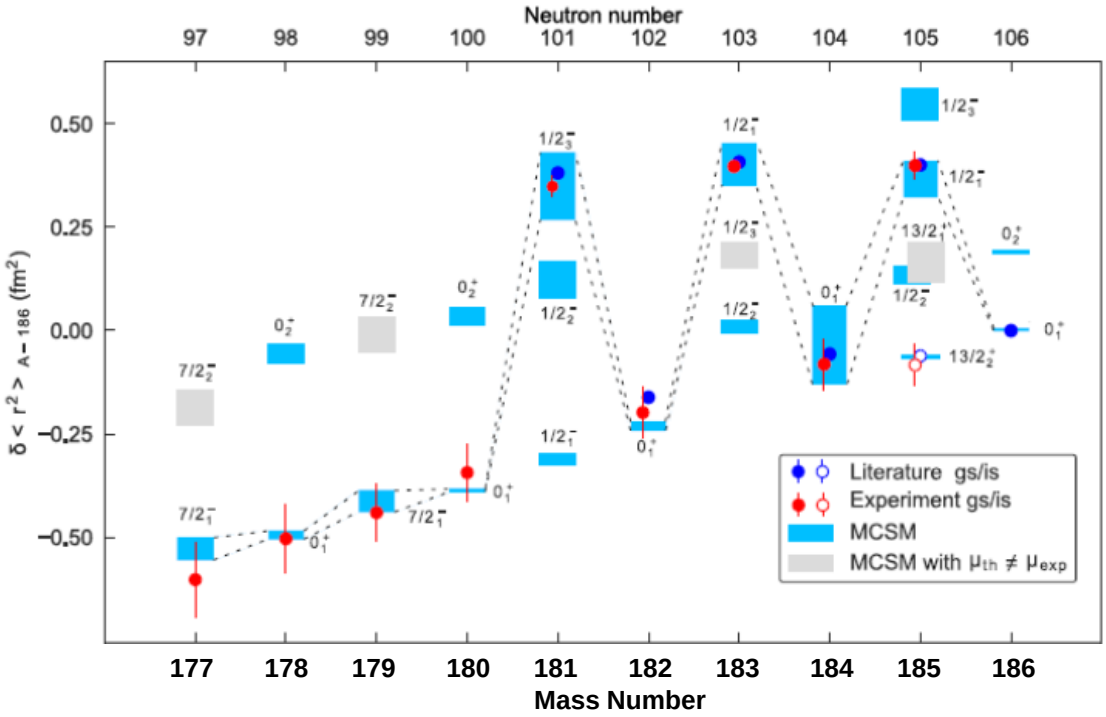

Figure 4.6: Change in mean-square charge radius with respect to the ground state of ^{186}Hg. Red points are experimental data taken at ISOLDE. The blue (grey) shaded areas indicate the extracted radii values corresponding to MCSM eigenstates labelled by their spin, parity and energy level ordering with calculated magnetic moment in agreement (disagreement) with the experimental value. Figure taken from [43].

Remarkable agreement with the experimental values was achieved. This enabled examination of the eigenstates in order to determine the underlying mechanism behind this shape staggering phenomena. the most compelling discrepancy between the heavily deformed $1/2^-$ states in ^{181,183,185}Hg and the near spherical even mass neighbouring isotopes is the occupancy of two orbitals: the $1h_{9/2}$ proton orbital above the Z=82 shell closure and the $1i_{13/2}$ neutron midshell between N=82 and N=126. The deformed states exhibit large and constant values of neutrons in the $1i_{13/2}$ orbit as well as a considerable promotion of 2-3 protons across the Z=82 shell gap into the $1h_{9/2}$ orbit(see Figures 2c and 17 in Refs. [43] and [49], respectively). This sudden reconfiguration of nucleons is a result of both the quadrupole and monopole components of the nucleon-nucleon interaction. As discussed in section 2.3, the monopole component and the quadrupole interaction lowers the binding energy. In this case, the energy decrease is greater than the energy required to create the particle-hole excitations, thus, the deformed state becomes the ground state. Such calculations are of great importance

understanding any effects observed in the Pb region.

Chapter 5

Previous work on Bi isotopes

As discussed in section 4.1, the manifestation of shape coexistence can be explained by the occurrence of low lying intruder states in the shell model. In the neutron deficient odd-mass Tl isotopes, the spherical $1/2^+$ ground state coexists with a low lying $9/2^-$ intruder state. In the case of the odd-mass Bi isotopes, these states are flipped: the $9/2^-$ near spherical ground state co-exists with a low lying $1/2^+$ intruder state. However, for both of these isotopic chains, the intruder state is produced via the same mechanism: excitation of a proton across the Z=82 shell gap, into the $1h_{9/2}$ orbital. Figure 5.1 shows the shell model diagram for both these states in the odd-mass Bi and Tl isotopes.

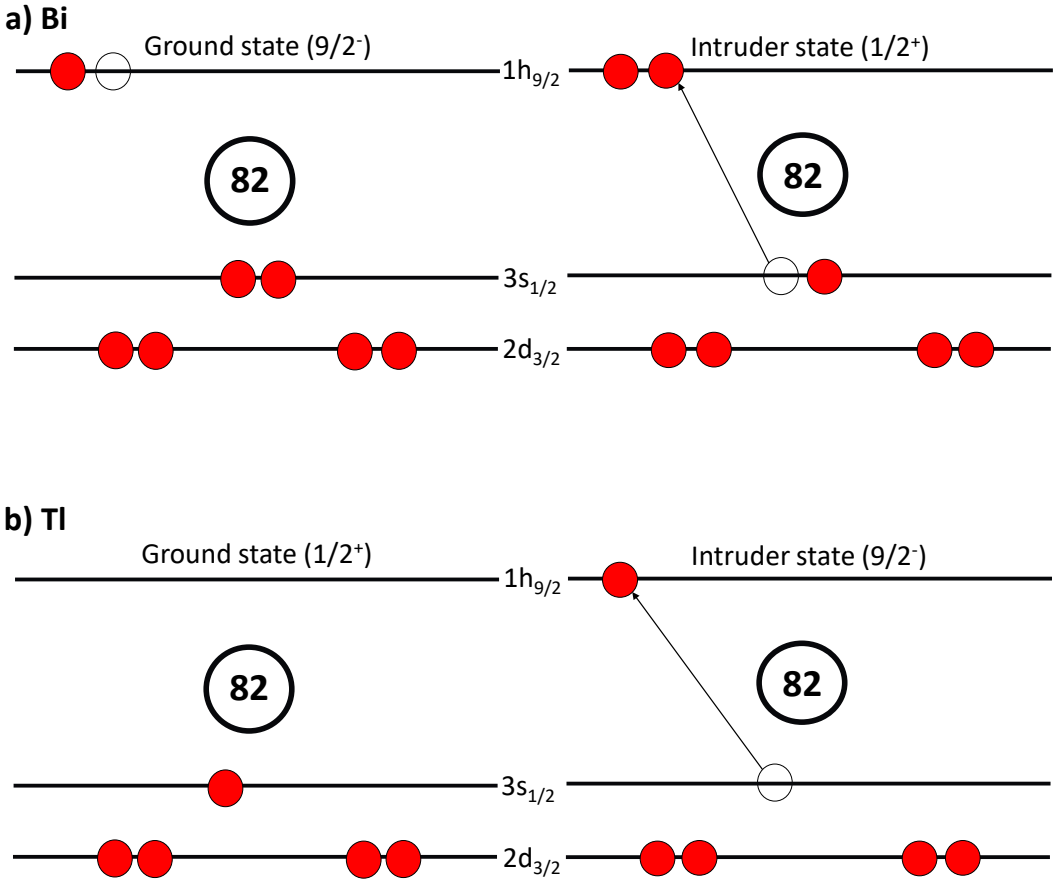

Figure 5.1: (a) Shell model diagram showing the orbitals occupied by the protons (red circles) and the holes (hollow circles) for both the ground state ($9/2^-$) and the intruder state ($1/2^+$) of odd-mass Bi isotopes. (b) Shell model diagram showing the orbitals occupied by the protons for both the ground state ($1/2^+$) and the intruder state ($9/2^-$) of odd-mass Tl isotopes. In both circumstances, the intruder state is produced via excitation of a proton across the Z=82 shell gap, shown by the arrows.

The ^{A}Bi$\rightarrow^{A-4}$Tl α decay has proven an extremely useful tool for the identification of the configurations of neutron deficient Bi nuclei. This is based on the fact that in odd-mass $^{187-195}$Bi isotopes, one typically observes unhindered ($\Delta L = 0$) $\pi s_{1/2}^{-1} \rightarrow \pi s_{1/2}^{-1}$ as well as $\pi h_{9/2} \rightarrow \pi h_{9/2}$ α decays. Figure 5.2 shows the α-decay systematics of the odd-mass Bi isotopes in the range $^{187-197}$Bi [50].

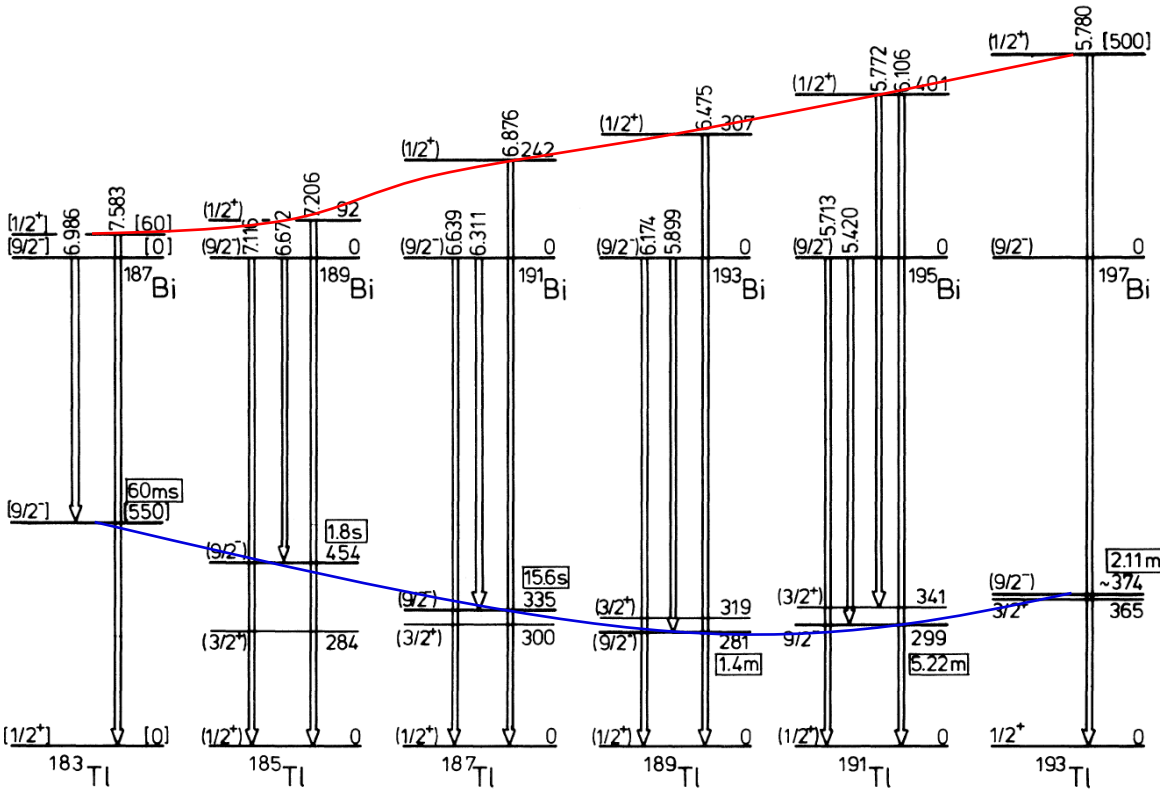

Figure 5.2: Low energy systematics of odd-mass Bi and Tl isotopes and α-decay scheme of Bi isotopes, showing the energies of each decay. The red and blue lines represent the energy systematics of intruder states of the Bi and Tl isotopes, respectively. Figure taken from [50].

Figure 5.3 shows a comparison of the experimental excitation energies of the Bi and Tl intruder states with respect to their corresponding ground states. For the Tl isotopes, the parabolic dependence of excitation energy with minima close to the N=104 mid-shell is a well established phenomenon [51].

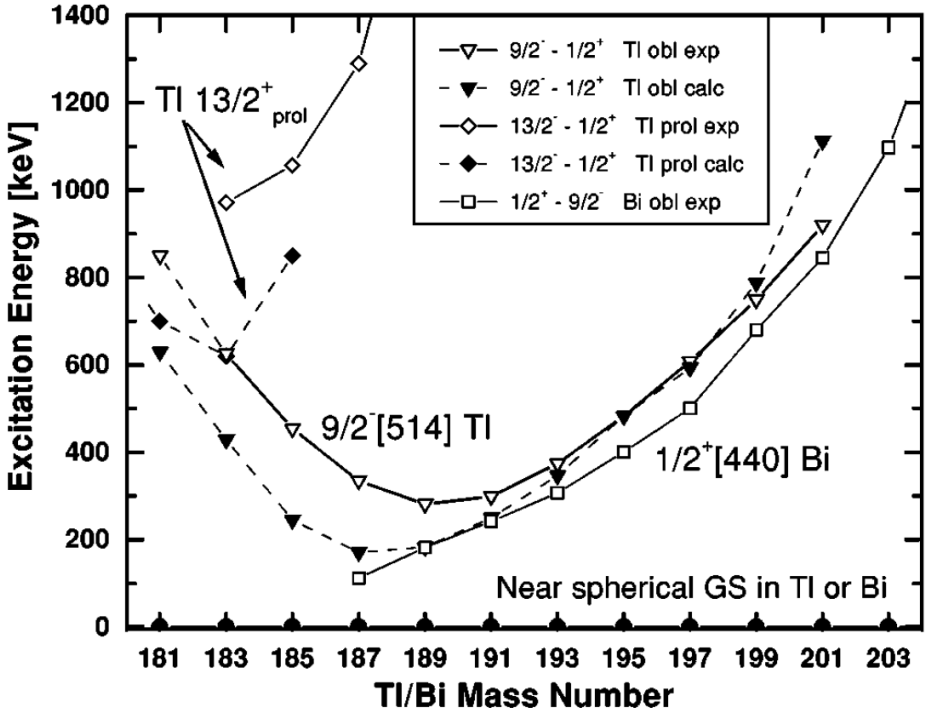

Figure 5.3: Experimental (open symbols with solid lines) and theoretical (filled symbols with dashed lines) excitation energies of the low lying intruder states for both Bi and Tl isotopes with respect to their ground states. Theoretical values were obtained from potential energy surface (PES) calculations from [52], with experimental data taken from [50, 53, 54, 55]

From Fig. 5.3, below ^{191}Bi, a strong deviation from the parabolic dependence of the Tl isotopes is clearly observed in the Bi isotopic chain when approaching the N=104 midshell. Extrapolation of this effect reveals that the $1/2^+$ intruder state in ^{185}Bi becomes the ground state, lying below the spherical $9/2^-$ state. This is surprising and provides an indication that the structure of this intruder state in ^{187,189}Bi will differ from that of the heavier isotopes. This point is further emphasised in the Potential Energy Surface (PES) calculations carried out in Ref. [52] on odd-mass neutron deficient Bi isotopes in order to determine their underlying structure. From these calculations a drastic change in nuclear shape is predicted. Fig. 5.4 shows the PES plots for these isotopes for both positive and negative parity states. These plots reveal a multitude of low lying minima of different nuclear shapes, each with their corresponding nuclear configuration. From these plots, two main conclusions can be drawn. Firstly, for the negative parity states, the ground state minima are calculated as near spherical with the β_2 gradually increasing from 0.074 at ^{195}Bi up to 0.09 at ^{187}Bi. In the spherical shell model approach, this state corresponds to the odd proton occupying the $1h_{9/2}$ spherical orbital

above the Z=82 proton shell closure (shown Fig. 5.1). The slight prolate shape arises from the polarisation effects of this valence proton. Experimentally, these states are known to exist in $^{187-209}$Bi [52], see Fig. 5.2. For the positive parity states, moderately deformed oblate minima were determined from these calculations, at $\gamma = -60°$ with the β_2 values gradually increasing from 0.125 at N=112 up to $\beta_2 = 0.14$ at the neutron midshell. In the language of the spherical shell model approach, these minima arise from the excitation of a proton from the closed shell into the $1h_{9/2}$ orbital, coupling with the odd proton in this state, leaving an unpaired proton in the $3s_{1/2}$ level. The result is a $\pi[2p - 1h]$ configuration.

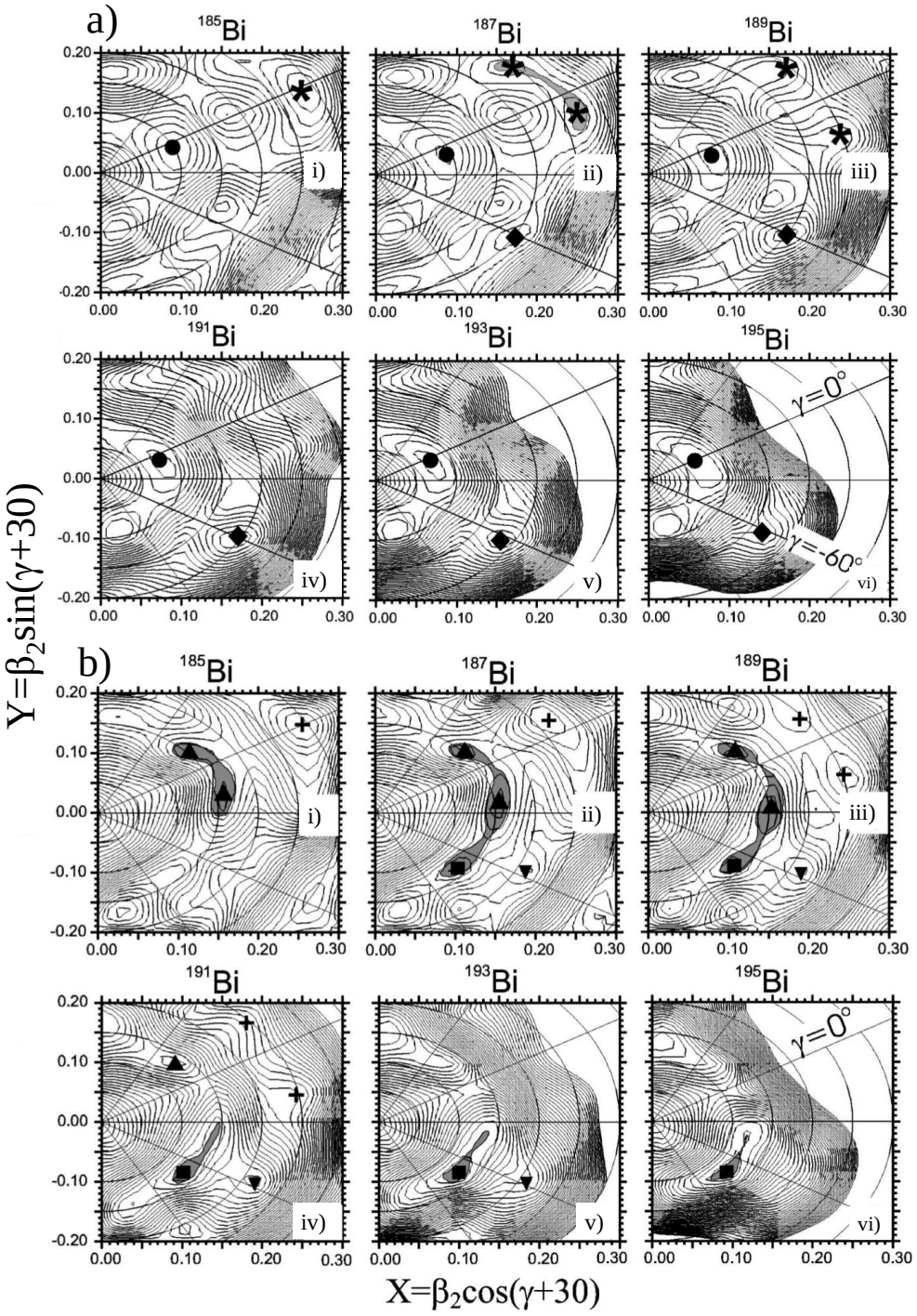

Figure 5.4: Potential-energy surfaces for the negative (a) and positive (b) parity states in the isotopes $^{185-195}$Bi. Near spherical, oblate and prolate states are indicated by filled circles, diamonds and stars, respectively. γ-soft minima are shown by shaded areas. Figure adapted from [52].

5.1 Bi laser spectroscopy studies

Fig. 5.5 shows the charge radii systematics for Bi isotopes before the work presented in this thesis. The first laser spectroscopy measurements were carried out in 1995-1996 by Campbell on the isotopes ^{202,203,204}Bi *et al.* [56, 57]. In these studies, gas cell laser spectroscopy was used at SUNY, Stony Brook to measure the isotope shifts of $^{202-204}$Bi. Five years later, further laser spectroscopy measurements were carried out at ISOLDE in 2000 by Pearson *et al.* [58]. In this investigation, gas cell laser spectroscopy was utilised again to measure the isotope shifts and electromagnetic moments of the isotopes $^{205-210,212,213}$Bi. From this study, the charge radii systematics appeared to follow the Pb trend, with the odd-even staggering being identical to what was observed in the Pb isotopic chain.

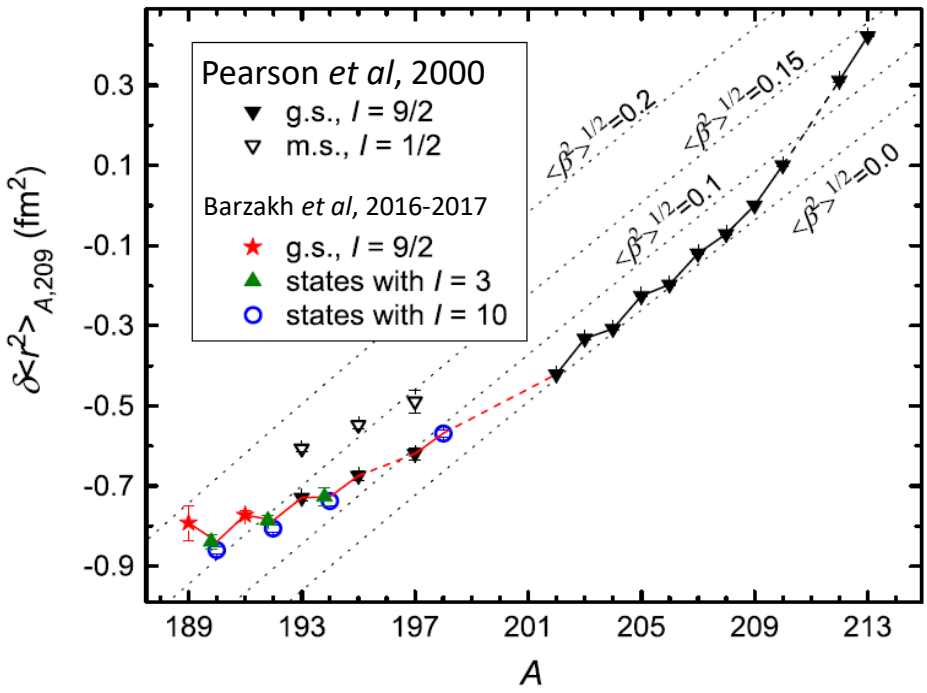

Figure 5.5: Changes in mean-square charge radii for Bi isotopes. Full downward triangles represent $9/2^-$ ground states [31, 58], hollow triangles: $1/2^+$ intruder states [31]. Stars show most recent measurements of ground state odd-A Bi nuclei [32]. Circle represent 10^- states [32] and upward triangles 3^+ states [32]. The dotted lines represent the droplet model prediction [8, 20] for different mean-square deformations. Figure taken from [32].

More recently in 2017, laser spectroscopy studies were carried out on Bi isotopes at the

Investigation of Radioactive Isotopes on Synchrocyclotron facility (IRIS) in Petersburg [32, 31]. Data on neutron deficient isotopes were collected, with the changes in mean-squared charge radius being obtained down to ^{189}Bi. These data revealed a marked deviation from the charge radii systematics of the Pb and Tl isotopic chains below ^{194}Bi. This was interpreted as an onset of quadrupole deformation. This onset of deformation in what was previously believed to be a spherical $9/2^-$ ground state in odd-mass Bi isotopes is a new phenomenon and will be investigated in more detail in this work. Furthermore, a large isomer shift was observed for the $1/2^+$ intruder states of ^{193,195,197}Bi, indicating the presence of shape coexistence in these isotopes. It is crucial that measurements are extended to ^{191m}Bi, as well as more accurate data are obtained for ^{189g,191g}Bi. This will allow further investigation of the departure of the intruder state excitation energy from the parabolic N dependence of the Tl isotopes.

Chapter 6

Experimental methods to study Bi isotopes

The results presented in this thesis are from experiments which took place at the Isotope Separator OnLine DEvice (ISOLDE) facility at CERN (Geneva, Switzerland). ISOLDE is located next to the Proton Synchrotron Booster (PSB), as shown in Fig. 6.1.

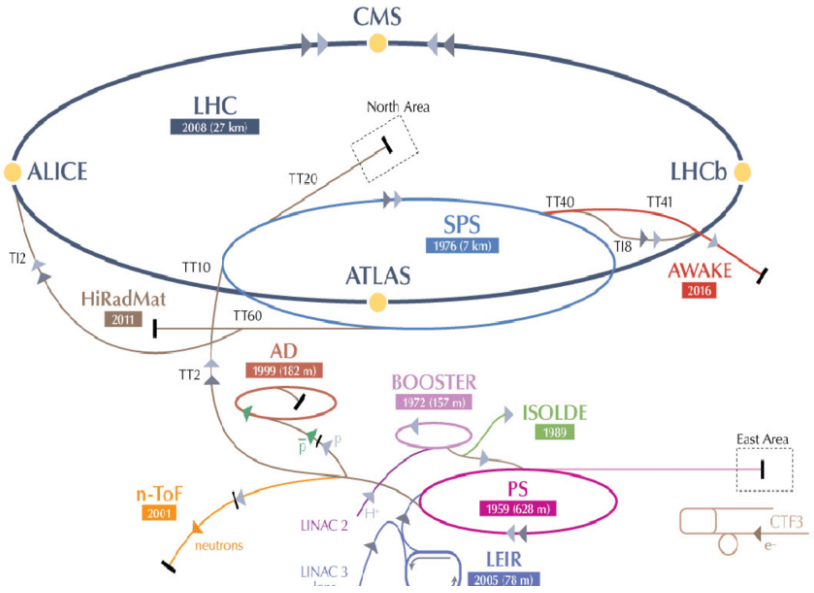

Figure 6.1: A schematic view of the CERN facility with ISOLDE shown in green, located next to the PSB, shown in pink. Figure taken from [59].

6.1 ISOLDE facility

ISOLDE is the CERN experimental hall for the production of radioactive ion beams using the Isotope Separator On-Line (ISOL) technique [60]. The layout of the building is seen in Fig. 6.2.

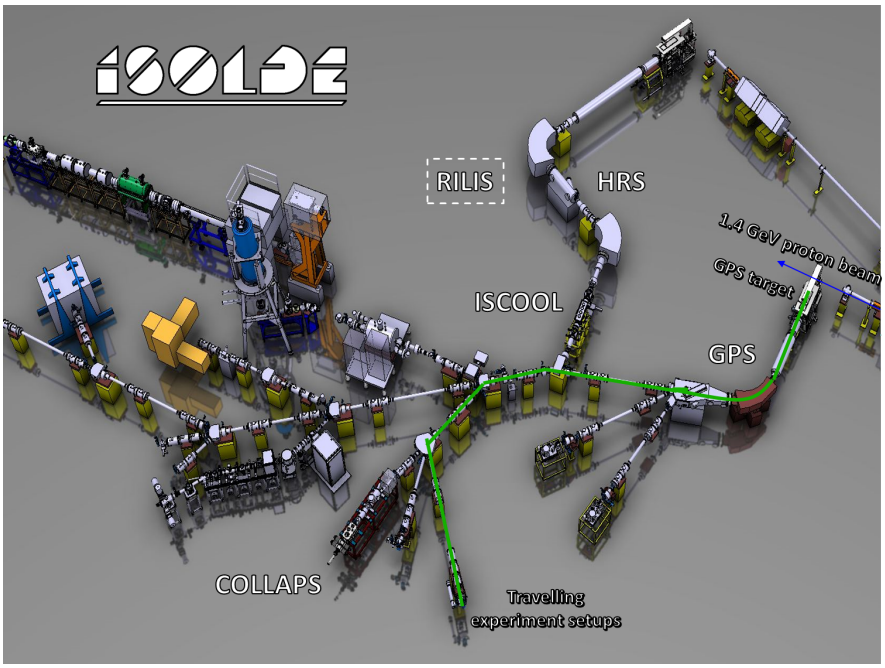

Figure 6.2: ISOLDE layout, showing the beam pathway from the GPS target. Figure adapted from [61].

The facility makes use of the two mass separators which provide high-purity beams to a number of different experiments. To this day, ISOLDE is capable of producing more than 1300 different isotopes across 73 different elements for experimental studies.

The Bi isotopes were produced by impinging a 1.4 GeV proton beam onto a uranium carbide (UC_x) target. The Bi isotopes were then ionised to a 1+ charge state using a three step laser ionisation scheme, accelerated using an electrostatic potential and then mass separated. The mass separated ion beam is then transferred to one of the detection setups: The Windmill (WM), ISOLTRAP's Multi-Reflection Time-Of-Flight Mass Separator (MR-TOF-MS) or the ISOLDE Faraday Cup (FC). In Fig. 6.2, the path of the Bi ions is shown for the case of using the WM setup. The choice of detection system is dependent upon many factors including isotope half life, branching ratio, decay mode and beam intensity.

The FC can be used in cases where the ion beam current is of the order of pA. The WM was used to perform decay studies as well as measurements of HFS and isotopes shifts for short lived alpha decaying isotopes, The ISOLTRAP MR-TOF-MS was used to measure HFS and isotope shifts of longer lived/stable isotopes or in cases when there is large isobaric contamination present. Fig. 6.3 gives a schematic overview of the beam production as well as the three different detection setups. The following sections provide more detailed descriptions of these individual stages.

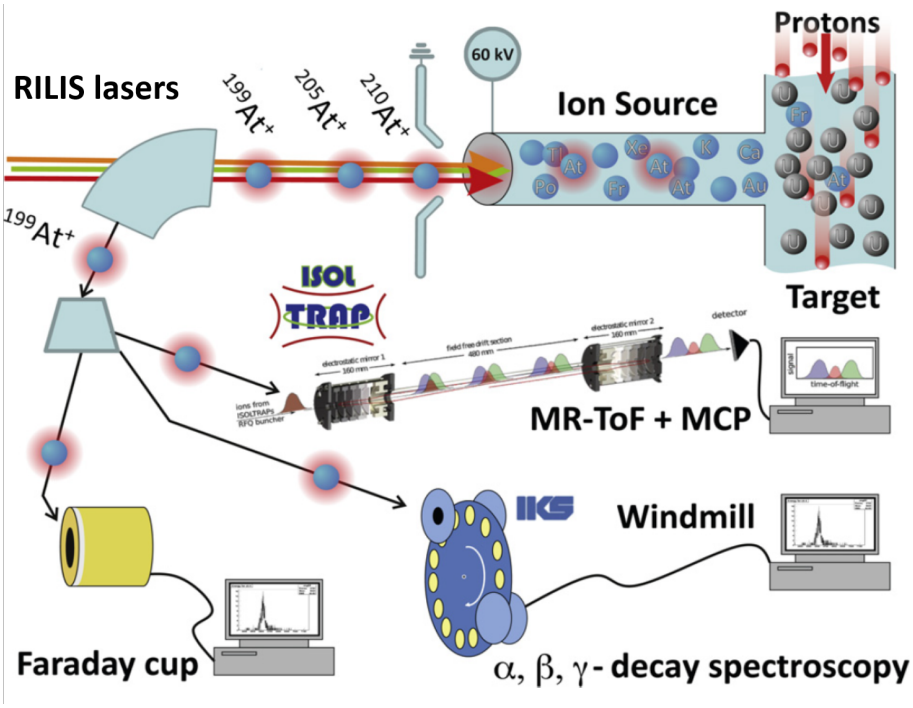

Figure 6.3: Schematic diagram of the in-source resonance ionisation spectroscopy of the At isotopes. This shows the proton beam impinging on the uranium carbide target, the resonant ionisation using the RILIS lasers, the mass separation using the GPS dipole magnet as well as the implantation into one of the three detection systems: the Faraday cup, the windmill and the ISOLTRAP MR-TOF. Figure taken from [62].

6.2 Beam production

At the ISOLDE facility, a 1.4 GeV proton beam is delivered from the PSB. This beam consists of pulses of 2.4 μs in length, with spacings of 1.2 seconds between them, providing an average current of 2 μA. The beam is organised into a logical sequence known as a supercycle (SC) which typically contains 35-40 proton pulses. These pulses are distributed

across different facilities at CERN. During experiment, ISOLDE will receive around 25-50% of these pulses depending on the isotope under investigation.

During the Bi experiments, the proton beam was impinged upon 50 g/cm^2 UC_x targets generating high energy collisions. These high energy collisions result in the production of many isotopes via three different types of reactions, shown in Fig. 6.4.

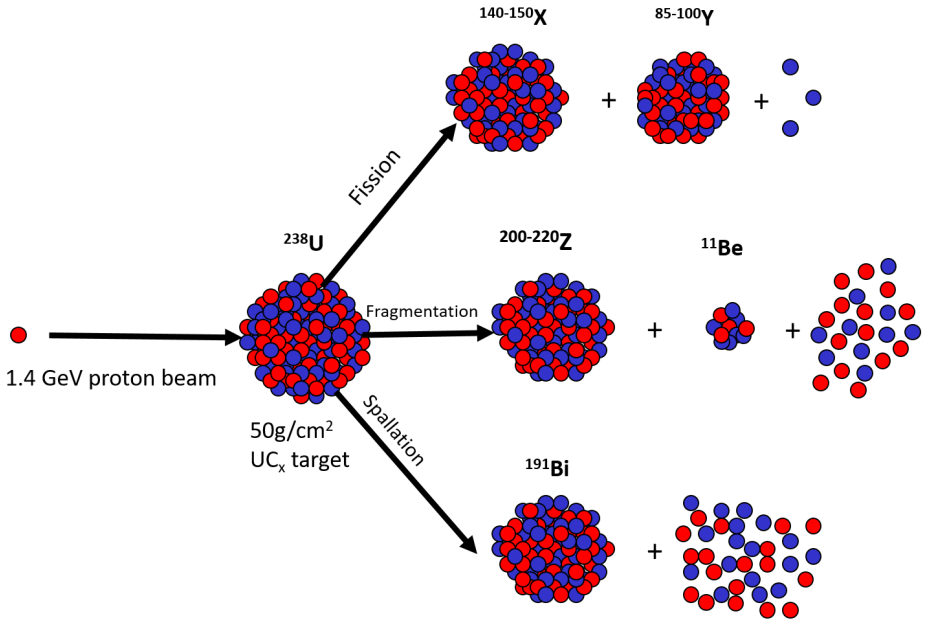

Figure 6.4: Schematic diagram of the reaction mechanisms used to produce the different isotopes at ISOLDE (red circles: protons, blue circles: neutrons).

The 3 mechanisms are:

·**Fission** The collision excites the target nucleus above the fission barrier. As a result, nuclear fission occurs splitting the parent nucleus into two daughter nuclei and a number of neutrons. This mechanism is useful for producing neutron rich nuclei.

·**Fragmentation** This type of reaction is useful for producing lighter nuclei such as ^{11}Be. The target nucleus breaks down into a light and a heavy nuclei and a number of free nucleons with the heavy nucleus having a mass comparable to that of the target nucleus.

·**Spallation** This is the reaction used to produced the neutron deficient Bi nuclei. In spallation, firstly a relativistic proton collides with a target nucleus, exciting multiple nucleons

to higher energy states. Then the nucleus de-excites itself by evaporating off tens of nucleons.

The reaction products are neutralised and their remaining kinetic energy is absorbed by the target. Extraction of nuclides occurs via thermal effusion and diffusion into the hot cavity via the transfer line. The release time is reduced by heating the target, transfer line and hot cavity to $> 2300°C$. The neutral atoms may then be ionised within the hot cavity of the ion source [63, 62].

6.3 RILIS

The resonant ionisation laser ion source (RILIS) [64] is the most commonly used ion source at the ISOLDE facility, with over 50% of the experiments making use of it due to its high efficiency and isobaric selectivity. RILIS is capable of producing ion beams for more than 35 different chemical elements. For each element a specific ionisation scheme is required [65, 66].

For Bi isotopes, three lasers are used to excite an atom from the ground state, through two intermediate excited states, then to the continuum, leaving a 1^+ charge state ion. After ionisation, the ions are accelerated by a 30-60 kV electrostatic potential. The ion beam was then mass separated before being delivered to one of the three experimental setups in the ISOLDE hall.

To maximise ionisation efficiency, the pulsed laser must have a repetition rate of 10 kHz. This repetition rate ensures that every atom is exposed to a minimum of one pulse of laser light, increasing the probability of an interaction between the laser's photon and the atom.

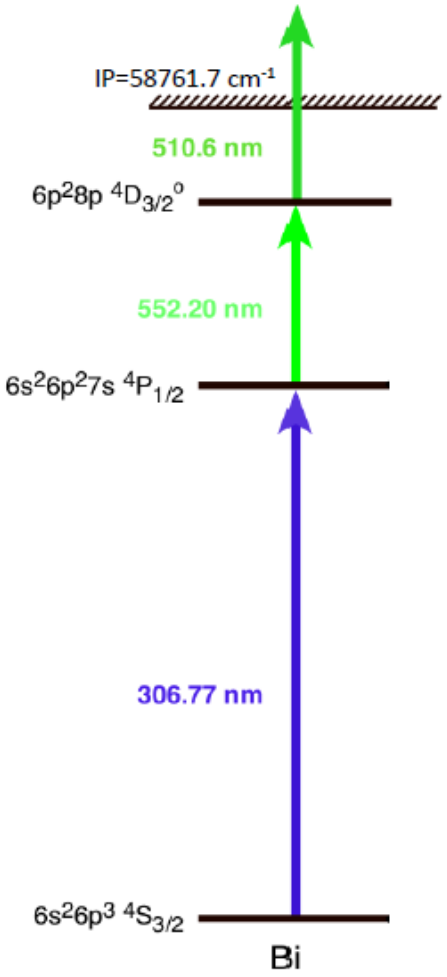

Figure 6.5: The three step resonant ionisation scheme used to produce the Bi beam during the IS608 experiment runs that took place in June 2016,2017 and 2018. The first laser step was frequency scanned in order to produce the HFS spectra. Figure adapted from [67].

6.4 Mass Separation

The ISOLDE facility has two separators, each equipped with their own target: The General Purpose Separator (GPS) and the High Resolution Separator (HRS). The GPS is the smallest of the two separators with its centrepiece being a double focussing 70^o magnet with a bending radius of 1.5m, producing a mass resolving power of $m/\triangle m \sim 2400$ [68]. The GPS allows selection of three ion beams within the mass range of $\pm 15\%$ from the central mass allowing three different beams to go to three separate experimental setups in the hall.

The HRS consists of two bending magnets which produce a mass resolving power of $m/\triangle m \sim 7 - 8000$. Unlike the GPS, the HRS has no switchyard for mass separation and so only a single beam can be delivered to a single experimental setup in the hall.

A merging switchyard then feeds the HRS and GPS beam lines into the ISOLDE central beam line. This beam line goes to the experimental hall, allowing the beam to be steered to a number of different experimental stations where a user's setup can be installed.

6.5 Photo-ion detection

For each isotope under investigation, the production yield, decay properties and levels of isobaric contamination are all different. As a result, multiple methods of photo-ion detection are required. The three different methods used for the Bi isotopes are described below.

Faraday Cup

The Faraday cup (FC) is typically used as a beam diagnostics tool for ion current measurements. However, the FC was used to measure ^{209}Bi as it is a stable isotope with a high production yield. During a laser scan, the integration time of the FC is fixed for each laser step and the average ion current measured, producing the HFS spectra.

Windmill Decay Station

For radioactive beams, their specific decay radiation can be used as an efficient and selective means of photo-ion detection. The ISOLDE tape station, a device typically used for yield measurements, can be used to measure β or γ radiation for isotopes with a half life longer than 100ms [62]. For shorter lived isotopes, the KU-Leuven Windmill decay station was used [69]. The ions were implanted into one of the ten carbon foils of $20\mu g/cm^2$ thickness and 6mm in diameter which were produced at the GSI laboratory [70]. These ten carbon foils were mounted on a rotatable wheel. A diagram of the Windmill setup is shown in Fig. 6.6. At the implantation position, there were two silicon detectors. One of these was an annular detector, Si1, positioned 7mm upstream, with an active area of 450mm^2 and a thickness of 300μm with a central hole of 6mm in diameter to allow passage of the beam. The second

silicon detector, Si2, was a standard detector with an active area of 300mm^2 and 300μm thickness situated 4mm downstream of the foil. This gave a total detection efficiency of 34% at the implantation position [30]. After a fixed number of SC, the wheel is rotated and the irradiated foil was moved between the second pair of silicon detectors. These were two Passivated Implanted Planar Silicon (PIPS) detectors, named Si3 and Si4. This allowed the measurement of α decays of long lived daughter products.

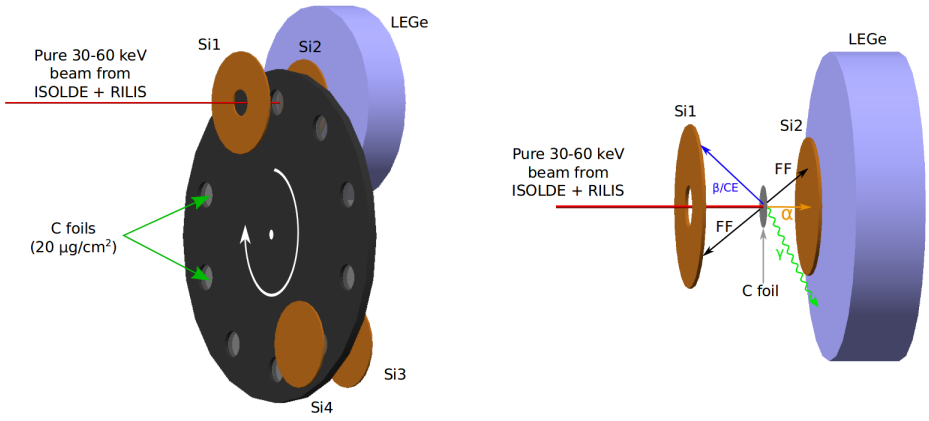

Figure 6.6: Model of the Windmill setup. Left: Position of the four silicon detectors (brown), rotatable wheel (black), carbon foils (grey) and the Low-Energy Germanium detector (LEGe, blue). The germanium detector positioned at a right angle to the beam is not shown in this diagram. Right: Zoomed in view of the implantation site with α-particles (orange), β/conversion electrons (blue), γ rays (green) and fission fragments (black) originating from the nuclei implanted into the foil. Figure taken from [11].

Two Germanium detectors were placed outside the WM chamber in order to detect γ rays. There was a low-energy planar germanium detector, named Ge1, situated directly behind Si2. The second, Ge2, was situated 90 deg to the beam direction, to the side of the chamber.

ISOLTRAP's MR-TOF-MS

At the ISOLDE facility, both mass separators have a mass resolving power sufficient to remove neighbouring isotopes from the radioactive beam. However, one of the major difficulties for many experiments at ISOL facilities is isobaric contamination. This can arise from the hot environment of the ion source resulting in surface ionisation. In order to suppress these isobars, one requires a mass resolving power of $m/\triangle m \sim 10^4$. To add to this, isotopes far from

stability are constrained by a large decrease in production yield as well as a reduction in half-life. This lowers the relative intensity ratio between the ions under study and the isobars. For longer lived isotopes with no decay to measure and a large amount of isobaric contamination, ISOLTRAP's Multi-Reflection Time-Of-Flight Mass-Spectrometer (MR-TOF-MS) [71] was used to measure the isotope shifts and the HFS.

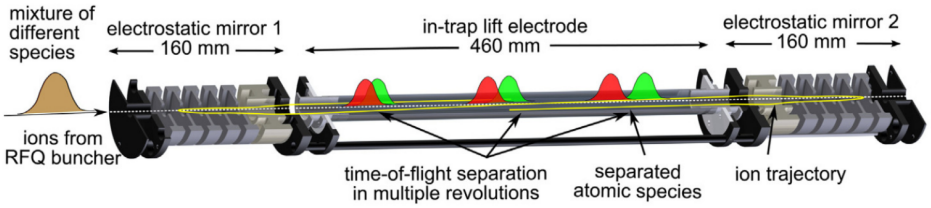

Figure 6.7: Schematic diagram of ISOLTRAP's Multi-Reflection Time-Of-Flight Mass Spectrometer. Figure taken from [71].

This device is shown in Fig. 6.7 and discussed in detail in [71]. ISOLTRAP's MR-TOF-MS consists of two electrostatic ion-optical mirrors, both 160 mm in length, surrounded by shielding electrodes and separated by a 460 mm long cavity. Firstly, the mass separated ion beam is bunched and cooled using the helium buffer gas filled Radio Frequency Quadrupole (RFQ) cooler/buncher. The ions are then injected into the cavity at an energy of 3.2 keV [72], where they are reflected back and forth between the mirrors, thousands of times, resulting in a long time of flight. This separates the different ions according to their mass to charge ratio, resulting in a mass resolving power of $m/\triangle m \approx 10^5$. This whole process typically takes 30ms (in fast measurement cycle). Once the mass separation occurs, the isotope under investigation was selected using a fast timing electrical deflector and the number of ions is then measured using a multichannel plate detector.

6.6 Scanning the hyperfine structure

When scanning the hyperfine structure of the Bi isotopes using in-source resonance ionisation spectroscopy, a three step laser ionisation scheme was chosen. In this scheme, a frequency tripled Ti:Sa laser was scanned in a 'high resolution' mode using a narrow-band (NB) laser with a $\approx$ 1 GHz linewidth (before tripling). The laser/atom interaction region is in the hot cavity (>2000 K), and so the thermal motion of the atoms gives rise to Doppler broadening,

which further limits the resolution by an additional 1 GHz. The other transitions are fixed in frequency and provided by broad-band (BB) lasers, which are tuned to give maximum ionisation efficiency. These BB lasers have a linewidth of over 100 GHz, which is usually larger than the IS or HFS effects. This allows all isotopes and isomers of a chosen element to be ionised with equal efficiency.

The HFS is scanned in discrete steps. For a given step in a scan, the NB laser is tuned to the desired frequency by the tilting of two etalons [73]. Once this frequency has stabilised the implantation of the beam into one of the three detection setups commences and the data acquisition begins, with the time of the laser step corresponding to the length of data acquisition. The wavelength was recorded using two High Finesse/Angstrom WS/7 wavemeters installed in the RILIS laboratory [74]. Over the course of a step, the laser frequency is continuously monitored and the average measurement is taken as the frequency. At the end of each laser step, the laser was tuned to a new frequency. Whilst this occurs the data acquisition prepares for the next step (for the Windmill, the wheel is rotated, introducing a fresh foil at the implantation position). The start and stop of data acquisition during a laser step, as well as the movement of the Windmill wheel in between the step, was controlled using digital clocks which are synchronised with those from the CERN PSB via an electronic logic system.

The neutron-deficient Bi isotopes below N=109 are short-lived and α-decaying, therefore the Windmill decay station was used to measure their HFS. During a laser scan, measuring the number of α decays under the chosen α line provides a way of determining ionisation efficiency across the scan. In this way, it is possible to measure the HFS of the ground and isomeric states in a given isotope, provided they have different α-decay energies. An example of this can be seen in the plot in Fig. 6.8, which shows the number of α counts as a function of laser wavenumber for a scan of ^{191}Bi. The HFS of the two isomers can be investigated by gating on their individual α-decay energies.

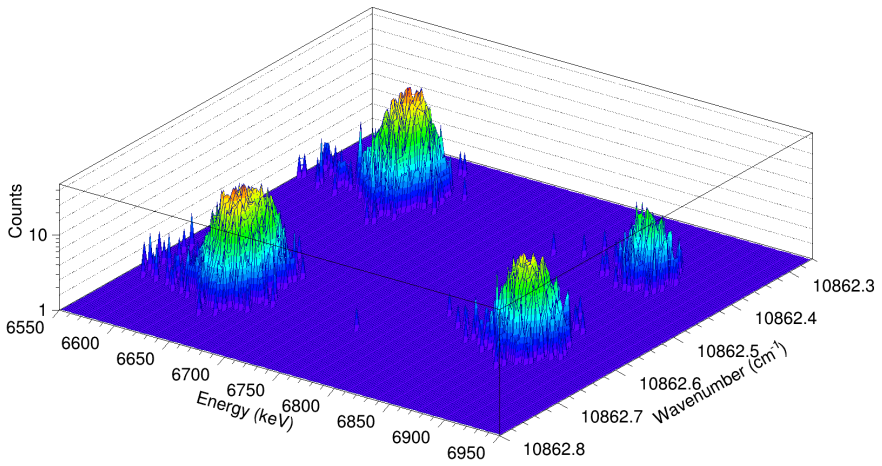

Figure 6.8: Surface plot of the ^{191g,m}Bi α-decay events measured in the windmill decay station, against the laser wavenumber of the scanning laser. Two pairs of peaks can be seen corresponding to the two characteristic α decays from the individual isomers. The difference in the structure of these two pairs arises due to the difference in the structure of the two nuclear isomers.

6.7 Windmill Data Acquisition

As discussed in the previous section, the WM wheel rotates after every laser step. During a laser scan, the number of SCs per laser step is fixed throughout the scan. This number is dependent on the half-life and production yield of the isotope under investigation.

The collection of data was performed using the Digital Gamma Finder (DGF), revision 4C, digital electronic modules from XIA [75]. Each module had 4 input channels and an internal clock for processing and time stamping each 'event'. Each 'Event' recorded in the modules was given a number of stamps which were then used in the analysis of the experimental data.

· **Energy:** Energy of the decay radiation detected is proportional to the size of the electronic signal received by the module.

· **Identification Stamp:** States which module and channel the signal was received, allowing identification of the event (i.e. a decay detected in the Si or Ge detectors or a time signal from one of the internal clocks).

· **Time Stamp:** Taken from the module's internal clock, stating the time of the event to the precision of 25ns.

During IS608, a total of 8 modules were used, 6 being utilised for the 6 different detectors. For the remaining two cards, one of the cards recorded clock logic signals used to control and synchronise the WM wheel rotation and the data acquisition. The start of a measurement step of a HFS scan, a proton pulse being sent to ISOLDE, the end of DAQ, and the movement of the WM wheel are all recorded by this. The other card was dedicated to a 100 Hz pulser. This monitored the fractional dead time during data acquisition as well as the total live time of each run. The IGOR software package by wavemetrics was used to ensure all the internal clocks were synchronised as well as control the modules remotely [76]. To reduce dead time from the readouts, a logic gate was used to synchronise the writing of the data from the module buffers to the PC hard drive.

Chapter 7

Results

This chapter presents the results from the laser spectroscopic studies of neutron-deficient Bi isotopes. The HFS constants and isotope shifts of $^{187-189,191}$Bi will be shown, from which the electromagnetic moments and changes in mean-square charge radius for each isotope (and isomers) can be extracted. The data were taken during the IS608 experimental runs, by the Windmill-RILIS-ISOLTRAP collaboration in June 2016 and June 2017 at the ISOLDE facilty, CERN. The contribution of the author is online analysis during the experimental campaign as well as the offline analysis, producing the final HFS spectra.

As discussed in Section. 6.3, RILIS ionizes the Bi atoms to a 1^+ charge state using a three step laser ionisation scheme shown in Fig. 7.1. The first step was excited using the frequency tripled Ti:Sa laser operated in narrowband mode (linewidth of $\backsim$0.8 GHz, before tripling). The second step was performed using a broadband DMK MSS dye laser. A broadband solid state Nd:YVO4 laser was employed for the final step. Further details of the RILIS laser system can be found in Ref [64]. The atomic spectroscopy measurements of the different Bi isotopes were performed by scanning the $6p^3\ ^4S_{3/2} \longrightarrow 6p^2 7s\ ^4P_{1/2}$ transition (λ=306.77 nm). For a given laser frequency, the ionisation efficiency was determined using one of three different ways: measuring the Radioactive Ion Beam (RIB) current using a Faraday cup, counting ions using ISOLTRAP's MR-ToF-MS or determining the number of α-decays using the Windmill decay station.

7.1 Expected HFS spectra

The right-hand side of Fig. 7.1 depicts a schematic view of the expected HFS of the ground I=9/2 and excited I=1/2 states in ^{191}Bi. The coupling of the nuclear spin I=9/2 with the atomic spin, J, results in splitting into the hyperfine levels. As can be seen in Fig. 7.1, the J=3/2 ground atomic state is split into 4 hyperfine levels of F=3,4,5 and 6, whilst the J=1/2 excited atomic state is split into 2 levels of F'=4 and 5. The blue arrows indicate allowed transitions. Fig. 7.2 shows a HFS spectrum obtained for the $I = 9/2^-$ ground state of ^{191}Bi. The blue line shows what one would expect without Doppler broadening, with a spectral resolution of $\backsim$50 MHz. The red line shows the HFS spectrum when using an in-source laser spectroscopy method, with a resolution of $\backsim$3 GHz. The hyperfine parameters a and b used in these fits were extracted from fits to the experimental data, which will be discussed in the following sections.

The intensity of each hyperfine transition, $I_{F_iF_j}$ relative to the intensity of the unpertubed electronic transition, $I_{J_iJ_j}$, is determined by:

$$\frac{I_{F_iF_f}}{I_{J_iJ_f}} = (2F_i + 1)(2F_f + 1) \begin{Bmatrix} F_i & F_f & 1 \\ J_f & J_i & I \end{Bmatrix}^2 \tag{7.1}$$

where the i and f subscripts denote the initial and final states, respectively, and {...} is a Wigner 6-j symbol.

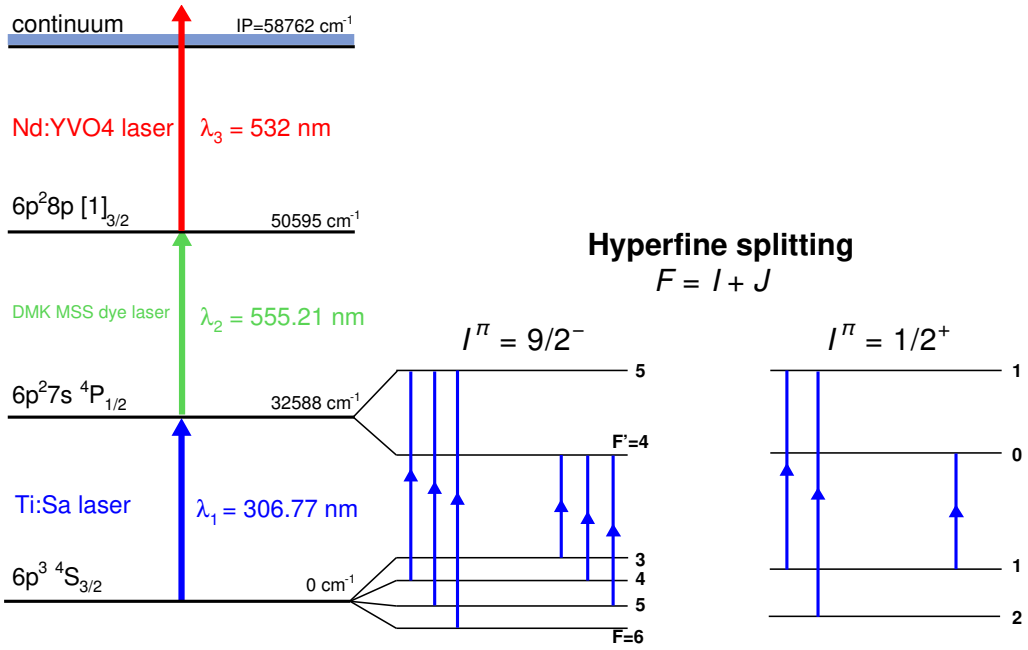

Figure 7.1: The three-step laser ionisation scheme used for Bi atoms during the IS608 campaign (left), and the hyperfine splitting resulting from the coupling of the atomic electron and nuclear spins for both the I=9/2 and 1/2 states in ^{191}Bi (right). The blue arrows indicate the allowed transitions between the initial and final states of the scanned 306.77 nm laser transition. The size of the hyperfine splitting is not to scale.

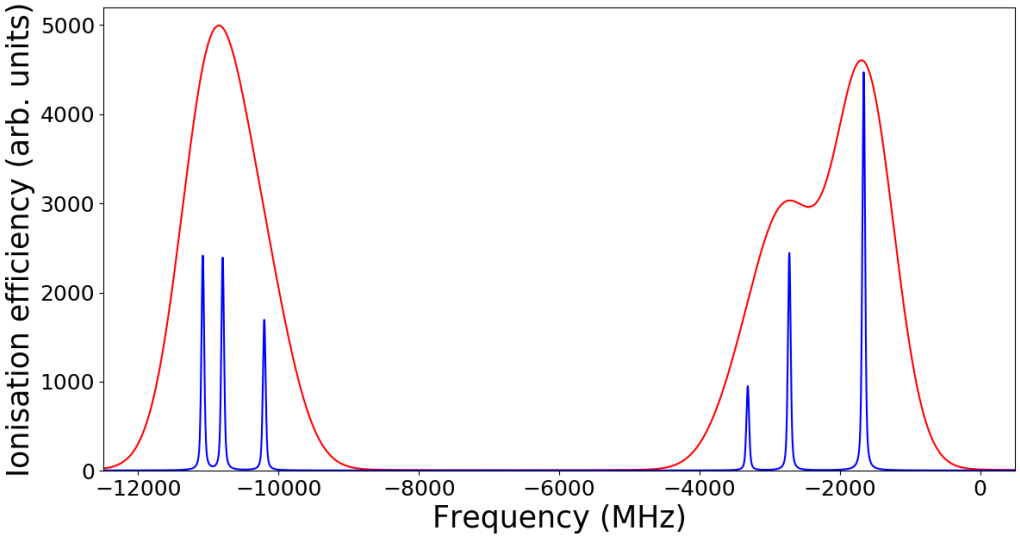

Figure 7.2: HFS spectra for the ground state of isotope ^{191}Bi. The red line shows what one would expect when employing an in-source laser spectroscopy method, such as the one used throughout the IS608 campaign, with a Doppler broadening of 850MHz. The blue line shows the HFS spectrum expected without Doppler broadening. The hyperfine factors a and b used to produce these two spectra were taken from the fitting results of ^{191}Bi HFS spectra, which will be discussed in the following sections.

7.2 Calibration of silicon detectors of Windmill

During the online analysis, the silicon detectors were calibrated using the ^{241}Am α source [77]. Due to the Am source not accounting for the carbon foil thickness, this source was only used for the initial calibration. In the offline analysis calibrations were carried out for every laser scan using the α-decays from the Bi nuclei and their daughter isotopes. Figure 7.3 shows the calibration results of the silicon detectors at implantation position (Si1 and Si2). This calibration was performed using the α-decay energies of ^{191}Bi [78].

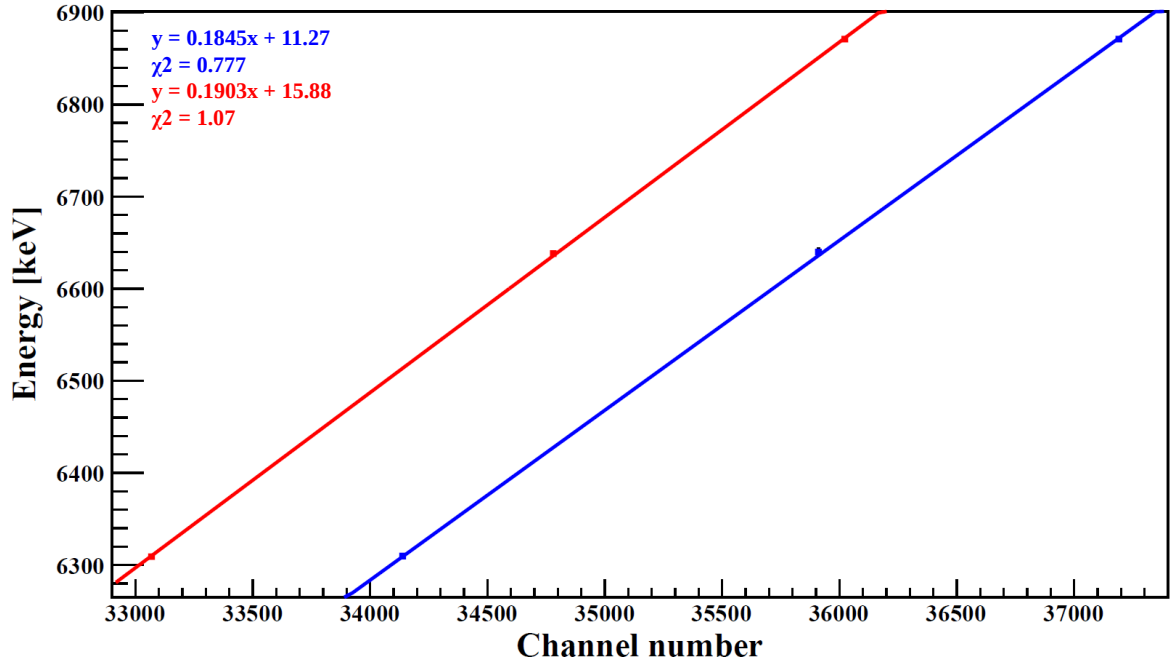

Figure 7.3: Energy calibration for Si1 (blue) and Si2 (red) detectors. The α-decay energies used are: ^{191}Bi E$_\alpha$= 6309(3), 6639(4) and 6871(3) keV [78]. The data were fitted with first order polynomials.

7.3 Producing HFS from Windmill laser scans

In the case of the isotopes $^{187-189,191}$Bi, the HFS spectra were extracted by counting the number of events under specific alpha lines measured by the Windmill decay station, for each laser frequency step throughout the scan. After each scan, one can apply gates on the characteristic α-decay of the isotope under investigation to produce the HFS spectra. Table. 7.1 shows the number of laser scans carried out for each isotope. This section details the

Table 7.1: Details of the number of laser scans and the amount of laser steps per scan shown for each Bi isotope investigated during the experimental campaign IS608. With the exception of some laser scans of ^{188}Bi, all other laser scans were carried out in 2016 using the HRS separator.

Isotope	Laser Scan No.	Supercycles per step	Number of laser steps
^{187}Bi	Scan 1(2016, HRS)	6	26
	Scan 2 (2016, HRS)	6	44
	Scan 3 (2016, HRS)	6	45
^{188}Bi	Scan 1 (2016, HRS)	1	119
	Scan 2 (2016, HRS)	2	123
	Scan 3 (2016, HRS)	4	60
	Scan 4 (2016, HRS)	3	74
	Scan 5 (2016, HRS)	3	123
	Scan 6 (2017, GPS)	3	65
	Scan 7 (2017, GPS)	5	65
	Scan 8 (2017, GPS)	5	54
	Scan 9 (2017, GPS)	4	39
^{189}Bi	Scan 1 (2016, HRS)	1	107
	Scan 2 (2016, HRS)	1	86
	Scan 3 (2016, HRS)	1	90
	Scan 4 (2016, HRS)	1	88
^{191}Bi	Scan 1 (2016, HRS)	1	108
	Scan 2 (2016, HRS)	1	91
	Scan 3 (2016, HRS)	1	90

methods used to extract the final HFS spectra for each Bi isotope.

7.4 ^{191}Bi

In each decay scheme shown in this chapter unconfirmed (confirmed) spins of nuclear states will be shown with brackets (no brackets). Throughout the text the brackets are omitted. The α-decay scheme of ^{191}Bi is shown in Fig. 7.4. Data were taken from Refs. [50, 79]. The $9/2^-$ ground state decays by two branches, while the $1/2^+$ isomer state has a single decay at 6871 keV.

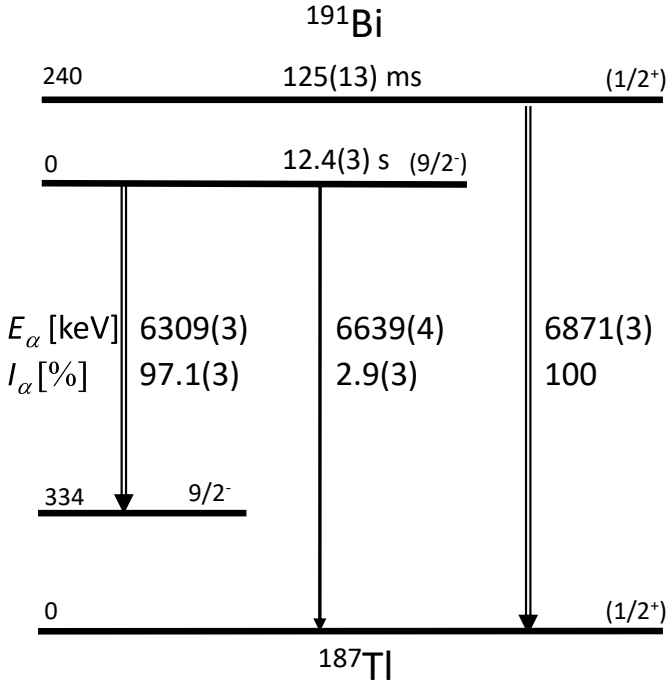

Figure 7.4: α-decay scheme for ^{191}Bi. Shown are the α-decay energies (E_α) and relative intensities (I_α). These values were taken from Refs. [50, 79].

Due to the high predicted yield (45000 ions/s) of ^{191}Bi, measurements of the HFS were attained using just three scans consisting of 1 supercycle per laser step. Additionally, there is no α-decaying isobaric contamination at mass A=191, resulting in a pure ^{191}Bi α decay spectra.

Alpha decay spectra

Fig. 7.5 shows the resultant α-decay spectrum measured at the implantation position using Si1 and Si2 during scan 1.

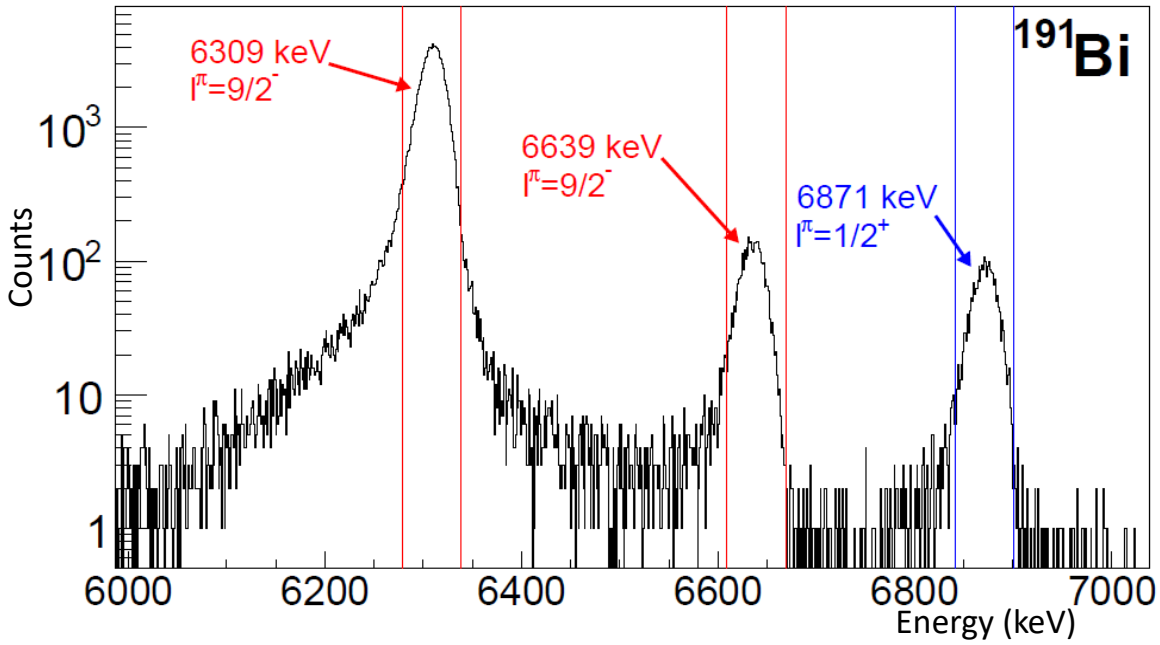

Figure 7.5: α-decay spectrum from laser scan 1 of ^{191}Bi measured at the implantation position using Si1 and Si2. The peaks are labelled with their decay energies in keV, as well as the spin and parity of the corresponding ^{191}Bi states. The respective gating conditions used to produce the HFS spectra are indicated by the vertical lines with colours matching the two different states.

The $9/2^-$ ground state is long lived and so its α decays will still be present after the 0.8 s time interval required for the carbon foil to move to the decay position between Si3 and Si4. Fig. 7.6 shows the energy spectra measured using Si3 and Si4 at the decay position in scan 1.

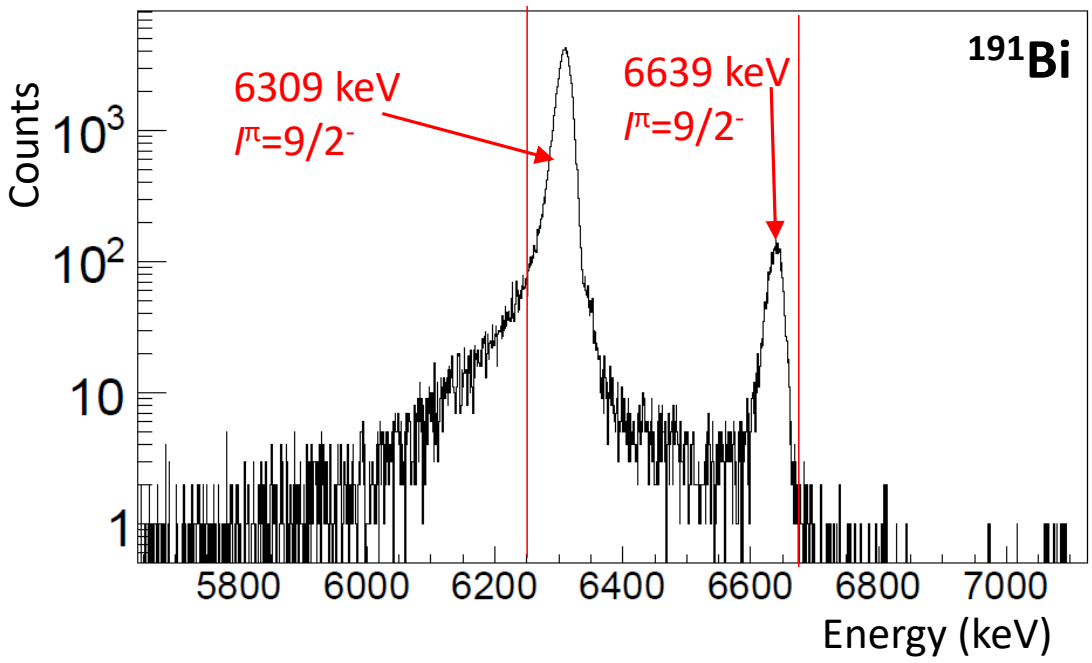

Figure 7.6: α-decay spectrum from a laser scan of ^{191}Bi measured at the decay position using Si3 and Si4. The peaks are labelled with their decay energies in keV, as well as the spin and parity of the ^{191}Bi states. The energy gate used to produce the I=9/2 ground state decay curve are indicated by the red vertical line.

Extraction of the HFS spectra

Energy gates were applied to the 6309 keV and 6639 keV α-decay peaks in Si1 and Si2 to produce the $9/2^-$ ground state HFS spectra and to the 6871 keV to determine the $1/2^+$ isomer state HFS spectra. Fig. 7.7 shows the HFS spectra for these two states produced from scan 1.

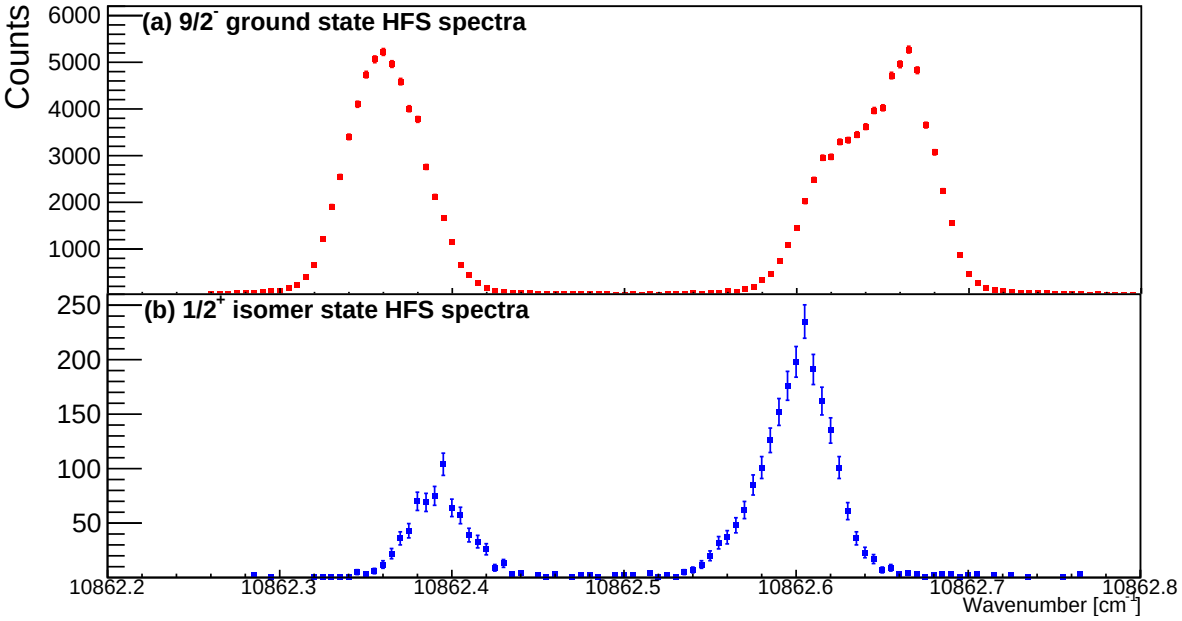

Figure 7.7: Extracted HFS as a function of laser wavenumber for scan 1 of ^{191}Bi: (a) I=9/2 ground state and (b) I=1/2 isomer state. For the ground state, energy gates of 6279-6339 keV were applied to the 6309 keV and gates of 6609-6669 keV to the 6639 keV α-decay lines measured using Si1 and Si2. For the isomer state, energy gates of 6841-6901 keV were applied to the 6871 keV α-decay lines measured with Si1 and Si2.

Measuring half lives

From the data taken with the silicon detectors during a laser scan, it is possible to measure the half lives ($t_{1/2}$) of different states. Fig. 7.8 shows the time distribution of α decays measured in Si3 and Si4 across every laser step in the leftmost peak of a hyperfine structure of ^{191g}Bi during laser scan 1, with energy gates applied to both 6309 and 6639 keV lines of the $9/2^-$ ground state. The red lines indicate the start of each laserstep in the scan and black data points show the α decays of the $9/2^-$ ground state for each laserstep. Shifting the data from each laser step to the movement of the WM wheel (corresponding to time=0) allowed the half life to be measured from a decay curve using all α decays observed in Si3 and Si4. Fig. 7.9 shows the extracted summed decay curve for the $9/2^-$ ground state from scan 1. An exponential fit was applied to extract $t_{1/2}$, giving a value of 12.46(8) s, more precise than the literature value of 12.4(3) s [78].

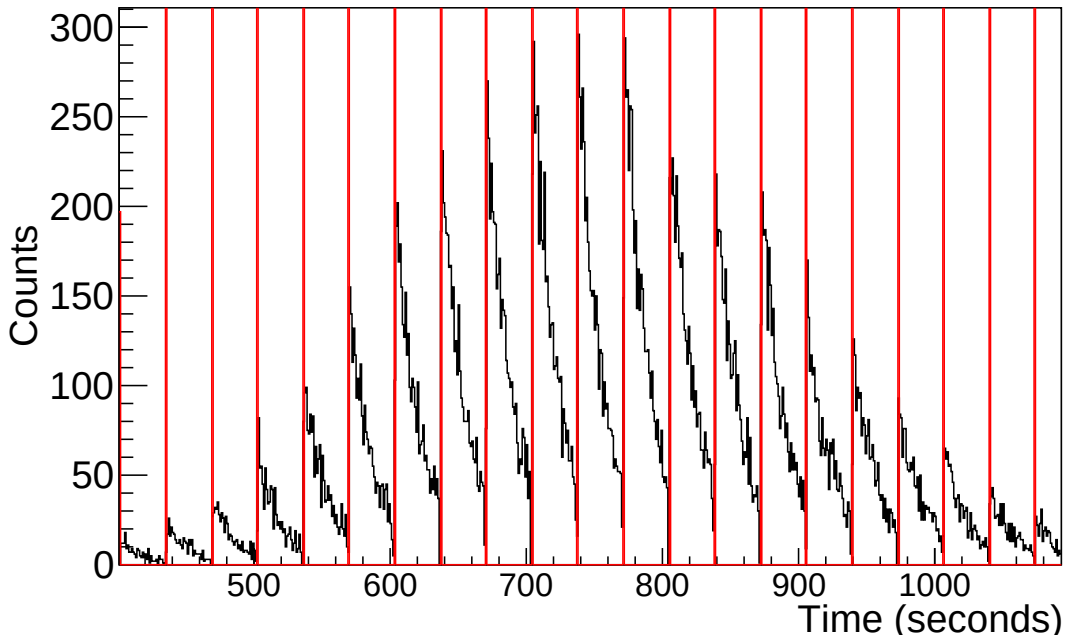

Figure 7.8: The time distribution of events in the 6279-6339 and 6609-6669 keV gates for α lines from the $9/2^-$ ground state, collected at the decay position (Si3 and Si4) showing the leftmost peak of the hyperfine structure of ^{191}Bi. The black line shows the number of measured α-decay events and the red lines indicate when the wheel of the Windmill was rotated. The Windmill rotation period is 0.8 seconds, which is the time required introduce the next foil.

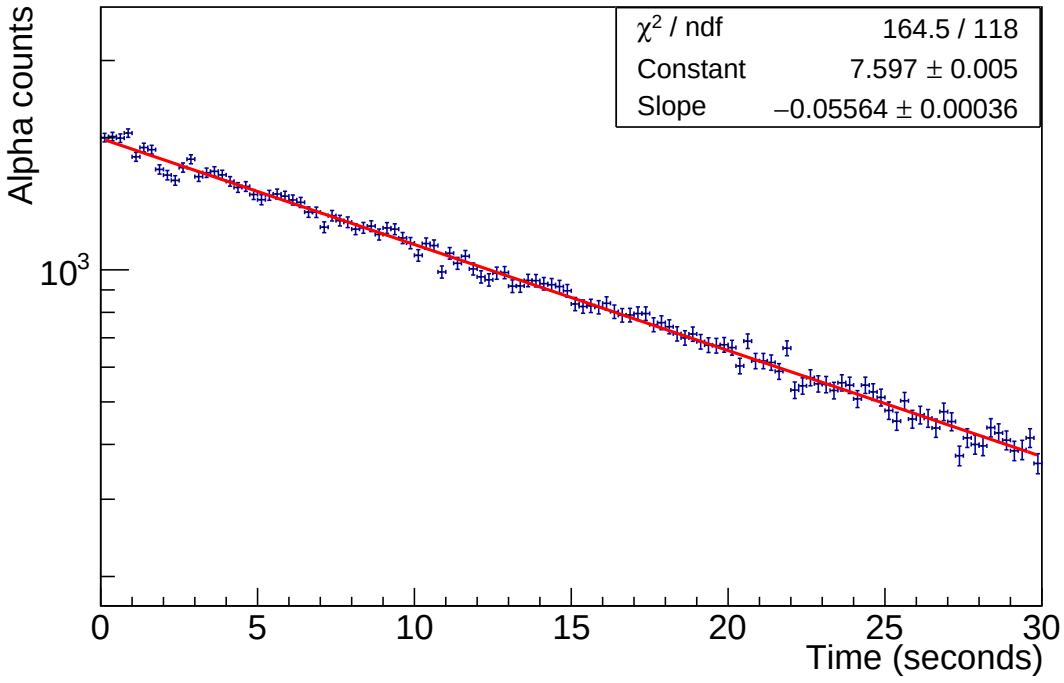

Figure 7.9: The extracted decay curve, for ^{191g}Bi, applying energy gates on α-decay events measured at the decay position using Si3 and Si4. The time=0 indicates the movement of the WM wheel (as shown by the red lines in Fig. 7.8), introducing the carbon foil to the decay position, between Si3 and Si4. The data were fitted using an exponential function.

7.5 ^{189}Bi

The α-decay scheme of ^{189}Bi is shown in Fig. 7.10. Data were taken from Refs. [53, 80]. The $9/2^-$ ground state decays by four branches, while the $1/2^+$ isomer state decays by three.

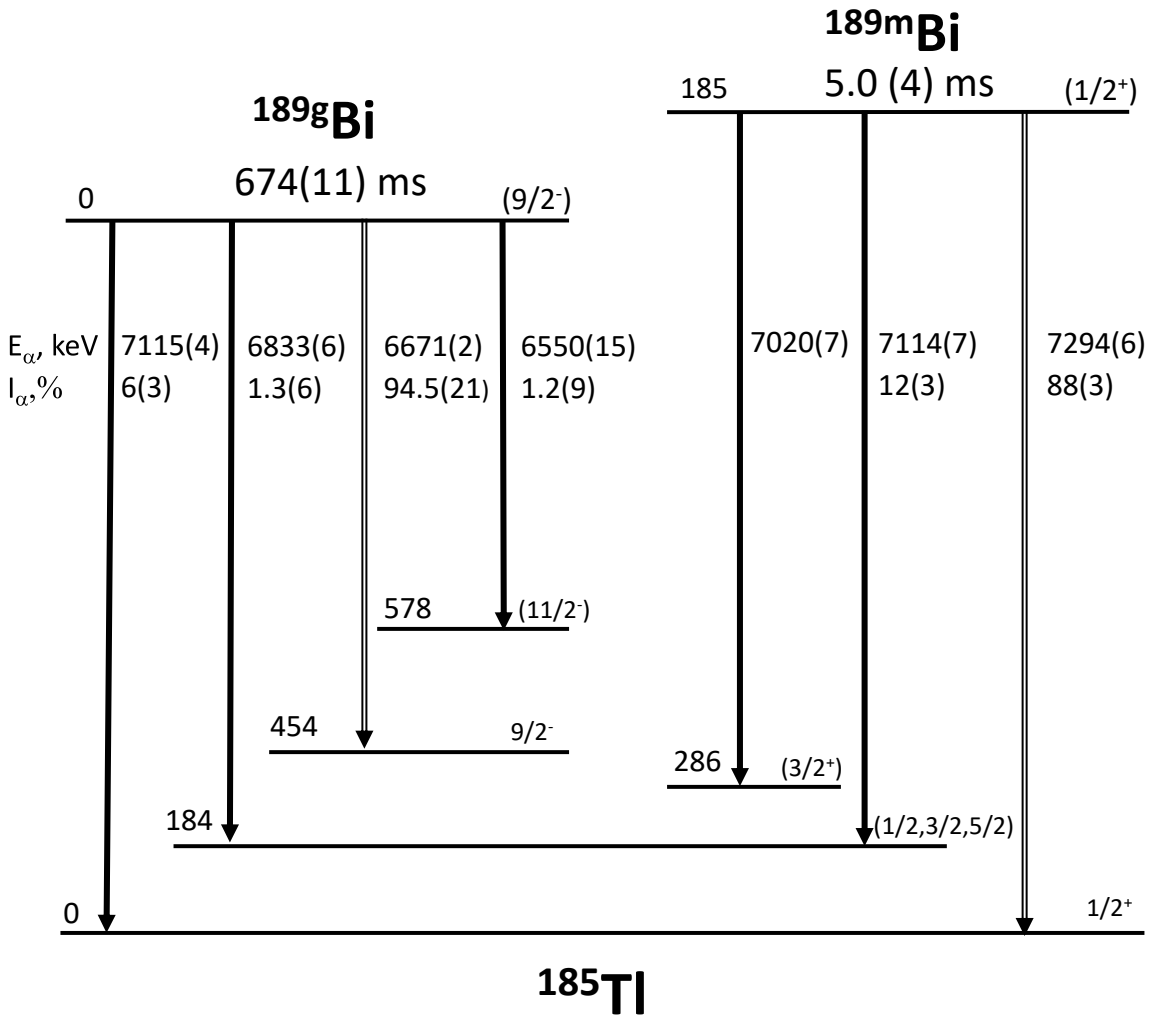

Figure 7.10: α-decay scheme for ^{189}Bi. Shown are the α-decay energies (E_α) and relative intensities (I_α) of each decay. These values were taken from Refs. [53, 80]

Fig. 7.11 shows the α-decay spectra produced from Si1 and Si2 during scan 3. The $9/2^-$ ground state had an expected yield of 2100 ions/s. As a result, measurements of this ground state could be achieved using a low number supercycles per laser step and so measurements were attained using 4 scans at 1 supercycle per laser step. Fig. 7.11 shows the α-decay spectra produced from Si1 and Si2 during scan 3.

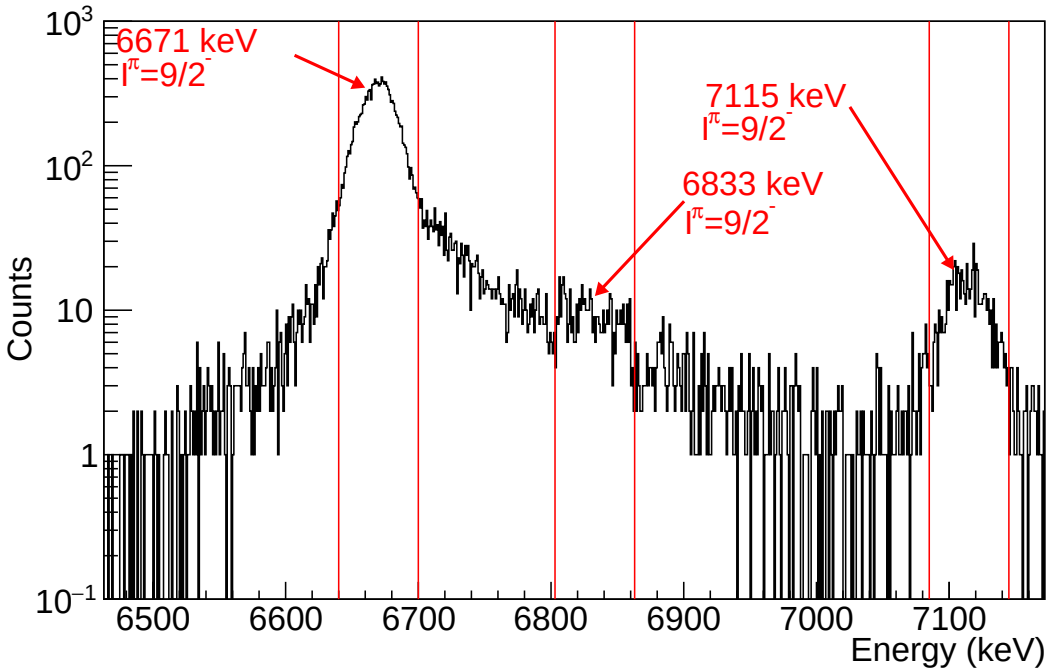

Figure 7.11: α-decay spectrum from laser scan 3 of ^{189}Bi measured at the implantation position using Si1 and Si2. The peaks are labelled with their decay energies in keV, as well as the spin and parity of the states of ^{189}Bi. The respective gating conditions used to produce the HFS spectra are indicated by the red vertical lines.

For the $9/2^-$ ground state, a value for the half life could not be extracted due to continuous implantation between proton pulses for every laser scan and the half life was too short to measure using Si3 and Si4. The $9/2^-$ ground state HFS was produced by applying gates to the 6671 and 7115 keV peaks. Fig. 7.12 shows the HFS spectra for this state.

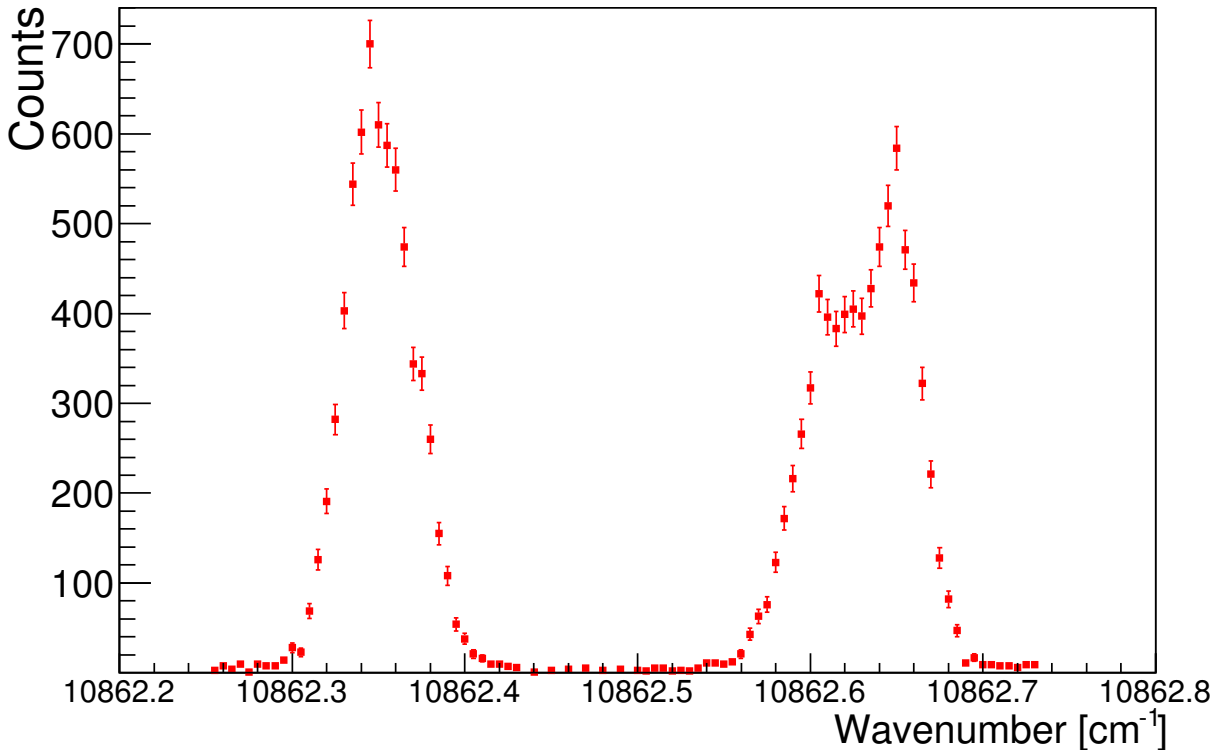

Figure 7.12: Extracted HFS as a function of laser wavenumber for scan 3 of ^{189g}Bi. Energy gates of 6641-6701 keV and 7085-7145 keV were applied to the 6671 keV and 7115 keV α-decays measured using Si1 and Si2, respectively.

7.6 ^{188}Bi

A total of 9 laser scans of ^{188}Bi were carried out, 5 in 2016 using the HRS, with the other 4 taking place in the 2017 experimental run using the GPS. Further details of each laser scan can be found in Table. 7.1. Nuclear spectroscopy studies of ^{188}Bi performed at the velocity filter, SHIP at GSI revealed two long lived isomer states interpreted as a high spin isomer $I^{\pi} = 10^{-}$ with a $\pi 1h_{9/2} \times \nu 1i_{13/2}$ configuration as well as tentatively assigning the second isomer state as $I^{\pi} = 3^{+}$ with a $\pi 1h_{9/2} \times \nu 3p_{3/2}$ configuration, based on the spin systematics for heavier odd-odd Bi nuclei [81]. Such states are well established in the odd-odd Bi isotopes ^{190,192,194}Bi [51]. However, some irregularities in the decay pattern of the low spin isomer of ^{188}Bi were observed. Based on the data presented in this thesis, the high spin 10^{-} isomer was confirmed but the interpretation of the low spin state changed to $I^{\pi} = 1^{+}$, these data will be presented in this section of the thesis. The α-decay scheme of ^{188}Bi, which accounts for this

work is shown in Fig. 7.13. The 10^- high spin (hs) isomer state decays by four branches. The 1^+ low spin (ls) isomer state decays by three branches.

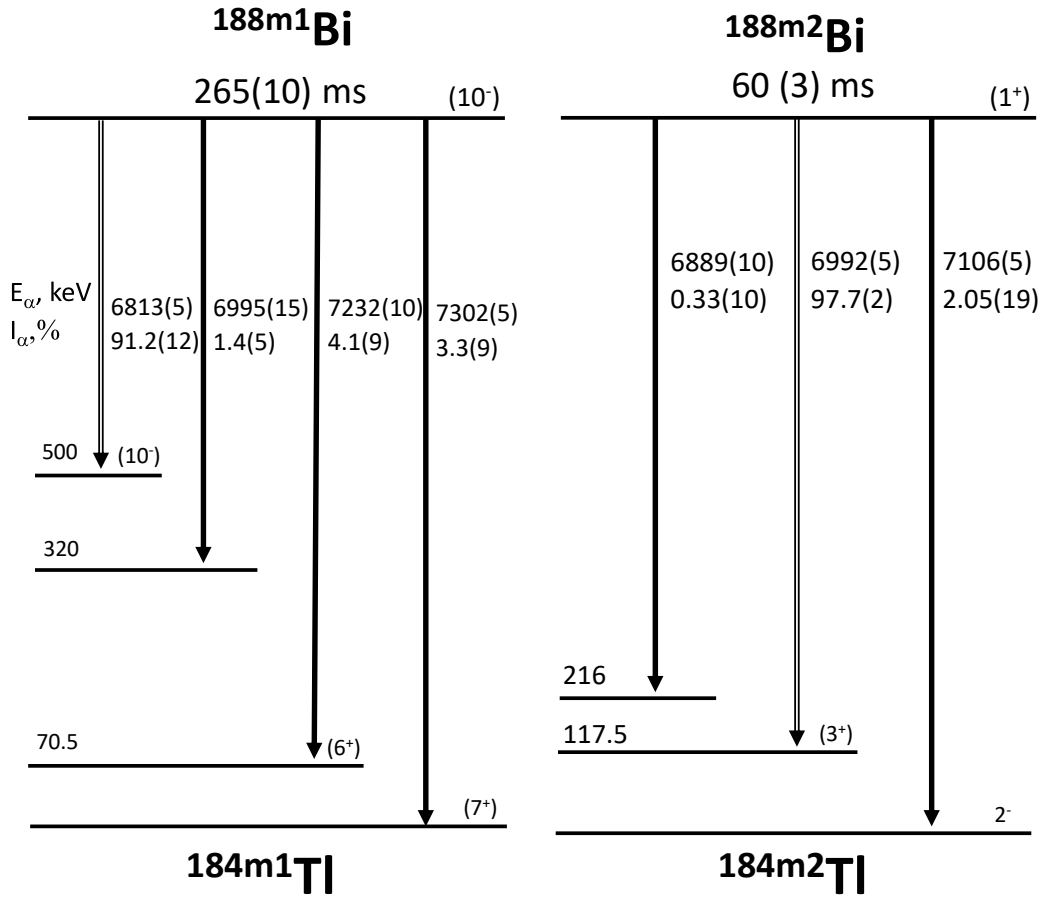

Figure 7.13: α-decay scheme for ^{188}Bi. Shown are the α-decay energies (E_α) and relative intensities (I_α) of each decay. These values were taken from Ref. [81].

Moreover, α-decay spectroscopy studies of ^{192}At were carried out by Andreyev *et al.* at the velocity filter SHIP. In this study, the observed α-decay pattern of ^{192}At and differences in the energies of the α-decay peaks was used to tentatively assign the low spin isomer in ^{188}Bi as the ground state [82].

The predicted yield of hs isomer and ls ground states were 320 ions/s and 60 ions/s, respectively. The HFS of both states was measured using Si1 and Si2 at the implantation position. Fig. 7.14(a) and Fig. 7.14(b) show the α-decay spectra measured during laser scans of ^{188}Bi taken in 2016 (HRS) and 2017 (GPS), respectively. Along with the Bi isotopes,

multiple Rn isotopes are also produced. This Rn gas can slowly diffuse through the ion source and the beamline and into the WM decay station. The GPS has a shorter beamline from the target to the WM than the HRS. This is reflected in these α-decay spectra, with the GPS spectra showing α-decay peaks from $^{201-203,205,206}$Rn and no Rn peaks observed in the HRS spectrum.

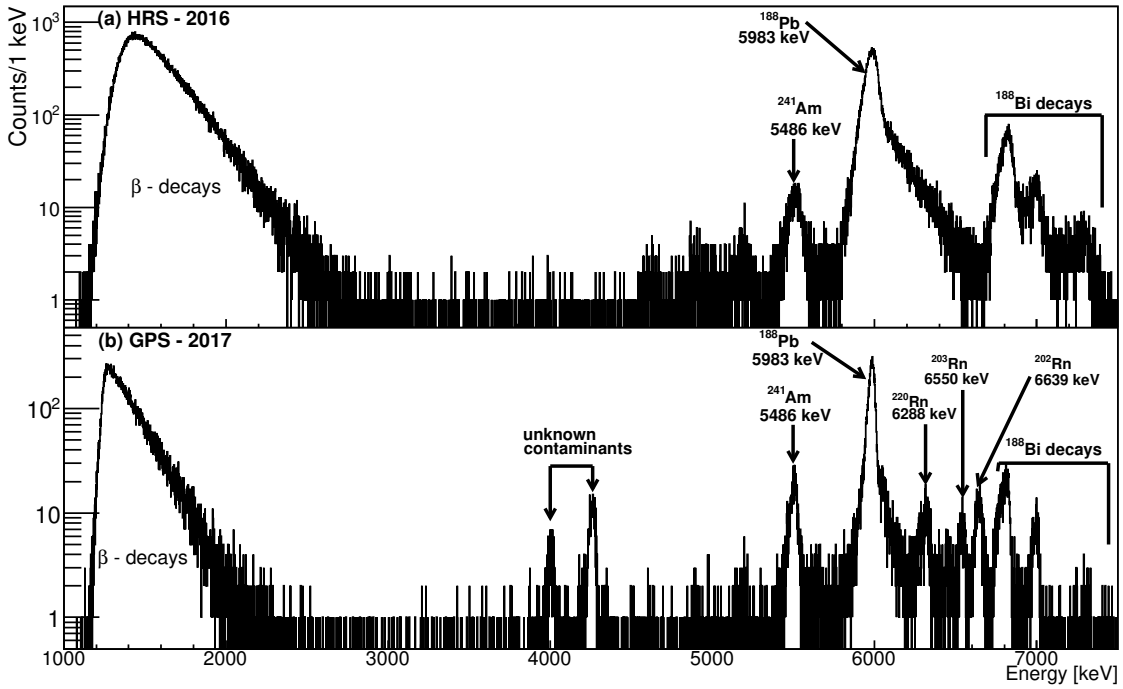

Figure 7.14: A comparison of α-decay spectra measured in (a) 2016 (scan 4) and (b) 2017. The large high energy tails seen on each α-decay peak in 2016 were a consequence of alpha-electron summing from the high level of low energy β decays.

Fig. 7.15 is an zoomed-in part of Fig. 7.14, showing only the region of ^{188}Bi α decays. The HFS spectrum for the hs state was produced by applying energy gates of 6780-6840 keV and energy gates of 7200-7400keV. For the $I^{\pi} = 1^{+}$ ground state, the HFS spectrum was produced by applying energy gates of 6960-7020 keV. In 2016 (HRS), scans 4 and 5 were carried out towards the end of the run. A consequence of this was a large amount of low energy β decays from surface ionised ^{188}Tl and isotopes produced in previous measurements, which is evident in Fig. 7.14(a), producing a significant amount of alpha-electron summing, producing high energy tails. This resulted in larger Full Width at Half Maximum (FWHM) for each observed α-decay peak. The measured FWHM from the fits are shown in the top right corner of both spectra in Fig. 7.15.

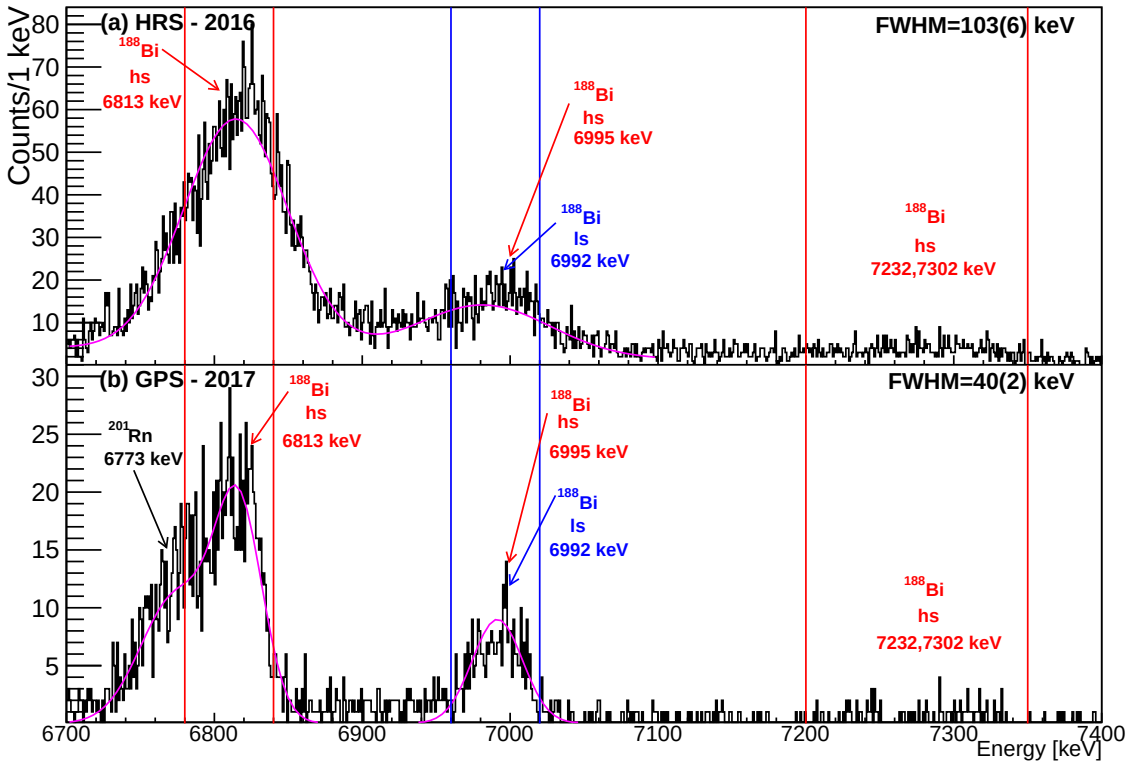

Figure 7.15: A comparison of the ^{188}Bi α-decay spectra from laser scans measured in (a) 2016 and (b) 2017. The large high energy tails present in 2016 resulted in a large number of counts from the 10^- isomer being present in the HFS spectra of the 1^+ ground state. The pink lines show Gaussian with exponential tail fits applied to the peaks to extract the FWHM for each scan.

These high energy tails in scans 4 and 5 meant that the 6813 keV 10^- α-decay peak and 6992 keV 1^+ α-decay peak were not well resolved. The ratio of number of α-decay events between the hs isomer and ground state in all laser scans of ^{188}Bi was determined as 3.74±0.35. This is largely due to the difference in half lives of 265(10)ms and 60(3)ms for the hs isomer and ground state, respectively. The time taken for the Bi atoms to effuse out of the target matrix and into the hot cavity results in more decay loss for the ground state before reaching the Windmill Decay Station. In contrast, the α-decay spectroscopy study of ^{188}Bi by Andreyev *et al.* in 2003 at the velocity filter SHIP [81], resulted in an even production of the hs isomer and ground state from the complete fusion evaporation reaction. At SHIP, products recoil out of thin targets, and so nuclei produced from the reaction come out the target and are implanted in the silicon detector in times of the order of μs. The α-decay spectrum measured in this study is shown in Fig. 7.16.

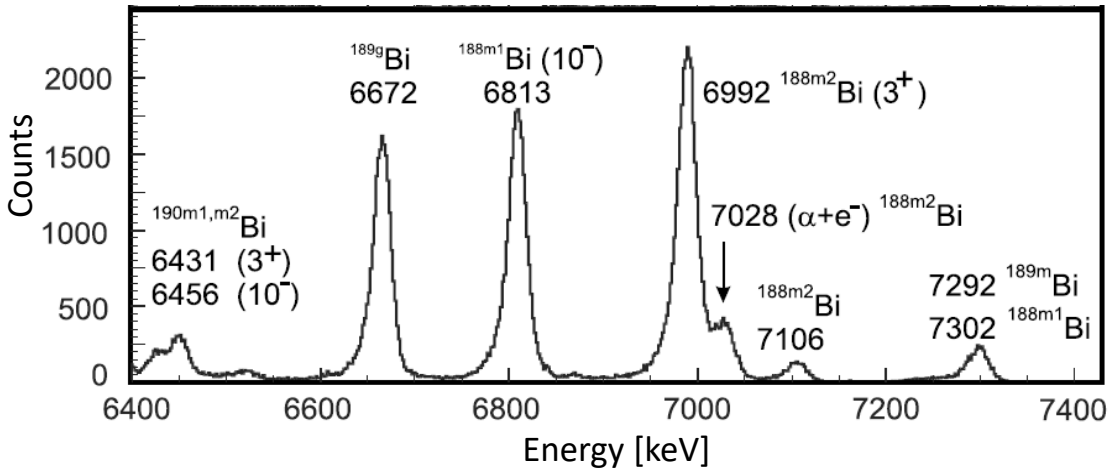

Figure 7.16: α-decay spectrum measured during the α-decay spectroscopy study of ^{188}Bi at the velocity filter SHIP by Andreyev *et al.* in 2003 [81]. Figure adapted from [81].

Figs. 7.17a,b show the HFS spectra extracted for hs isomer and ground states in ^{188}Bi, respectively, during a laser scan in 2016. The high energy tail in the 6813 keV 10^- α decay (shown in Fig. 7.15(a)) caused an increase in counts in the leftmost and middle hyperfine structure peaks of the $I^\pi = 1^+$ HFS spectra. Thus, the additional experimental run was carried out in 2017 in order to produce the correct HFS spectra for the ground state.

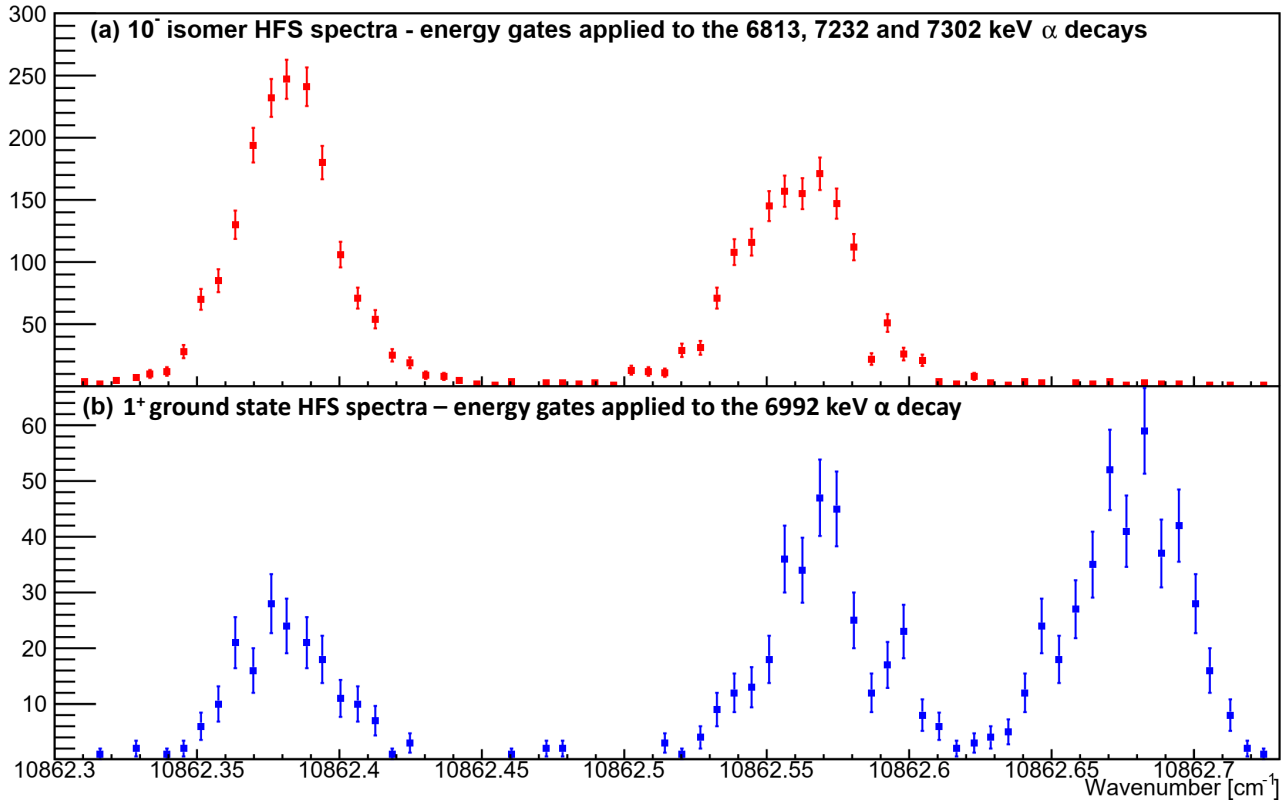

Figure 7.17: Extracted HFS as a function of laser wavenumber for a laser scan of (a) $I^{\pi} = 10^{-}$ isomer state and (b) $I^{\pi} = 1^{+}$ ground state of ^{188}Bi, taken in 2016.

In 2017 (GPS), the low-energy background was considerably lower and so the high energy tails were not present, as shown in Fig. 7.14b. As a result, both the 6813 keV 10^{-} α-decay peak and 6992 keV 1^{+} α decay were better resolved than in the 2016 (HRS) run, shown in Fig. 7.15a. Figs. 7.18a,b shows the HFS spectra extracted for 10^{-} isomer state and 1^{+} ground state in ^{188}Bi, respectively, during a laser scan in 2017 (GPS). For the HFS spectra of the 1^{+} ground state, it is clear that the intensity of the leftmost hyperfine structure is significantly reduced, along with a reduction in intensity of the central peak, in the 2017 laser scan, in comparison to the scan taken in 2016.

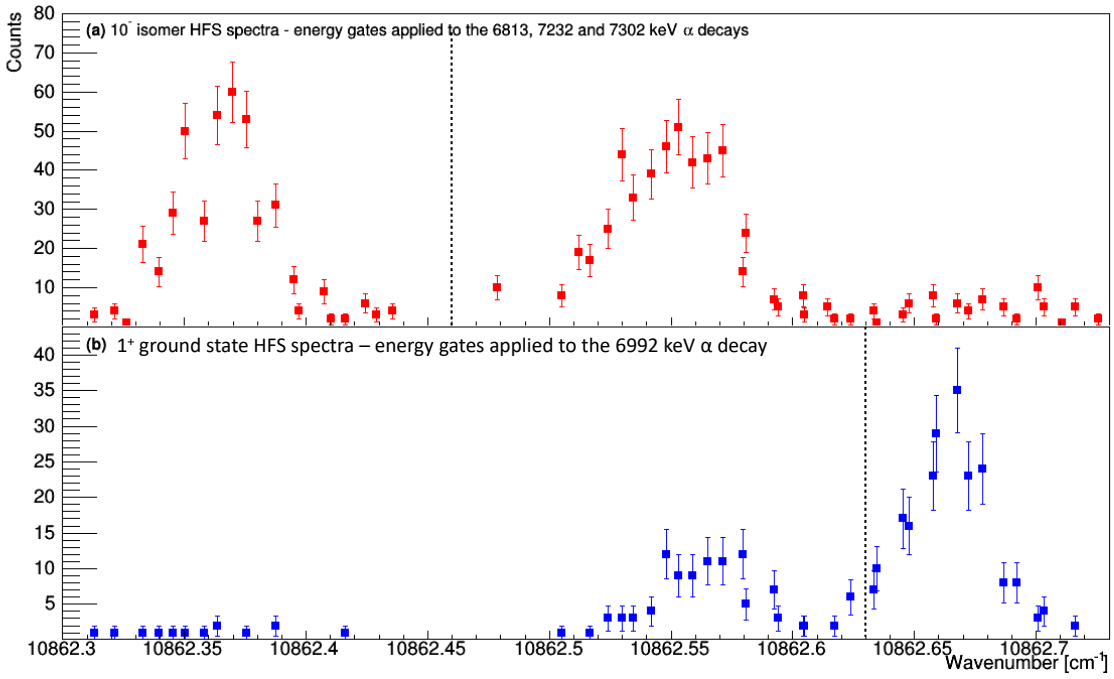

Figure 7.18: Extracted HFS as a function of laser wavenumber for a laser scan of ^{188}Bi (a) 10^- isomer state and (b) 1^+ ground state taken in 2017. The dashed black line shows the extracted centroid from fits applied to each spectra.

Separation of isomers

In order to suppress the 10^- isomer counts from the 1^+ ground state HFS spectra seen in the 2016 experimental run, timing gates were applied after the arrival of each proton pulse. Fig. 7.19 shows the distribution of α-decay events after every proton pulse in laser scan 4 for both the 10^- (red) isomer and 1^+ (blue) ground state. The difference in these time distributions arises due to the differing half lives: 265(10) ms for the 10^- isomer state and 60(3) ms for the 1^+ ground state [81]. Therefore, timing conditions applied after the arrival of each proton pulse was used to suppress the longer living 10^- isomer state, with timing gates of 200, 300 and 400 ms applied after every proton pulse. Fig. 7.20 shows the change in the 1^+ HFS spectra with these different timing conditions. To add to this, the 6992 keV 1^+ α decay has almost the same energy as the 6995(15) keV 10^- α decay, as shown in the decay scheme in Fig. 7.13, but has a much lower intensity.

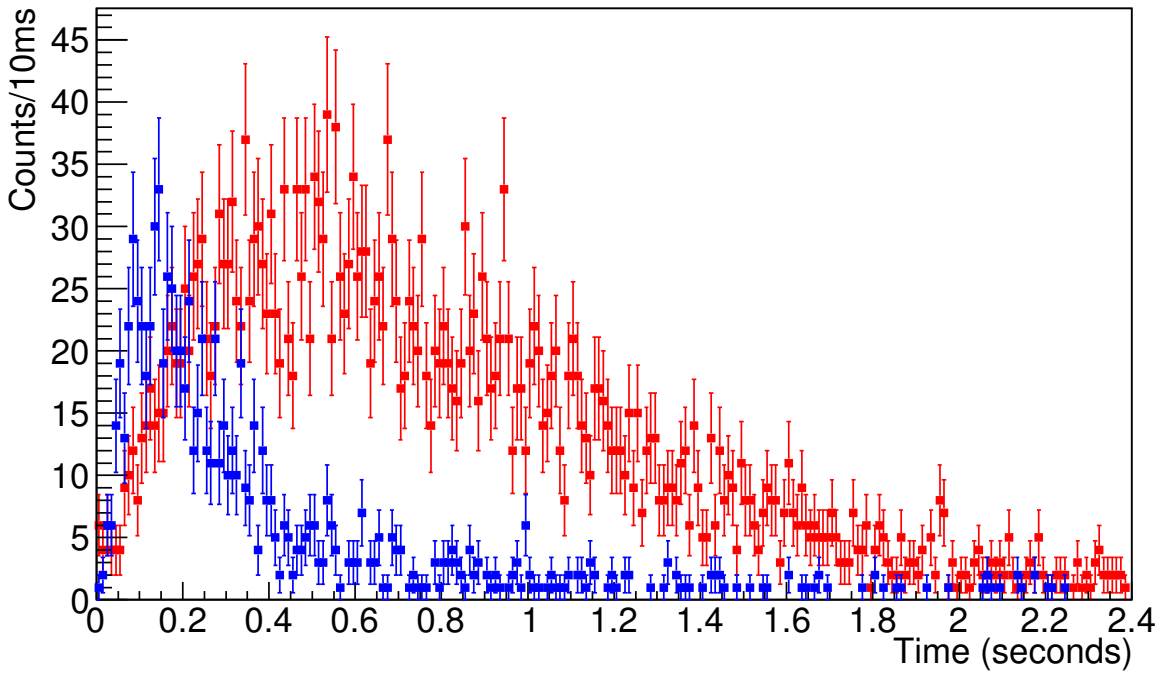

Figure 7.19: The extracted decay curves for the hs isomer (red) and ls ground (blue) states in ^{188}Bi. Energy gates were applied to α-decay peaks measured at the implantation position using Si1 and Si2. The maximum time of 2.4 seconds corresponds to the spacing between proton pulses. Based on this spectra, appropriate time gates could then be applied to each proton pulse in order to produce the cleaner ls HFS spectra.

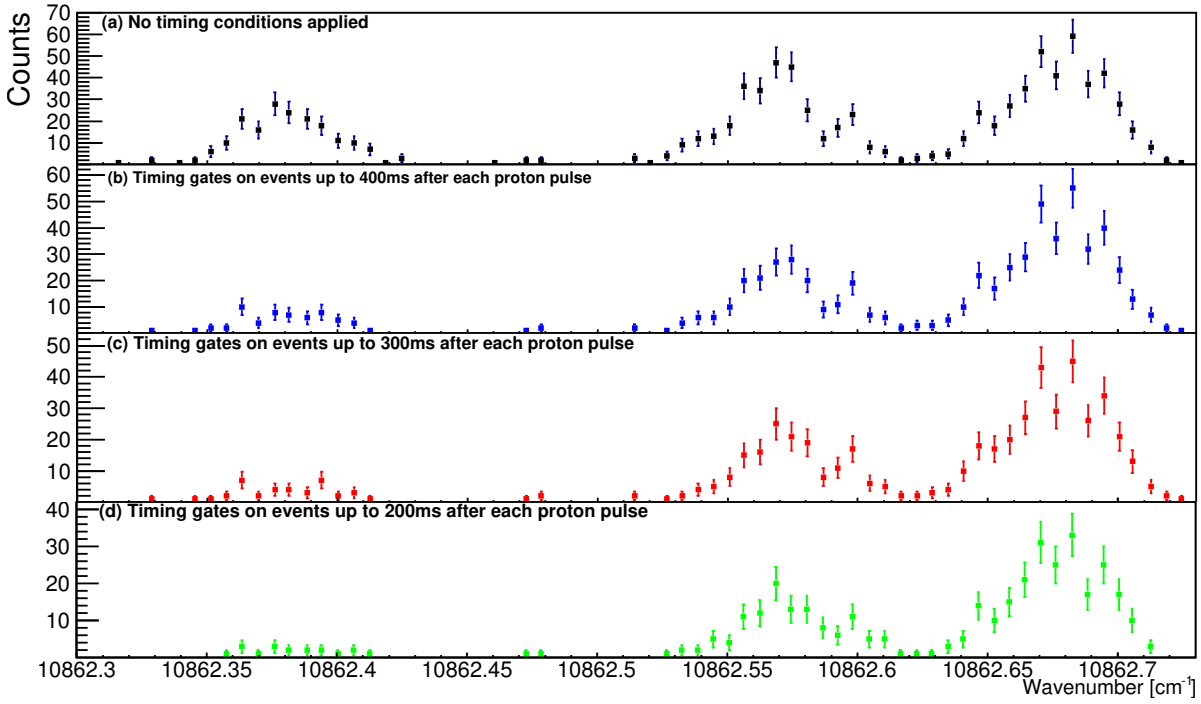

Figure 7.20: Extracted HFS as a function of laser wavenumber for a scan in 2016 of the 1^+ ground state. Timing gates were applied after each proton pulse impact to suppress counts arising from the hs isomer.

To this end, applying these timing gates the HFS spectra of the ground state have only two peaks, shifted from the hs HFS structures (shown in Fig. 7.18). The apparent presence of a peak at 10862.37 cm^{-1} was only due to contamination from the hs isomer state.

7.7 ^{187}Bi

The α-decay scheme of ^{187}Bi is shown in Fig. 7.21. Data were taken from Ref. [83]. The $9/2^-$ ground state decays by three branches, with the $1/2^+$ isomer state decaying by one branch.

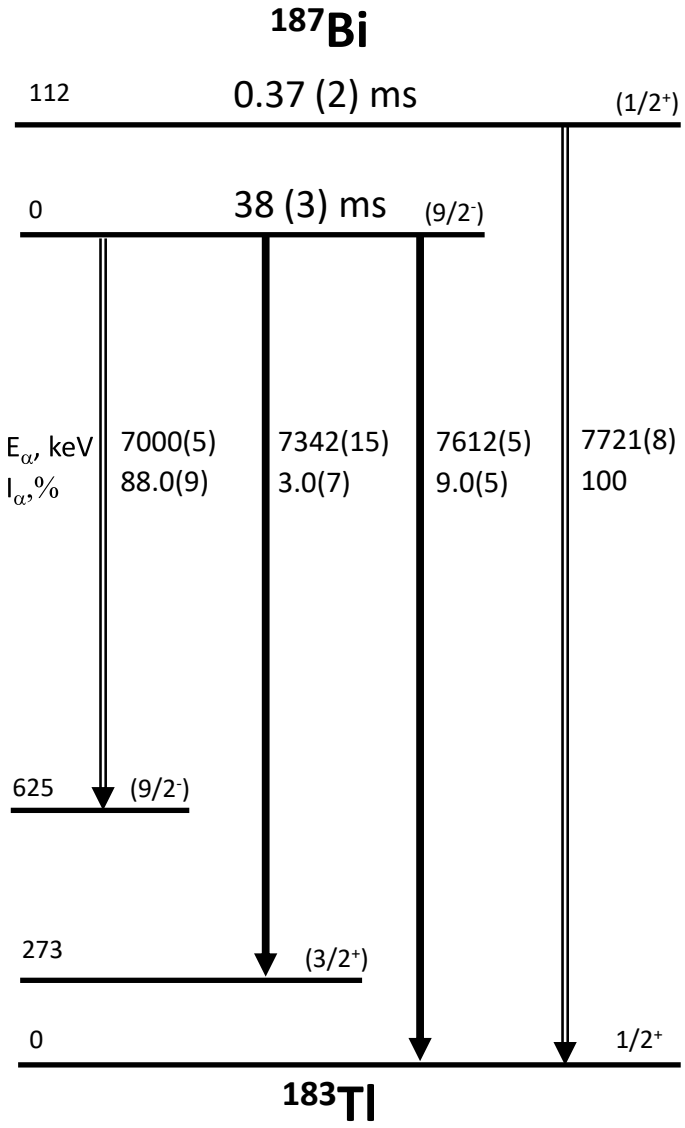

Figure 7.21: α-decay scheme for ^{187}Bi. Shown are the α-decay energies (E_α) and relative intensities (I_α) of each decay. These values were taken from Refs. [83].

Due to the low expected yield of 1.5 ions/s and the short half life of 38(3) ms [83], measurements of the HFS of $9/2^-$ state in ^{187}Bi was attained using 3 laser scans at 6 supercycles per laserstep. Fig. 7.22 shows the α-decay spectra produced from Si1 and Si2 during scan 2.

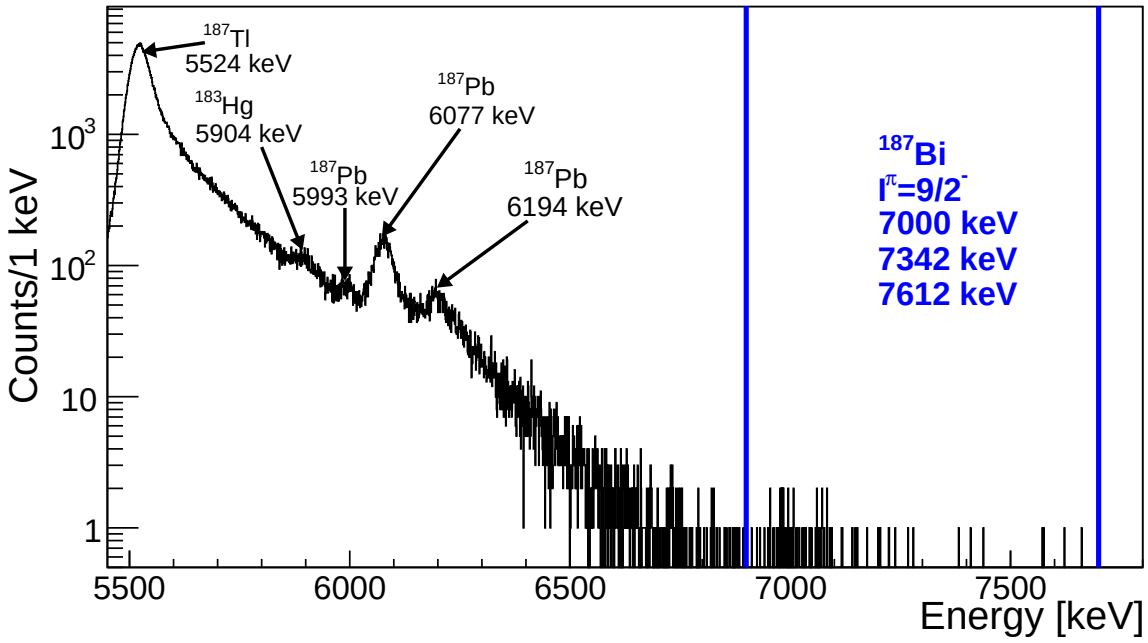

Figure 7.22: α-decay spectrum from laser scan 2 of ^{187}Bi measured at the implantation position using Si1 and Si2. The peaks are labelled with their decay energies in keV, as well as their corresponding parent isotope. The respective gating conditions used to produce the $9/2^-$ HFS spectra are indicated by the blue vertical lines.

During the scans of ^{187}Bi, there was a large amount of α-decaying isobaric contamination from the isotopes ^{187}Tl and ^{187}Pb, as can be seen in Fig. 7.22. However, these do not overlap with the energies of the α-decays from the $9/2^-$ ground state of ^{187}Bi. Due to the low statistics, a broader energy gate of 6900-7700 keV (shown by the blue lines in Fig. 7.22) was applied to the 7000, 7342 and 7612 keV α lines in order to produce as much statistics as possible in the HFS spectra. Fig. 7.23 shows the HFS spectra for the $9/2^-$ ground state.

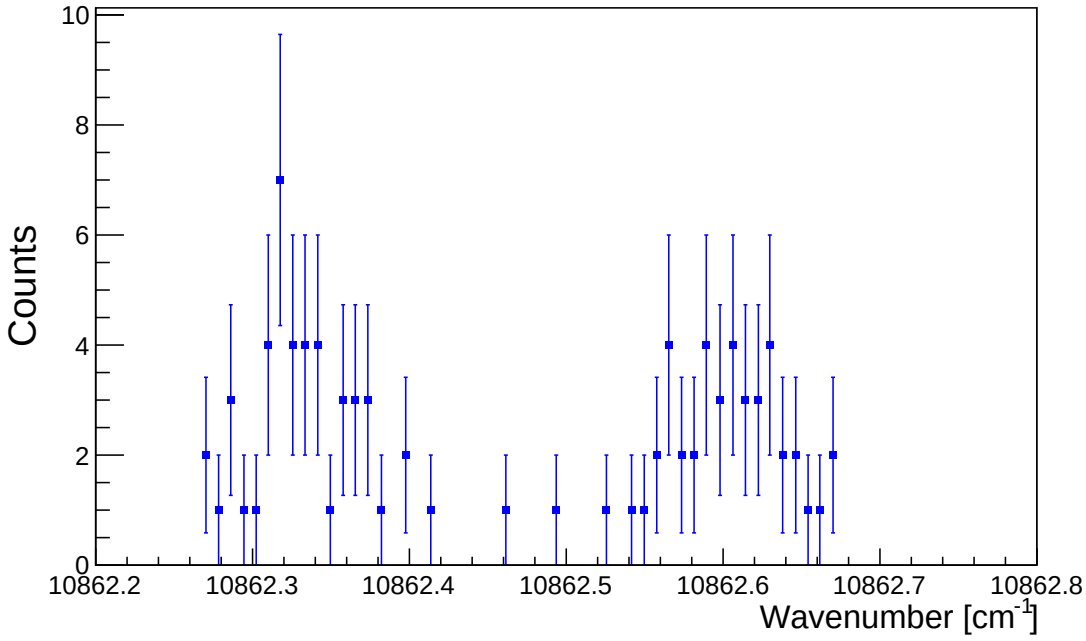

Figure 7.23: Extracted HFS as a function of laser wavenumber for scan 3 of ^{187}Bi. For the $9/2^-$ ground state, an energy gate of 6900-7700 keV was applied to the 7000, 7342 and 7612 keV α-decays measured using Si1 and Si2.

Chapter 8

Fitting of the HFS spectra

Upon extraction of the HFS spectra for each Bi isotope, one applies fits to each spectra, enabling extraction of the isotope shift (necessary to calculate the change in mean-square charge radius) and the electromagnetic hyperfine parameters a and b (allowing determination of both the magnetic dipole and electric quadrupole moment). This was performed by developing a fitting code in ROOT [84], from this point forward referred to as the HFS fit code. This code fitted the HFS spectra using Voigt profiles - a convolution of a Gaussian and Lorentzian distribution, which account for the Doppler broadening in the hot cavity and the laser linewidth, respectively. The intensity of each HFS component was determined using the intensities, given by Equation. 7.1.

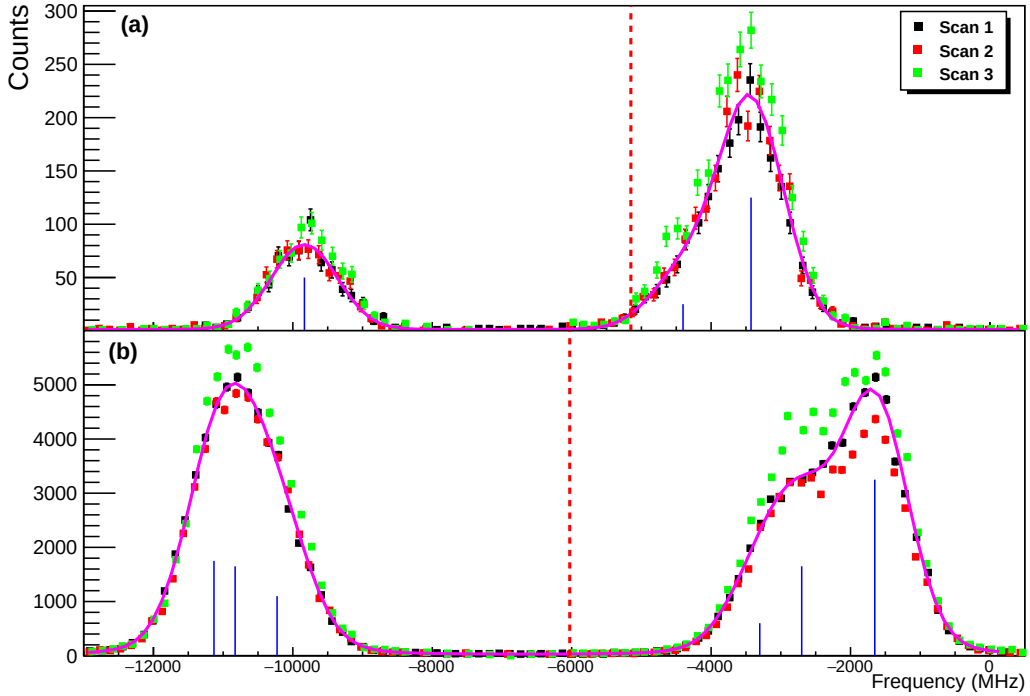

Figure 8.1: Fitting of HFS spectra for all three laser scans of ^{191}Bi I=9/2 (bottom panel) and I=1/2 (top panel) states using the HFS fit code. The fit (using average values of hyperfine constants a and b from all three scans) is shown by the pink lines, with the centre of gravity of the HFS spectra shown by the vertical dashed red lines. The vertical blue lines represent the centroid positions of each hyperfine transition, with their height proportional to their theoretical intensities.

Fig. 8.1 shows the fitting of ^{191}Bi, with fits applied to both the I=9/2 ground state (bottom panel) and I=1/2 isomer state (top panel). When extracting parameters from the HFS spectra, one must first convert from wavenumber to relative frequency. This was done by subtracting the fundamental wavenumber of the scanning laser (10862.72 cm^{-1}). In order to account for possible wavemeter drift, reference scans were also carried out for ^{209}Bi in order to determine the frequency reference point, which averaged as ν_{209}=1527(27) MHz. The HFS fit code does not take into account the effects of laser saturation and polarization during scanning. Modelling such effects is not trivial, however a simple model for saturation is implemented in the Python package SATLAS [85]. This package is specifically developed for analysis of laser spectroscopy data, accounting for laser saturation using the following equation:

$$I(s) \cong I_S \cdot exp\left(\frac{I_{racah} \cdot s}{I_s} - 1\right) \tag{8.1}$$

Table 8.1: Comparison of my and Seliverstov-Barzakh fitting routines for the a and b electromagnetic hyperfine parameters as well as the isomer shift, $\delta\nu$, between the I=9/2 and I=1/2 states in ^{191}Bi.

Fitting Procedure	$a(1/2)$ [MHz]	$a(9/2)$ [MHz]	$b(9/2)$ [MHz]	$\delta\nu$ [MHz]
HFS fit	-1460(10)	-410(3)	-1116(340)	2594(93)
Seliverstov-Barzakh	-1463(7)	-407(1)	-1023(65)	2629(49)

where $I_S = 2F_{lower} + 1$, $I_{racah} = \frac{I_{F_i F_f}}{I_{J_i J_f}}$ is the intensity ratio given by the equation 7.1 and s is the saturation parameter, varying from 0 (no laser saturation) to 1 (full laser saturation). This package was used to verify the values obtained from the HFS fit code. Parallel to this analysis, collaborators Anatoly Barzakh and Maxim Seliverstov from the St. Petersburg Nuclear Physics Institute, Gatchina, also applied fits to these HFS spectra. They utilise much more complex fitting procedures which implement all laser saturation and polarisation effects by solving rate equations. Table. 8.1 shows a comparison of the extracted values of the magnetic hyperfine parameters and isomer shift between the $I = 9/2$ ground and $I = 1/2$ isomeric states of ^{191}Bi from each fitting procedure. One can see that there is good agreement between both procedures for the magnetic hyperfine parameter a, and isomer shift. However, the values of the electric hyperfine parameter b have a large error. As a result, all the final values presented in this section were calculated from the values extracted using the Seliverstov-Barzakh procedure.

8.1 Changes in charge radii and deformation of the Bi nuclei

The isotope shifts relative to ^{209}Bi from fits applied to the HFS data are shown in Table. 8.2, along with the calculated values of the change in mean-squared charge radius, $\delta\langle r^2\rangle_{A,209}$, deduced using the Equation:

$$\delta\nu_{is}^{AA'} = \frac{A' - A}{AA'}M + F\delta\langle r^2\rangle^{A,A'} \tag{8.2}$$

discussed in Section 3. There are no atomic calculations for either the electronic F factor or the Specific Mass Shift (SMS). The electronic factor was determined using charge radii systematics for isotope pairs with N=124,126 and 122,124 for other elements in the Pb region, giving a value of F=24.8(17) GHz/fm^2 [31]. The SMS is typically negligible for an s→p transition, so one can assume $M = (1 \pm 2)M^{NMS}$, a relation used in adjacent isotopic

chains (see Refs. [44, 86, 87]).

The values of the root mean square quadrupole deformation parameter, $\langle\beta^2\rangle^{1/2}$, were calculated using the equation:

$$\langle r^2\rangle = \langle r^2\rangle_{DM}(1 + \frac{5}{4\pi}\langle\beta^2\rangle) \tag{8.3}$$

where $\langle r^2\rangle_{DM}$ is the charge radius deduced from the Droplet Model with zero deformation [88, 20]. Values of $\langle\beta^2\rangle$ where determined from the extracted values of $\delta\langle r^2\rangle$ and setting the mean-square deformation of ^{209}Bi equal to that of the neighbouring isotope, ^{208}Pb, such that, $\langle\beta^2\rangle^{1/2}_{^{209}Bi} = \langle\beta^2\rangle^{1/2}_{^{208}Pb} = 0.055(3)$ [89].

Table 8.2: Measured values of isotope shifts, $\delta\nu_{A,209}$ and the corresponding calculated values of changes in mean-square charge radii $\delta\langle r^2\rangle_{A,209}$, with the statistical errors given in round brackets and systematic errors given in curly brackets. The respective $\langle\beta^2\rangle^{1/2}$ values are also given, with the values determined from the framework of the Droplet Model, using the Berdichevsky and Tondeur (BT) parameters [20].

A	N	I	$\delta\nu_{A,209}$ [MHz]	$\delta\langle r^2\rangle_{A,209}$ [fm^2]	$\langle\beta^2\rangle^{1/2}$ [BT]
187	104	9/2	-22993(250)	-0.916(74){64}	0.194(16)
188	105	1	-8368(160)	-0.326(29){23}	0.287(25)
		10	-23667(100)	-0.944(9){66}	0.174(12)
189	106	9/2	-20823(50)	-0.830(8){58}	0.186(13)
191	107	9/2	-19610(50)	-0.782(7){55}	0.167(12)
		1/2	-16979(50)	-0.676(7){47}	0.192(14)

The extracted values of $\delta\langle r^2\rangle$ are plotted in Fig. 8.2 as a function of mass number. For comparison, the measurements from Barzakh *et al.* in 2016 [32, 31] and Pearson *et al.* in 2000 [58] are shown. The dashed black lines represent the DM predictions with constant deformation [20, 88]. The error bars represent the statistical errors only from the fitting of each HFS spectra.

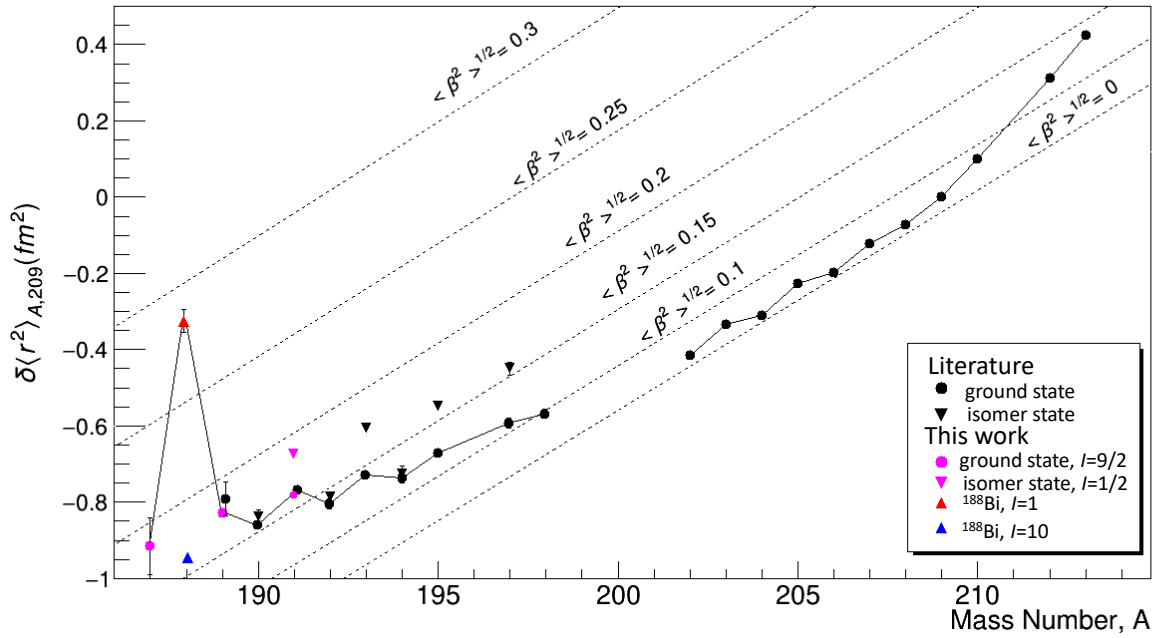

Figure 8.2: Change in mean-square charge radii for the Bi isotopic chain relative to ^{209}Bi, are shown as a function of mass number. For ground states, the data from this work (pink circles) and literature values [58, 32, 31] (black circles), are shown. For the isomeric states, this work (pink, downward triangles) and Gatchina [31] (black, downward triangles), are plotted. The values for the I^{π}=10^{-} and I^{π}=1^{+} isomers in ^{188}Bi are shown with blue and red triangles, respectively. To guide the eye, the black line connects each ground state measurement. The dashed black lines represent the DM predictions for the change in mean-square charge radius for fixed deformations [20, 88].

The data plotted in Fig. 8.2 shows the change in mean-square charge radii for neutron-deficient Bi nuclei. The charge radii of the 9/2^{-} ground states of ^{189,191}Bi were extracted with a lower error than the previous values from Gatchina [32]. This provides confidence that any systematic errors are accounted for. The light even-N Bi isotopes, ^{187,189,191}Bi, follow the same trend observed in the investigations carried out by Barzakh *et al.* in 2016 [32, 31], with a marked deviation from sphericity which can be interpreted as the onset of quadrupole deformation. At the same time, large shape staggering and shape coexistence is observed at ^{188}Bi, where the ground state has a larger rms deformation than the neighbouring odd-A Bi nuclei and the respective 10^{-} isomer of ^{188}Bi. While this is seen for several isotopes below A=198, it is significantly greater for ^{188}Bi.

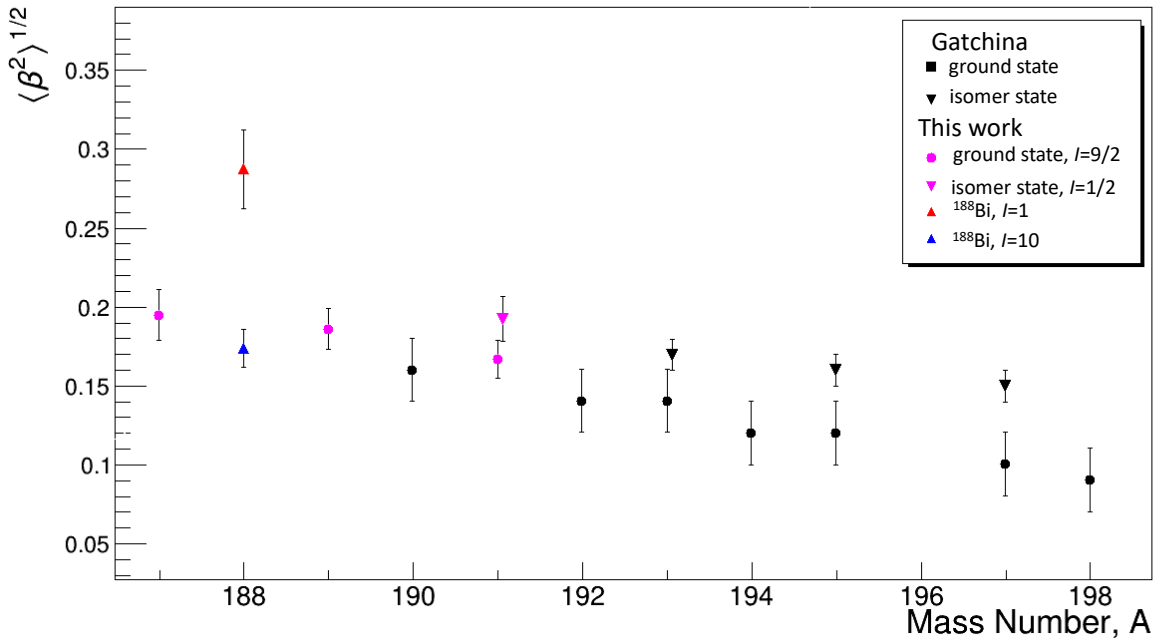

Figure 8.3: Ground (circles) and isomeric (triangles) state quadrupole deformation parameters as a function of neutron number for the light Bi isotopes from ISOLDE and Gatchina [32, 31]. These values were deduced by comparison of the measured $\delta\langle r^2\rangle$ with predictions using the DM [20, 88].

8.2 Comparison with neighbouring isotopic chains

Fig. 8.4 shows a comparison of the results of the Bi isotopic chain to the Tl and Pb chains. In order to remove the effect of odd-even staggering, whereby the odd-N isotopes have a smaller $\delta\langle r^2\rangle$ than their even-N neighbouring isotopes, even-N and odd-N isotopes were plotted separately. In order to remove the dependence on electronic factors, the values plotted were $\delta\langle r^2\rangle_{N,126}/\delta\langle r^2\rangle_{124,122}$. The data for the Pb, Po and Tl chains were obtained from Refs. [34, 29, 90, 91, 92, 93, 28].

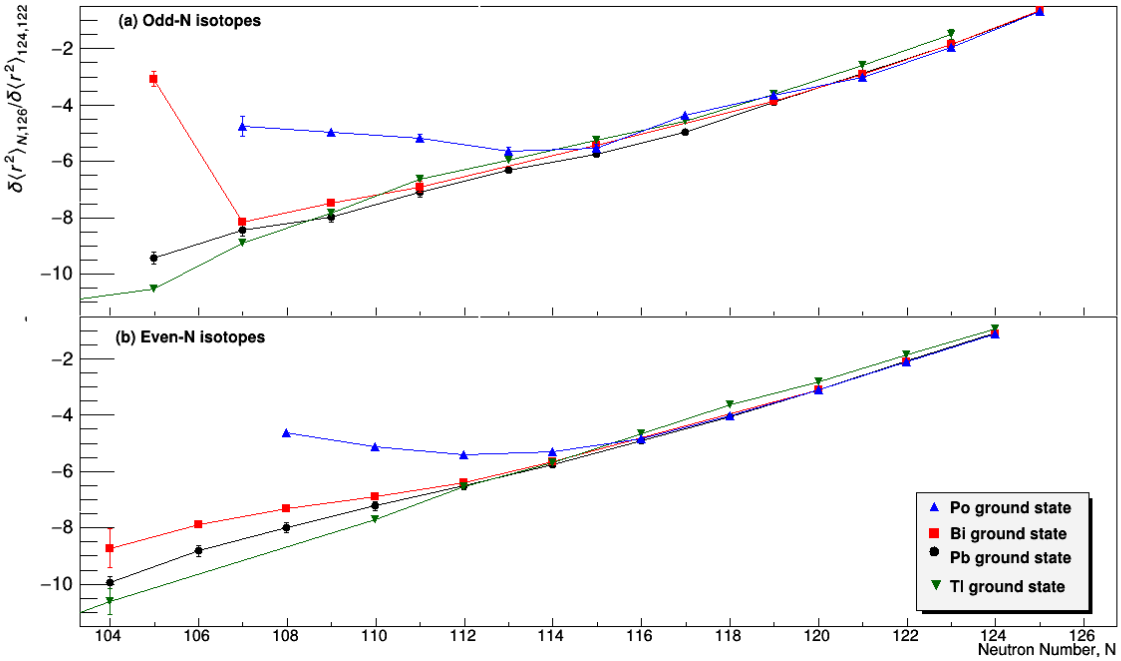

Figure 8.4: Comparison of the change in mean-square charge radii relative to the N=126 isotopes for the Po (blue), Pb (black), Bi (red) and Tl (green) isotopic chains.

Looking at Fig. 8.4, one can see that for N=112-126, the Bi isotopes follow the spherical Pb trend, which is the case for both odd and even-N nuclei. However, in the case of even-N Bi nuclei, there is a deviation from the Pb trend at N <112. This deviation is not as strong as what is observed in the Po isotopes, in which this phenomenon occurs in both odd and even N nuclei. In the odd-N isotopes, the large shape staggering effect observed at ^{188}Bi (N=105) was not observed in either the Tl or Pb isotopic chains.

8.3 Comparison with neutron-deficient Hg isotopes

Fig. 8.5 compares the changes in mean-squared charge radii for the neutron-deficient Hg and Bi isotopes. One of the most interesting features seen is that the shape staggering between ^{187,188,189}Bi resembles the staggering observed in the $^{181-185}$Hg [43], with both starting at the same neutron number (N=105). As well as this, the isomer shift relative to the staggering looks almost the same in both chains.

This may suggest that the same mechanism is involved in staggering in both isotopic

chains. In Section 4.2, the MCSM calculations were discussed which reproduced the large shape staggering effect seen in the Hg isotopes. These calculations highlighted the importance of a higher occupancy of two specific orbitals: the neutron $\nu 1i_{13/2}$ and proton $\pi 1h_{9/2}$ which induces the large shape staggering effect. These MCSM calculations will soon be extended to the lightest Bi isotopes $^{187-189}$Bi to further investigate the underlying mechanism behind this shape staggering effect.

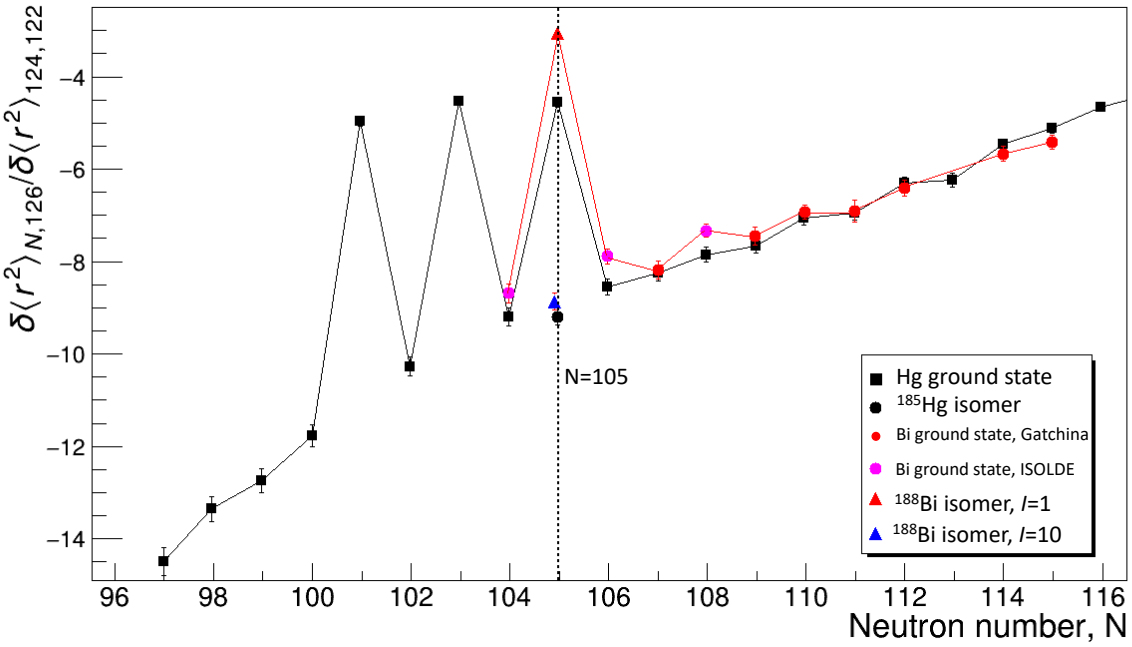

Figure 8.5: Comparison of the change in mean-square charge radii relative to the N=126 isotopes for the Hg (black) and Bi chain.

8.4 Magnetic dipole moments

The g-factor, g, of a nuclear state with spin I, is related to the magnetic dipole moment, μ, by the equation:

$$g = \frac{\mu}{I} \tag{8.4}$$

The magnetic dipole moment is determined primarily by the unpaired nucleons. Thus, for odd-A Bi nuclei, μ is defined by the unpaired proton. For odd-even nuclei with a single

unpaired nucleon, the Schmidt values [94, 95], μ_s, are determined using:

$$\mu_s = j\left(g_l \pm \frac{g_s - g_l}{2l+1}\right)\mu_N \tag{8.5}$$

where μ_N is the nuclear magneton, $j = l \pm 1/2$ is the spin of the single particle state, g_l is the orbital g-factor, which has a value of 0(1) for a free neutron (proton) and g_s is the spin g-factor which has a value of -3.83μ_N and 5.59μ_N for neutrons and protons, respectively.

Another factor to consider is that protons and neutrons are bound within a nucleus, thus not free particles. This is taken into account by quenching the g-factor using the effective g-factor such that $g_{eff} = \rho g_s$, where ρ is the renormalization factor which has values of 0.6-0.9 (calculations of μ_s for odd-A Bi nuclei in this work set ρ=0.6). This substitution allows the determination of the magnetic moment with this effect factored in, μ_q. In the following sections, the values of magnetic dipole moments extracted from the HFS spectra will be directly compared with both μ_s and μ_q.

In odd-odd nuclei, the magnetic moment of both the unpaired proton and neutron couple. One can use the additivity rule (single particle approximation) in order to deduce the total magnetic moment of the nucleus using the equation [19]:

$$\mu = \frac{I}{2}\left(g_\pi + g_\nu + (g_\pi - g_\nu)\frac{j_\pi(j_\pi+1) - j_\nu(j_\nu+1)}{I(I+1)}\right) \tag{8.6}$$

where j is the total angular momentum of the unpaired proton/neutron (subscripts π and ν denote the proton and neutron, respectively). One can use the g_π values of neighbouring odd-A Bi nuclei and g_ν values of adjacent odd-A Pb nuclei to determine the g-factors of odd-odd Bi nuclei. The values extracted from the experimental data can then be compared with these predicted values in order to determine the underlying configuration. The final experimental values of μ were evaluated using the formula:

$$\mu_A = \mu_{209}\frac{I_A}{I_{209}}\frac{a_A(^4S_{3/2})}{a_{209}(^4S_{3/2})} \tag{8.7}$$

where the subscript A denotes the atomic number of the isotope of interest. In this equation, the hyperfine structure anomaly for an atomic level without an unpaired s electron is ignored [96]. The values of μ_{209} and $a_{209}(^4S_{3/2})$ were taken from [97] as 4.0900(15)μ_N [98, 99] and -446.937(1) MHz [58], respectively. The extracted values of μ are presented in

Table 8.3 and are plotted as a function of neutron number in Fig. 8.6. The values of μ for ^{187g,188hs,189g,191g,191m}Bi follow the smooth systematics for heavier Bi isotopes.

Table 8.3: The magnetic hyperfine parameters, a, extracted from fitting of the HFS spectra and their corresponding magnetic moments for the Bi isotopes.

A	N	I	a [MHz]	μ [μ_N]
187	104	9/2	-397.7(25)	3.64(2)
188	105	1	-489(25)	0.99(5)
		10	-122.36(60)	2.49(1)
189	106	9/2	-400.83(20)	3.668(2)
191	107	9/2	-407(1)	3.72(1)
		1/2	-1463(7)	1.49(1)

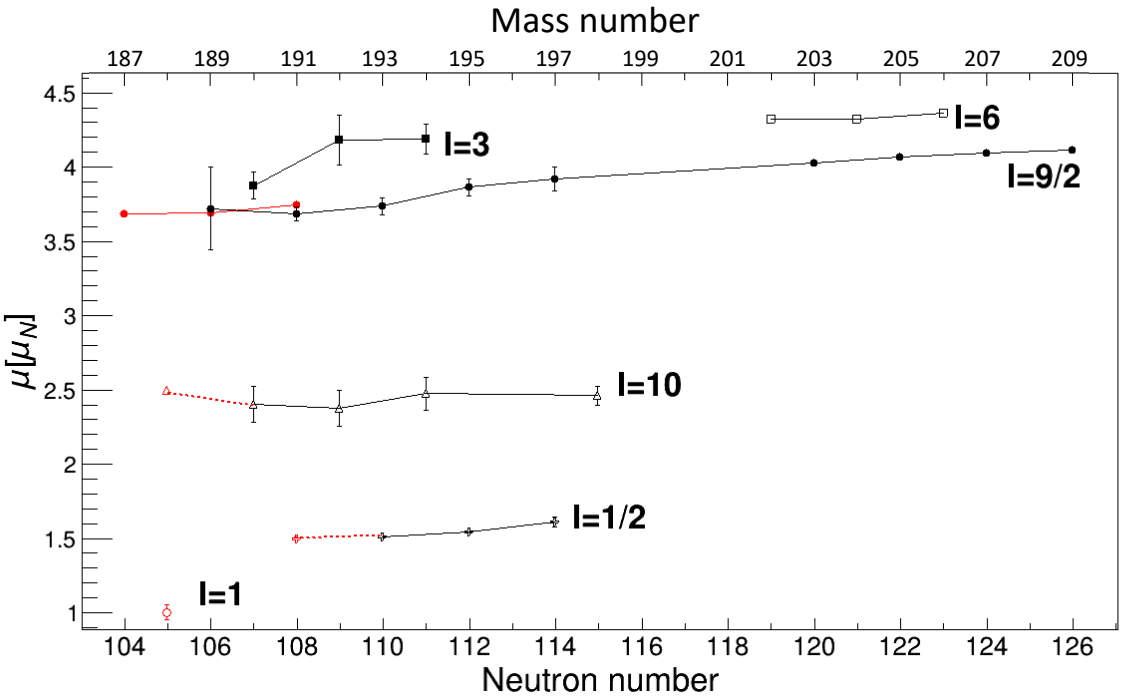

Figure 8.6: Magnetic moments of different states in neutron-deficient Bi nuclei as a function of neutron number, with the spin of each state labelled. Red data points indicate values from the work presented and black data points are taken from Refs. [56, 58, 32, 31]. The black and red lines represent a guide to the eye for the literature values and the data presented in this work, respectively.

8.5 Odd-A Bi nuclei

Fig. 8.7 shows a comparison between the values of μ for I=9/2 states in even-N Tl and Bi isotopes. The black dashed line represents the value of $\mu(^{209}Bi) = 4.0900(15)\mu_N$, used as a reference point. This is due to ^{209}Bi having a ground state configuration of a single $\pi 1h_{9/2}$ proton coupled to a ^{208}Pb core. Therefore, this value is used to directly compare other isotopes, with the same proton configuration. To add to this, the value of $\mu(^{209}Bi)$ differs significantly from both the calculated values of $\mu_q = 3.54\mu_N$ and $\mu_s = 2.62\mu_N$ (using ρ=0.6), determined for a single proton in the $1h_{9/2}$ orbital. Actually, for a nucleus with a structure of a single particle outside a doubly magic core, this is the largest difference in the whole nuclear chart.

The origin of this difference was explained by Arima and Horie, as a result of admixture of the 1p-1h spin-flip excitations to the ground state of ^{209}Bi [95, 100], with the leading role of $\nu 1i_{11/2} \bigotimes \nu 1i^{-1}_{13/2}$ and $\pi 1h_{9/2} \bigotimes \pi 1h^{-1}_{11/2}$ excitations. These excitations involve all protons and neutrons in the $\pi 1h_{11/2}$ and $\nu 1i_{13/2}$ orbitals, respectively. The high collectively of these excitations results in a large modification to the value of μ.

The data plotted in Fig. 8.7 shows that the magnetic moments of the I=9/2 states in ^{187,189,191}Bi are in good agreement with the trend of the Tl and At isotopes. All three isotopic chains start to deviate from $\mu(^{209}Bi)$ at N=114. A reduction in neutron number lowers the occupancy of the $\nu 1i_{13/2}$, thus reducing the number of neutrons involved in the core excitation. This results in the lowering of μ away from the reference value of $\mu(^{209}Bi)$, towards the values of both μ_s and μ_q.

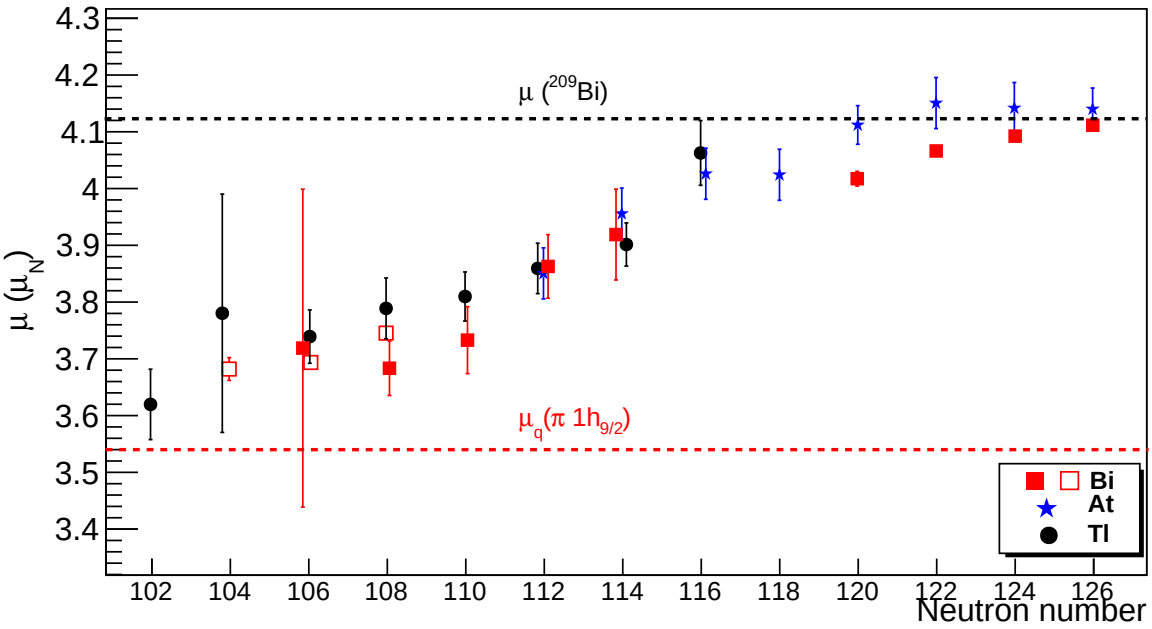

Figure 8.7: The values of μ for the $I = 9/2$ states in the Bi (red squares) [32, 31, 58], Tl (black circles) [34, 101] and At (blue stars) [35] isotopic chains. The hollow symbols show the results from this work, with solid symbols representing literature values. The dashed black horizontal line displays the magnetic moment of ^{209}Bi. The dashed red horizontal line shows the calculated value of μ_q for the I^{π}=9/2$^-$ state.

The magnetic moments for the I=1/2 states in neutron-deficient Bi nuclei are plotted as a function of neutron number in Fig. 8.8 along with the magnetic moments of the Tl isotopes. For the neutron-deficient Tl nuclei, this is the $\pi(0p-1h)$ spherical ground state, possessing a $\pi 3s^{-1}_{1/2}$ configuration. The magnetic moment for the I=1/2 state in ^{191}Bi is in good agreement with the Tl systematics, and is also close to the calculated value μ_q=1.677μ_N for the I=1/2 state. This indicates that this state is a $\pi 3s^{-1}_{1/2}$ intruder configuration, arising from the excitation of a proton across the Z=82 shell gap, forming a $\pi(1p-1h)$ excitation.

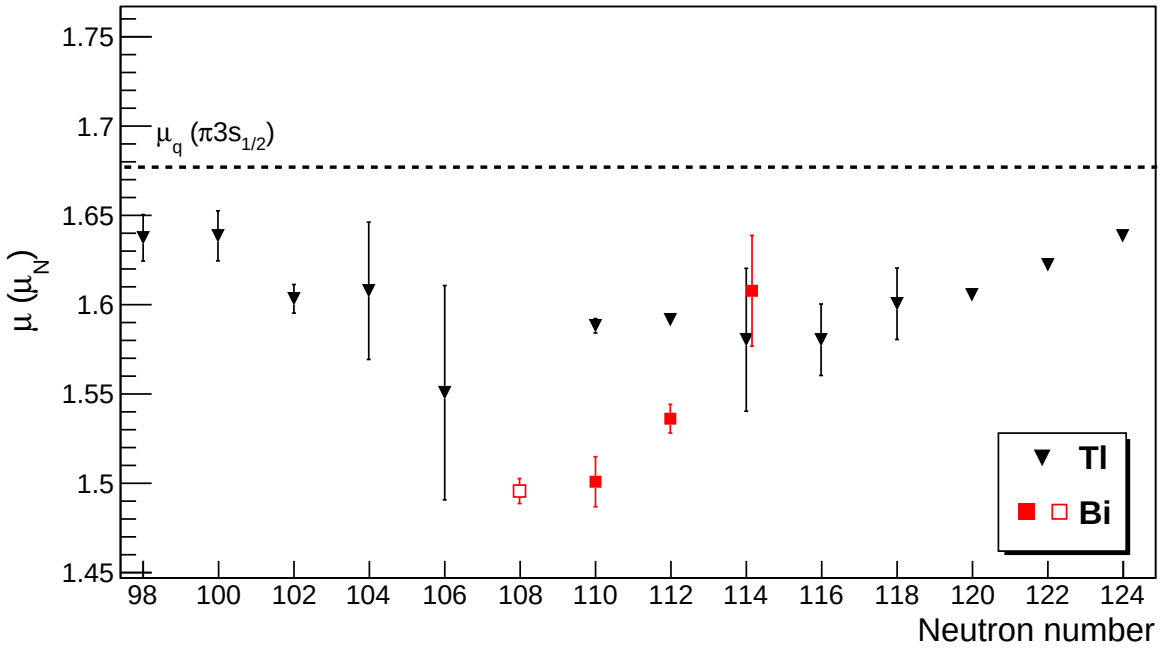

Figure 8.8: The values of μ for the $I = 1/2$ states in the Bi (red squares) [32, 31, 58] and Tl (black triangles) [34, 101] isotopic chains. The hollow symbols represent the results from this work, with solid symbols showing literature values. The dashed black horizontal line shows the calculated value of μ_q for the I^π=$1/2^+$ state.

8.6 ^{188}Bi

The $I^\pi = 10^-$ isomer state is well established in odd-odd Bi nuclei from N=125 all the way down to at N=105 [31]. Fig. 8.9 shows the extracted values of μ for the $I^\pi = 10^-$ isomer states in odd-odd Tl [34], Fr [102] and Bi isotopes. For the heavier odd-odd Bi nuclei (N=119-125) studied by Pearson *et al.* in 2000 [58], the magnetic moments were found to agree well with the calculated μ_{add} values (determined from Eqn. 8.6 using values of g_ν taken from the magnetic dipole moments of the adjacent odd-A Pb nuclei). However, the measurements by Barzakh *et al.* in 2017 show that this agreement falls off below N=111 (^{190,192,194}Bi). To restore agreement with μ_{add} values, g_ν values from the magnetic dipole moments of the $I^\pi = 13/2^+$ isomers in odd-A Po nuclei with comparable deformation were used. Details of values used for ^{190,192,194}Bi can be found in Ref. [31]. For ^{188}Bi ($\delta\langle\beta^2\rangle^{1/2}$=0.17(1)), the value used was $\mu = \mu(^{195}Po, I^\pi = 13/2^+) = -0.601\mu_N$. This modification of μ_{add} values restores good agreement for the lighter odd-odd Bi isotopes. This means that the structure of the $I^\pi = 10^-$ isomer state in ^{188}Bi could possibly be a mixture of both spherical and deformed

configurations, as in the Po nuclei [103]. This indicates that the 10^- isomer in ^{188}Bi has the same $\pi 1h_{9/2} \times \nu 1i_{13/2}$ configuration as in ^{190,192,194}Bi.

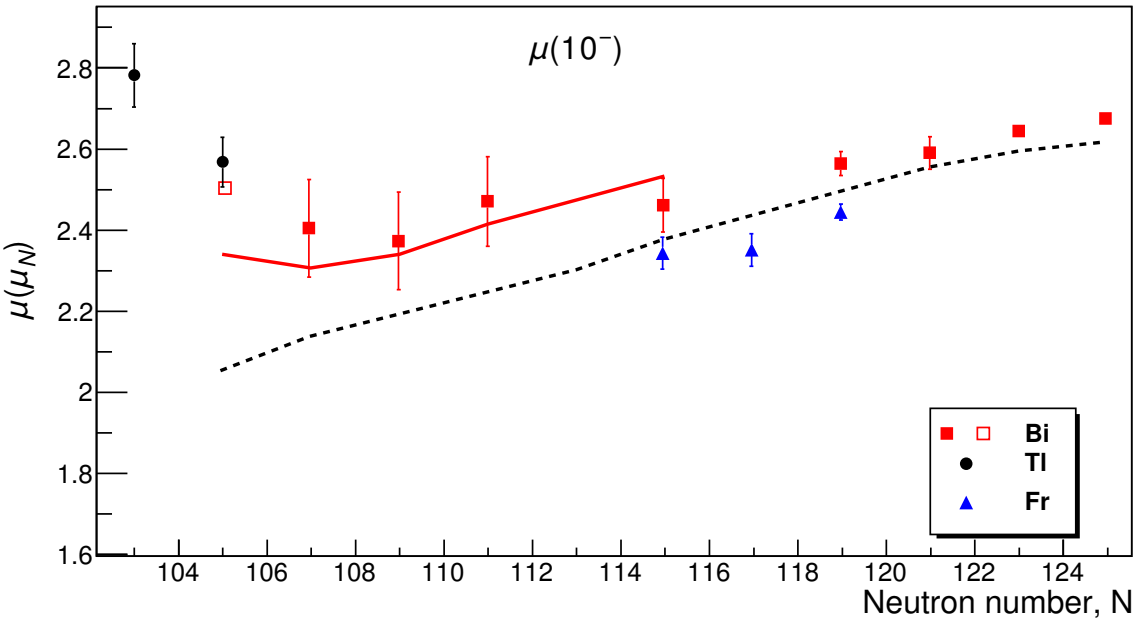

Figure 8.9: The values of μ for the $I = 10$ states in the Bi (red squares, open: this data, closed: literature [32, 58]), Fr [102] (blue triangles) and Tl [34] (black circles). The dashed line corresponds to μ_{add} calculations using μ_N values taken from the magnetic moments of adjacent odd-A Pb nuclei, with the solid red line utilising magnetic moments of Po nuclei with similar deformation.

For the low spin isomer of ^{188}Bi, the extracted value of the magnetic moment is $\mu = 1.00(5)\mu_N$, not in agreement with the magnetic moments of the I=3 states in the heavier odd-odd Bi nuclei ^{190,192,194}Bi ($\mu(^{190}\text{Bi})$=3.87(9)μ_N, $\mu(^{192}\text{Bi})$=4.18(17)μ_N and $\mu(^{194}\text{Bi})$=4.186(99)μ_N from Ref. [32]).

8.7 ^{188ls}Bi isomer spin assignment

As discussed in Section. 7.6, the interpretation of the low spin isomer of ^{188}Bi was changed from these data. This section of the thesis discusses the method used to determine the spin of this state. In order to accurately extract the isotope shift and the electromagnetic hyperfine parameters, exact knowledge of the nuclear spin is paramount. Extraction of the nuclear spin represents a particular challenge when utilising in-source laser spectroscopy. This is largely due to the Doppler broadening resulting in poor spectral resolution. Moreover, in

Table 8.4: Comparison of experimental α_{expt}, and theoretical, α_{theor} values for the peak area ratios of laser scans of the ^{188}Bi low spin isomer. Based on this, the spin was changed from the earlier suggestion of I=3 from Ref. [81], to I=1.

Nuclear Spin I:	1	2	3
α_{theor}	2.00	1.50	1.33
α_{expt}	2.01(9)		

the presence of saturation spin assignment cannot be performed using simple comparisons of goodness-of-fit for different spins.

In our experiment we did not resolve hyperfine components stemming from the different atomic ground-state sublevels. Thus, typically, hfs spectra consisted of two peaks each of them being the sum of the overlapping hyperfine components corresponding to the allowed transitions from the ground-state sublevels to one of the excited-state sublevels (either with total angular momentum F_{high} or F_{low}; see Fig. 7.2). In order to determine spin the "integration method" was used [104]. This method is based on comparison of areas under each resolved peak with theoretically predicted values (sum of the calculated intensities of each hyperfine component which formed that peak) for different spin assumptions. The ratio of areas under two peaks, formed by transitions to sublevels with F_{high} and F_{low} respectively, α_{expt}, is compared with calculated value α_{theor}:

$$\alpha_{theor} = \frac{\sum_F S_{F,F'=5}}{\sum_F S_{F,F'=4}} \tag{8.8}$$

Where S is the relative probability of a given hyperfine component, determined using Eqn. 7.1. It was shown that this ratio is weakly dependent on laser saturation and other distorting effects on the spectrum shape [104]. Table 8.4 shows a comparison of the α_{expt} value obtained as the weighted mean value from all the scans of the ^{188}Bi low spin isomer, with the calculated values of α_{theor} for different nuclear spins. One can clearly see good agreement of α_{expt} with α_{theor} for $I = 1$ and incompatibility of other spin assignments with experiment.

8.8 Electric quadrupole moments

The electric quadrupole moment, $Q_{s,A}$ of an isotope of atomic mass A was determined using the relation:

$$Q_{s,A} = \frac{b_A}{b_{209}} Q_{s,209} \tag{8.9}$$

where b_{209}=-305.067(2) MHz and $Q_{s,209}$=-0.420(8) b are the reference values from measurements of ^{209}Bi [105, 106]. One can relate the calculated value of Q_s to the quadrupole deformation parameter, β_Q using the relation:

$$Q_s = \frac{I \cdot (2I-1)}{(I+1)(2I+3)} \cdot \frac{3Z}{\sqrt{5\pi}} \cdot r_0^2 \cdot A^{2/3} \cdot \beta_Q \cdot (1 + \frac{1}{7}\sqrt{\frac{20}{\pi}}\beta_Q + ...) \tag{8.10}$$

where r_0=1.2 fm. It was important to compare the calculated values of β_Q with the values of β_{DM} extracted from the isotope shift data using Eqn. 8.3. Table. 8.5 shows the extracted values of Q_s along with β_Q and β_{DM} for the Bi isotopes.

Table 8.5: The electric hyperfine parameters, b, extracted from fitting of the HFS spectra and their corresponding electric quadrupole moments, Q_s, and quadrupole deformation parameter, β_Q, (see Eqn. 8.10) for the Bi isotopes. Values of $\beta_{DM} \equiv \langle\beta^2\rangle^{1/2}$ (see Eqn. 8.3) extracted from the isotope shift data are also shown for comparison.

A	N	I	b [MHz]	Q_s [b]	β_Q	β_{DM}
187	104	9/2	-912(400)	1.26(55)	-0.08(3)	0.194(16)
188	105	1	619(273)	0.85(38)	0.29(13)	0.287(25)
		10	-1218(300)	-1.68(41)	-0.08(2)	0.174(12)
189	106	9/2	-1160(14)	-1.60(4)	-0.098 (22)	0.186(13)
191	107	9/2	-1023(65)	-1.41(9)	-0.086(6)	0.192(14)

The ratio of Q_s, to the N=126 isotope of the same chain, $Q_{s,126}$ for $9/2^-$ states in even-N Fr, At and Bi isotopes and 8^+ states in even-N Po are shown in Fig. 8.10. Using this ratio removes dependence on the electric-field gradient calibration. Literature values for Bi isotopes were taken from [32, 31, 58], Po data taken from [107], At data taken from [35] and Fr data taken from [39, 40, 41, 42]. This investigation extends the Q_s data for $I = 9/2$ states in Bi down to N=104, with measurements for ^{187,189,191}Bi. Looking at Fig. 8.10 one can see that in the region N=120-126, the Bi isotopes follow the same linear trend as the other isotopic chains.

This linear increase in Q_s for states with $\pi h^n_{9/2}$ configurations with increasing number

of neutron holes in the N=126 shell has been observed in all isotopes up to the Ra isotopic chain (Z=88). The high resolution measurements of the Fr isotopes using the Collinear Resonance Ionisation Spectroscopy (CRIS) at ISOLDE, produced more precise values of Q_s therefore these measurements allow further testing of this phenomenon in the lead region. It should be noted that the error bars for the Fr isotopes in Fig. 8.10 include the error from the value of the reference isotope, $Q_s(^{213}\text{Fr})$=-0.14(2) b, taken from [108]. This is a much larger percentage error than from the Bi reference isotope $Q_s(^{209}\text{Bi})$=-0.420(8) b [106] although the Fr studies produced by CRIS experiments determined values of the electric hyperfine constant, b, with errors of under 10% [42]. For the neutron-deficient Bi nuclei, a deviation from the linear trend occurs at ^{193}Bi (N=110). The dashed line represents a quadratic fit applied to the Bi data in order to show this deviation. As discussed in Section 8.1 the I=9/2 ground state of even-N Bi nuclei shows a departure from the spherical trend of the Pb and Tl isotopic chains at N=110 (as shown in Fig. 8.4). However, there are no data for ^{199,201}Bi and the significantly large errors prevent one being able to draw conclusions on the nature of this deformation. Much greater spectral resolution is essential in order to more accurately determine the values of Q_s. Furthermore, all of the values of β_Q were smaller than the values of β_{DM} calculated from the IS data. β_{DM} should be larger than β_Q as it includes the dynamic deformation (zero-point vibration).

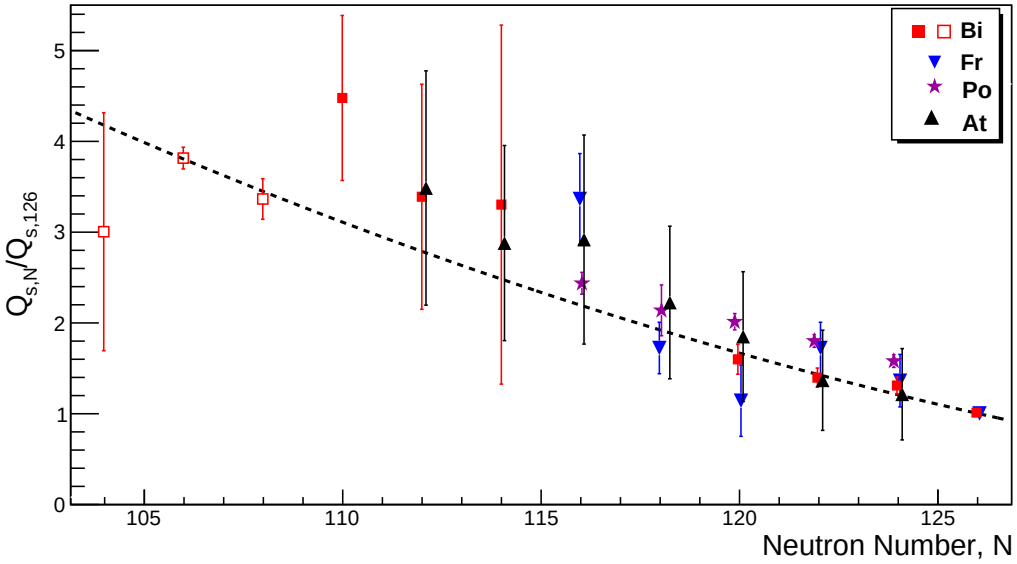

Figure 8.10: The ratio of quadrupole moments below N=126 to the quadrupole moment of a reference nuclide with N=126 for the $I = 9/2$ states in even-N Fr [39, 40, 41, 42] (blue triangles), At [35] (black triangles) and Bi nuclei (solid red squares [32, 31, 58], hollow red squares: this work). $I = 8$ states in even-N Po nuclei are also shown [107] (purple stars). The dashed line represents a quadratic fit to the Bi values, as a guide to the eye.

For ^{188}Bi, values of Q_s for both the $I^\pi = 1^+$ ground and $I^\pi = 10^-$ isomeric state, along with their corresponding values of β_Q are shown in Table. 8.5. One can clearly see that the value of β_Q for the $I^\pi = 10^-$ isomer is smaller than β_{DM}, extracted from the IS data. However, there is good agreement between β_Q and β_{DM} for the $I^\pi = 1^+$ ground state. At strong deformation, vibrations become small and the value of β_{DM} is much closer to the β_Q. This good agreement therefore further reinforces the interpretation that the $I^\pi = 1^+$ ground state is strongly deformed. The change in sign between the values of Q_s in these two states in ^{188}Bi indicates a possible change in nuclear shape from weakly oblate in both the $I^\pi = 10^-$ state, as well as in the ground states of the even-N neighbouring isotopes, ^{187,189}Bi, to strongly prolate in the $I^\pi = 1^+$ ground state.

Chapter 9

Conclusion

This thesis presents the studies of $^{187-189,191}$Bi from the IS608 experimental campaign at ISOLDE, CERN. Their respective isotope shifts, mean-square charge radius and electromagnetic moments were extracted. The results indicate that for the odd-A Bi nuclei, a marked deviation from the spherical trend of the Pb and Tl isotopic chains was observed in the I^{π}=$9/2^{-}$ ground states, interpreted as the onset of quadrupole deformation as the N=104 midshell is approached. A clear case of shape coexistence was observed in ^{191}Bi with a large difference in the charge radius of the I^{π}=$9/2^{-}$ ground and I^{π}=$1/2^{+}$ isomeric states of this isotope.

Analysis of the magnetic moments of $I = 9/2$ states in odd-A Bi nuclei revealed their predominant single particle nature, owing to a $\pi 1h_{9/2}$ configuration. The $I = 1/2$ isomer state in ^{191}Bi has a magnetic moment similar to the $I = 1/2$ states in the heavier Bi nuclei and the Tl isotopic chain. This indicates that this state in the even-N Bi isotopes has a $\pi 3s^{-1}_{1/2}$ intruder configuration. Values of Q_s were calculated for the $I^{\pi} = 9/2^{-}$ ground states of ^{187,189,191}Bi. These data revealed a linear increase in Q_s with increasing number of neutron holes in the N=126 shell. However, more precise measurements are necessary in order to further test the Q_s systematics for the most neutron-deficient Bi nuclei.

The magnetic moments of the ground and isomeric states of the odd-odd nucleus, ^{188}Bi were also measured. The $I = 10$ isomer has a magnetic moment consistent with the states of the same spin in heavier odd-odd Bi nuclei and At nuclei. μ_{add} calculations were compared with the extracted magnetic moments and the configuration $[\pi 1h_{9/2} \times \nu 1i_{13/2}]_{10^-}$ was assigned to

this state. As for the I^{π}=1^{+} state in ^{188}Bi, the integration method fixed the spin of this state.

Values of Q_s were also determined along with their corresponding values of β_Q. For the $I^{\pi} = 10^{-}$ isomer state the value of β_Q did not agree with the β_{DM} value extracted from the isotope shift data, which indicates the "soft" potential energy surface with large contribution of the zero-point vibration to $\delta\langle r^2\rangle$. However, for the $I^{\pi} = 1^{+}$ ground state there is good agreement between the values of β_Q and β_{DM}, which additionally support the strong prolate deformation. Comparison of extracted Q_s values indicated a change in shape from prolate in the ground state ($I^{\pi} = 1^{+}$) to presumably oblate in the isomer ($I^{\pi} = 10^{-}$).

The most interesting outcome in this investigation was the strong shape coexistence between the 1^{+} ground and 10^{-} isomer state in ^{188}Bi. The ground state has a value of β_{DM} much larger than both the 10^{-} isomer and the $9/2^{-}$ ground states of the neighbouring odd-A isotopes ^{187,189}Bi. Moreover, this state is also much more deformed than the $1/2^{+}$ intruder states in ^{191,193,195,197}Bi, indicating a significant difference in the underlying structure of the odd-odd and odd-A Bi nuclei. Furthermore, the shape staggering measured between the ground states of ^{187,188,189}Bi is very similar to the historically well known shape staggering phenomenon observed in $^{181-185}$Hg, with both starting at the same neutron number (N=105). This could suggest that the same mechanism is inducing this deformation.

9.1 Future work

In terms of the laser spectroscopy studies of the neutron deficient Bi nuclei, it would be interesting to determine whether or not the shape staggering effect between odd-A and odd-odd Bi nuclei persists in the same way as in the shape staggering observed in the Hg isotopic chain. This would at least require measurement of the HFS of ^{186}Bi. Due to low production of this isotope at ISOLDE, it was not possible to measure it so far.

However, the upgrade of the ISOLDE facility in 2020 may increase production of this isotope in the target enough to allow its measurement. This would certainly require extended run times for each laser scan. This poses a challenge in terms of the fluctuation in the number of protons as well as the stability of the lasers. Significant ion source development by

RILIS and the target group in the future may reduce the release times of reaction products from the target. These upgrades will make it possible to measure many more isotopes at ISOLDE.

Recent Monte Carlo Shell Model (MCSM) calculations were carried out on the Hg chain, reproducing the large shape staggering seen in the isotopes $^{181-185}$Hg. Good agreement was noted for both the charge radii and electromagnetic moments for the odd-N nuclei. The MCSM calculations are currently being extended to the Bi isotopes $^{187-191}$Bi to seek the underlying reasons of the shape staggering at ^{188}Bi and guide further experimental findings. Furthermore, in 2019 γ-ray spectroscopy studies were carried out on ^{188}Bi in order to observe the bands built on top of both states. Analysis is underway and the results may help pin down the configuration of both states.

For the Bi chain, the evaluated spectroscopic quadrupole moments have large uncertainties due to the low resolution of the in-source laser spectroscopy method. The main advantage of in-source laser spectroscopy is the high ionization efficiency which allows investigation of isotopes with production rates as low as 1 atom per second. However, due to the high temperature of the ion source, Doppler broadening typically dominates the spectral resolution, resulting in large errors on the extracted values of Q_s. Collinear laser spectroscopy is an alternative method which has a spectral resolution 100-1000 times greater than the in-source approach [109]. Recent developments of the Paul trap ISCOOL, a device which cools and bunches the ion beam before its sent to CRIS, has lowered the sensitivity down to 100 atoms per second under optimal conditions, although typically 10,000 atoms per second is necessary [110]. More recently, laser spectroscopy studies were carried out using CRIS at ISOLDE on the Fr isotopes, enabling extraction of the quadrupole moment with reduced errors [42]. With the current production yields at ISOLDE, it would be possible to use CRIS to measure the values of Q_s of the isotopes ^{189,191}Bi as well as remeasure the ground states of ^{193,195,197}Bi, previously determined by Barazkh *et al.* in 2016 [31]. These measurements will provide information on the evolution of the quadrupole deformation in odd-A Bi nuclei when approaching the N=104 midshell.

Bibliography

[1] K. Wimmer et al., Discovery of the shape coexisting 0^+ state in ^{32}Mg by a two neutron transfer reaction, *Phys. Rev. Lett.*, 105:252501, Dec 2010.

[2] P. Möller, A.J. Sierk, T. Ichikawa, and H. Sagawa, Nuclear ground-state masses and deformations: FRDM(2012), *Atomic Data and Nuclear Data Tables*, 109-110:1 – 204, 2016.

[3] H. Morinaga, Interpretation of Some of the Excited States of $4n$ Self-Conjugate Nuclei, *Phys. Rev.*, 101:254–258, Jan 1956.

[4] K. Heyde and J. Wood, Shape coexistence in atomic nuclei, *Reviews of Modern Physics*, 83:1467–1521, 11 2011.

[5] K Heyde and J L Wood, Nuclear shapes: from earliest ideas to multiple shape coexisting structures, *Physica Scripta*, 91(8):083008, jul 2016.

[6] P. Campbell, I.D. Moore, and M.R. Pearson, Laser spectroscopy for nuclear structure physics, *Progress in Particle and Nuclear Physics*, 86:127–180, 2016.

[7] C. F. v. Weizsäcker, Zur theorie der kernmassen, *Zeitschrift für Physik*, 96(7):431–458, Jul 1935.

[8] W. D Myers and W.J Swiatecki, Average nuclear properties, *Annals of Physics*, 55(3):395 – 505, 1969.

[9] K. S. Krane. *Introductory nuclear physics.* Wiley, 1988.

[10] Otto Haxel, J. Hans D. Jensen, and Hans E. Suess, On the "Magic Numbers" in Nuclear Structure, *Phys. Rev.*, 75:1766–1766, Jun 1949.

[11] J. Cubiss. PhD thesis University of York: In-source laser spectroscopy of At isotopes and decay studies of ^{178}Au, 2017.

[12] S. G. Nilsson, Binding states of individual nucleons in strongly deformed nuclei, *Kong. Dan. Vid. Sel. Mat. Fys. Med.*, 29N16:1–69, 1955.

[13] R.B. Firestone. *Table of Isotopes.* Wiley-Interscience, 1996.

[14] G. Gamow, Zur Quantentheorie des Atomkernes, *Zeitschrift für Physik*, 51(3):204–212, Mar 1928.

[15] B. Cheal and K.T. Flanagan, Progress in laser spectroscopy at radioactive ion beam facilities, *Journal of Physics G: Nuclear and Particle Physics*, 37(11):113101, Sept 2010.

[16] E Otten. Nuclear Radii and Moments of Unstable Isotopes, Jan 1989.

[17] W. H. King. *Isotope shifts in atomic spectra.* 1984.

[18] H. B. G. Casimir. On the interaction between Atomic Nuclei and Electrons, 1963.

[19] C. Ekström, G. Wannberg, and Y. S. Shishodia, Hyperfine structure and nuclear magnetic moments of some neutron-deficient thallium isotopes, *Hyperfine Interactions*, 1:437–458, June 1975.

[20] D. Berdichevsky and François Tondeur, Nuclear core densities, isotope shifts, and the parametrization of the droplet model, *Zeitschrift für Physik A*, 322:141–147, 02 1985.

[21] Kris Heyde, A shell-model description of intruder states and shape coexistence, *Nuclear Physics A*, 507(1):149 – 154, 1990.

[22] K. Heyde, C. De Coster, J. Ryckebusch, and M. Waroquier, Equivalence of the spherical and deformed shell-model approach to intruder states, *Physics Letters B*, 218(3):287 – 290, 1989.

[23] A. N. Andreyev et al., A triplet of differently shaped spin-zero states in the atomic nucleus ^{186Pb}, *Nature*, 405:430–433, 06 2000.

[24] J. Bonn, G. Huber, H. J. Kluge, L. Kugler, and E. W. Otten, Sudden change in the nuclear charge distribution of very light mercury isotopes, *Physics Letters B*, 38(5):308 – 311, 1972.

[25] N. Rud, D. Ward, H. R. Andrews, R. L. Graham, and J. S. Geiger, Lifetimes in the Ground-State Band of ^{184}Hg, *Phys. Rev. Lett.*, 31:1421–1423, Dec 1973.

[26] D. Proetel, R. M. Diamond, P. Kienle, J. R. Leigh, K. H. Maier, and F. S. Stephens, Evidence for Strongly Deformed Shapes in ^{186}Hg, *Phys. Rev. Lett.*, 31:896–898, Oct 1973.

[27] J. Bonn, G. Huber, H. J. Kluge, and E. W. Otten, Spins, moments and charge radii in the isotopic series $^{181-191}$Hg, *Zeitschrift für Physik A Atoms and Nuclei*, 276(3):203–217, Sep 1976.

[28] M.D. Seliverstov et al., Charge radii of odd-A $^{191-211}$Po isotopes, *Physics Letters B*, 719(4):362 – 366, 2013.

[29] István Angeli and Krassimira Marinova, Table of experimental nuclear ground state charge radii: An update, *Atomic Data and Nuclear Data Tables*, 99:69–95, 01 2013.

[30] M. Seliverstov et al., Electromagnetic moments of odd-A $^{193-203,211}$Po isotopes, *Physical Review C*, 03 2014.

[31] A. E. Barzakh, D. V. Fedorov, V. S. Ivanov, P. L. Molkanov, F. V. Moroz, S. Yu. Orlov, V. N. Panteleev, M. D. Seliverstov, and Yu. M. Volkov, Laser spectroscopy studies of intruder states in ^{193,195,197}Bi, *Phys. Rev. C*, 94:024334, Aug 2016.

[32] A. E. Barzakh, D. V. Fedorov, V. S. Ivanov, P. L. Molkanov, F. V. Moroz, S. Yu. Orlov, V. N. Panteleev, M. D. Seliverstov, and Yu. M. Volkov, Onset of deformation in neutron-deficient Bi isotopes studied by laser spectroscopy, *Phys. Rev. C*, 95:044324, Apr 2017.

[33] A. E. Barzakh, L. Kh. Batist, D. V. Fedorov, V. S. Ivanov, K. A. Mezilev, P. L. Molkanov, F. V. Moroz, S. Yu. Orlov, V. N. Panteleev, and Yu. M. Volkov, Changes in the mean-square charge radii and magnetic moments of neutron-deficient Tl isotopes, *Phys. Rev. C*, 88:024315, Aug 2013.

[34] A. E. Barzakh et al., Changes in mean-squared charge radii and magnetic moments of $^{179-184}$Tl measured by in-source laser spectroscopy, *Phys. Rev. C*, 95:014324, Jan 2017.

[35] J. G. Cubiss et al., Charge radii and electromagnetic moments of $^{195-211}$At, *Phys. Rev. C*, 97:054327, May 2018.

[36] H. De Witte et al., Nuclear Charge Radii of Neutron-Deficient Lead Isotopes Beyond $N = 104$ Midshell Investigated by In-Source Laser Spectroscopy, *Phys. Rev. Lett.*, 98:112502, Mar 2007.

[37] T. E. Cocolios et al., Early Onset of Ground State Deformation in Neutron Deficient Polonium Isotopes, *Phys. Rev. Lett.*, 106:052503, Feb 2011.

[38] D. A. Fink et al., In-Source Laser Spectroscopy with the Laser Ion Source and Trap: First Direct Study of the Ground-State Properties of ^{217,219}Po, *Phys. Rev. X*, 5:011018, Feb 2015.

[39] K. T. Flanagan et al., Collinear Resonance Ionization Spectroscopy of Neutron-Deficient Francium Isotopes, *Phys. Rev. Lett.*, 111:212501, Nov 2013.

[40] K. M. Lynch et al., Decay-Assisted Laser Spectroscopy of Neutron-Deficient Francium, *Phys. Rev. X*, 4:011055, Mar 2014.

[41] I. Budinčević et al., Laser spectroscopy of francium isotopes at the borders of the region of reflection asymmetry, *Phys. Rev. C*, 90:014317, Jul 2014.

[42] S. G. Wilkins et al., Quadrupole moment of ^{203}Fr, *Phys. Rev. C*, 96:034317, Sep 2017.

[43] B. Marsh et al., Characterization of the shape-staggering effect in mercury nuclei, *Nature Physics*, 14:1163–1167, 12 2018.

[44] G. Ulm, S. K. Bhattacherjee, P. Dabkiewicz, G. Huber, H.-J. Kluge, T. Kühl, H. Lochmann, E.-W. Otten, K. Wendt, S. A. Ahmad, W. Klempt, R. Neugart, and I. S. O. L. D. E. Collaboration, Isotope shift of ^{182}Hg and an update of nuclear moments and charge radii in the isotope range $^{181-206}$Hg, *Zeitschrift für Physik A Atomic Nuclei*, 325(3):247–259, Sep 1986.

[45] R Julin, K Helariutta, and M Muikku, Intruder states in very neutron-deficient Hg, Pb and Po nuclei, *Journal of Physics G: Nuclear and Particle Physics*, 27(7):109–139, June 2001.

[46] M. Scheck et al., Lifetimes of odd-spin yrast states in ^{182}Hg, *Phys. Rev. C*, 81:014310, Jan 2010.

[47] J. Wauters et al., Alpha decay of ^{186}Pb and ^{184}Hg: The influence of mixing of 0^+ states on α-decay transition probabilities, *Phys. Rev. C*, 50:2768–2773, Dec 1994.

[48] J. Elseviers et al., Shape coexistence in ^{180}Hg studied through the β decay of ^{180}Tl, *Phys. Rev. C*, 84:034307, Sep 2011.

[49] S. Sels et al., Shape staggering of midshell mercury isotopes from in-source laser spectroscopy compared with density-functional-theory and Monte Carlo shell-model calculations, *Phys. Rev. C*, 99:044306, Apr 2019.

[50] E. Coenen, K. Deneffe, M. Huyse, P. Van Duppen, and J. L. Wood, α Decay of Neutron-Deficient Odd Bi Nuclei: Shell-Model Intruder States in Tl and Bi Isotopes, *Phys. Rev. Lett.*, 54:1783–1786, Apr 1985.

[51] P. Van Duppen, P. Decrock, P. Dendooven, M. Huyse, G. Reusen, and J. Wauters, Intruder states in odd-odd Tl nuclei populated in the α-decay of odd-odd Bi isotopes, *Nuclear Physics A*, 529:268–288, 07 1991.

[52] A. N. Andreyev et al., Shape-changing particle decays of ^{185}Bi and structure of the lightest odd-mass Bi isotopes, *Phys. Rev. C*, 69:054308, May 2004.

[53] J. Wauters et al., Fine structure in the α decay of ^{189}Bi, *Phys. Rev. C*, 55:1192–1196, Mar 1997.

[54] C. N. Davids et al., Proton Decay of an Intruder State in ^{185}Bi, *Phys. Rev. Lett.*, 76:592–595, Jan 1996.

[55] M. Muikku et al., Shape coexistence in ^{183}Tl, *Phys. Rev. C*, 64:044308, Sep 2001.

[56] P. Campbell, J.A. Behr, J. Billowes, G. Gwinner, G.D. Sprouse, and F. Xu, Magnetic dipole and electric quadrupole moments of the neutron-deficient bismuth isotopes, *Nuclear Physics A*, 598(1):61 – 81, 1996.

[57] P. Campbell, J. Billowes, J.A. Behr, G. Gwinner, G.D. Sprouse, and F. Xu, Isotope shifts of the neutron-deficient bismuth isotopes: charge radii systematics across the Z = 82 shell closure, *Physics Letters B*, 346(1):21 – 26, 1995.

[58] M R Pearson, P Campbell, K Leerungnavarat, J Billowes, I S Grant, M Keim, J Kilgallon, I D Moore, R Neugart, M Neuroth, S Wilbert, and the ISOLDE Collaboration, Nuclear moments and charge radii of bismuth isotopes, *Journal of Physics G: Nuclear and Particle Physics*, 26(12):1829–1848, nov 2000.

[59] CERN website: Accelerators and Technology Sector. (https://espace.cern.ch/acctec-sector/default.aspx). Accessed: 18/03/2019.

[60] Erich Kugler, The ISOLDE facility, *Hyperfine Interactions*, 129(1):23–42, Dec 2000.

[61] ISOLDE website:. http://isolde.web.cern.ch. Accessed: 18/03/2019.

[62] B.A. Marsh et al., New developments of the in-source spectroscopy method at RILIS/ISOLDE, *Nuclear Instruments and Methods in Physics Research Section B: Beam Interactions with Materials and Atoms*, 317:550 – 556, 2013. XVIth International Conference on ElectroMagnetic Isotope Separators and Techniques Related to their Applications, December 2–7, 2012 at Matsue, Japan.

[63] U. Köster, How to produce intense and pure ISOL beams, *Progress in Particle and Nuclear Physics*, 46(1):411 – 412, 2001.

[64] U Köster, V.N Fedoseyev, and V.I Mishin, Resonant laser ionization of radioactive atoms, *Spectrochimica Acta Part B: Atomic Spectroscopy*, 58(6):1047 – 1068, 2003. LAP-2002 INTERNATIONAL CONFERENCE ON LASER PROBING.

[65] S. Rothe et al., Laser ion beam production at CERN-ISOLDE: New features – More possibilities, *Nuclear Instruments and Methods in Physics Research Section B: Beam Interactions with Materials and Atoms*, 376:91 – 96, 2016. Proceedings of the XVIIth International Conference on Electromagnetic Isotope Separators and Related Topics (EMIS2015), Grand Rapids, MI, U.S.A., 11-15 May 2015.

[66] V.I. Mishin et al., Chemically selective laser ion-source for the CERN-ISOLDE on-line mass separator facility, *Nuclear Instruments and Methods in Physics Research Section B: Beam Interactions with Materials and Atoms*, 73(4):550 – 560, 1993.

[67] Bruce Marsh. In-Source Laser Resonance Ionization at ISOL Facilities, Feb 2007. Presented 14 Mar 2007.

[68] M.J.G. Borge, Highlights of the ISOLDE facility and the HIE-ISOLDE project, *Nuclear Instruments and Methods in Physics Research Section B: Beam Interactions with Materials and Atoms*, 376:408 – 412, 2016. Proceedings of the XVIIth International Conference on Electromagnetic Isotope Separators and Related Topics (EMIS2015), Grand Rapids, MI, U.S.A., 11-15 May 2015.

[69] L. Ghys et al., α-decay properties of ^{200,202}Fr, *Phys. Rev. C*, 100:054310, Nov 2019.

[70] B. Lommel, D. Gembalies-Datz, W. Hartmann, S. Hofmann, B. Kindler, J. Klemm, J. Kojouharova, and J. Steiner, Improvement of the target durability for heavy-element production, *Nuclear Instruments and Methods in Physics Research Section A: Accelerators, Spectrometers, Detectors and Associated Equipment*, 480(1):16 – 21, 2002. Targets for Particle Beams: Preparation and Use. Proceedings of t he 20th World Conference of the International Nuclear Target Development Society.

[71] R.N. Wolf and othersr, ISOLTRAP's multi-reflection time-of-flight mass separator/spectrometer, *International Journal of Mass Spectrometry*, 349-350:123 – 133, 2013.

[72] A. E. Barzakh et al., Shape coexistence in ^{187}Au studied by laser spectroscopy, *Phys. Rev. C*, 101:064321, Jun 2020.

[73] S. Rothe, V.N. Fedosseev, T. Kron, B.A. Marsh, R.E. Rossel, and K.D.A. Wendt, Narrow linewidth operation of the RILIS Titanium: Sapphire laser at ISOLDE/CERN, *Nuclear Instruments and Methods in Physics Research Section B: Beam Interactions with Materials and Atoms*, 317:561 – 564, 2013. XVIth International Conference on ElectroMagnetic Isotope Separators and Techniques Related to their Applications, December 2–7, 2012 at Matsue, Japan.

[74] R.E. Rossel et al., Data acquisition, remote control and equipment monitoring for ISOLDE RILIS, *Nuclear Instruments and Methods in Physics Research Section B: Beam Interactions with Materials and Atoms*, 317:557 – 560, 2013. XVIth International Conference on ElectroMagnetic Isotope Separators and Techniques Related to their Applications, December 2–7, 2012 at Matsue, Japan.

[75] X-ray Instruments Association. X-ray Instruments Associates. (http://www.xia.com). Accessed: 15/03/2019.

[76] Wavemetrics. IGOR software package from wavemetrics. (https://www.wavemetrics.com/). Accessed: 15/03/2019.

[77] A. Rytz, Recommended energy and intensity values of alpha particles from radioactive decay, *Atomic Data and Nuclear Data Tables*, 47(2):205 – 239, 1991.

[78] H. Kettunen, T. Enqvist, M. Leino, K. Eskola, P.T. Greenlees, K. Helariutta, P. Jones, R. Julin, S. Juutinen, H. Kankaanpää, H. Koivisto, P. Kuusiniemi, M. Muikku, P. Nieminen, P. Rahkila, and J. Uusitalo, Investigations into the alpha-decay of 195At, *The European Physical Journal A - Hadrons and Nuclei*, 16(4):457–467, Apr 2003.

[79] V.R. Vanin, N.L. Maidana, R.M. Castro, E. Achterberg, O.A. Capurro, and G.V. Martí, Nuclear Data Sheets for A = 191, *Nuclear Data Sheets*, 108(11):2393 – 2588, 2007.

[80] H. Kettunen et al., Alpha-decay studies of the new isotopes ^{191}At and ^{193}At, *The European Physical Journal A - Hadrons and Nuclei*, 17(4):537–558, Aug 2003.

[81] A. N. Andreyev et al., α-decay spectroscopy of light odd-odd Bi isotopes - I: 188,190Bi nuclei, *The European Physical Journal A - Hadrons and Nuclei*, 18(1):39–54, Oct 2003.

[82] A. N. Andreyev, S. Antalic, D. Ackermann, S. Franchoo, F. P. Heßberger, S. Hofmann, M. Huyse, I. Kojouharov, B. Kindler, P. Kuusiniemi, S. R. Lesher, B. Lommel, R. Mann, G. Münzenberg, K. Nishio, R. D. Page, J. J. Ressler, B. Streicher, S. Saro, B. Sulignano, P. Van Duppen, and D. R. Wiseman, α-decay spectroscopy of the new isotope ^{192}At, *Phys. Rev. C*, 73:024317, Feb 2006.

[83] A. N. Andreyev et al., α-decay of the new isotope ^{187}po: probing prolate structures beyond the neutron mid-shell at n = 104, *Phys. Rev. C*, 73:044324, Apr 2006.

[84] Rene Brun and Fons Rademakers, ROOT — An object oriented data analysis framework, *Nuclear Instruments and Methods in Physics Research Section A: Accelerators, Spectrometers, Detectors and Associated Equipment*, 389(1):81 – 86, 1997. New Computing Techniques in Physics Research V.

[85] W. Gins and R.P. de Groote and M.L. Bissell and C. Granados Buitrago and R. Ferrer and K.M. Lynch and G. Neyens and S. Sels, Analysis of counting data: Development of the SATLAS Python package, *Computer Physics Communications*, 222:286 – 294, 2018.

[86] W. H. King and M. Wilson, Isotope shifts in lead: mass shifts and the odd-even effect, *Journal of Physics G: Nuclear Physics*, 11(3):43–45, mar 1985.

[87] B. Cheal, T. E. Cocolios, and S. Fritzsche, Laser spectroscopy of radioactive isotopes: Role and limitations of accurate isotope-shift calculations, *Phys. Rev. A*, 86:042501, Oct 2012.

[88] W. D. Myers and K. H. Schmidt, Update on droplet-model charge distributions, *Nucl. Phys. A; (Netherlands)*, 410:1, Nov 1983.

[89] S. RAMAN, C.W. NESTOR, and P. TIKKANEN, TRANSITION PROBABILITY FROM THE GROUND TO THE FIRST-EXCITED 2+ STATE OF EVEN–EVEN NUCLIDES, *Atomic Data and Nuclear Data Tables*, 78(1):1 – 128, 2001.

[90] H. De Witte et al., Nuclear Charge Radii of Neutron-Deficient Lead Isotopes Beyond $N = 104$ Midshell Investigated by In-Source Laser Spectroscopy, *Phys. Rev. Lett.*, 98:112502, Mar 2007.

[91] M. Anselment, W. Faubel, S. Göring, A. Hanser, G. Meisel, H. Rebel, and G. Schatz, The odd-even staggering of the nuclear charge radii of Pb isotopes, *Nuclear Physics A*, 451(3):471 – 480, 1986.

[92] U. Dinger, J. Eberz, G. Huber, R. Menges, S. Schröder, R. Kirchner, O. Klepper, T. Kühl, D. Marx, and G. D. Sprouse, Nuclear moments and change in the charge-radii of neutron deficient lead isotopes, *Zeitschrift für Physik A Atomic Nuclei*, 328(2):253–254, Jun 1987.

[93] S. B. Dutta, R. Kirchner, O. Klepper, T. U. Kühl, D. Marx, G. D. Sprouse, R. Menges, U. Dinger, G. Huber, and S. Schröder, Measurement of isotope shift and hyperfine splitting of ^{190,191,193,197}Pb isotopes by collinear laser spectroscopy, *Zeitschrift für Physik A Hadrons and Nuclei*, 341(1):39–45, Mar 1991.

[94] Th. Schmidt, Über die magnetischen Momente der Atomkerne, *Zeitschrift für Physik*, 106:358–361, May 1937.

[95] A. Arima, A short history of nuclear magnetic moments and GT transitions, *Science China: Physics, Mechanics and Astronomy*, 54:188–193, 01 2010.

[96] J.R. Persson, Table of hyperfine anomaly in atomic systems, *Atomic Data and Nuclear Data Tables*, 99(1):62 – 68, 2013.

[97] S. Schmidt et al., The nuclear magnetic moment of 208Bi and its relevance for a test of bound-state strong-field QED, *Physics Letters B*, 779:324 – 330, 2018.

[98] Yu Ting and Dudley Williams, Nuclear Gyromagnetic Ratios. IV, *Phys. Rev.*, 89:595–596, Feb 1953.

[99] T. Baştuğ, B. Fricke, M. Finkbeiner, and W.R. Johnson, The magnetic moment of ^{209}Bi, *Zeitschrift für Physik D Atoms, Molecules and Clusters*, 37:281–282, December 1996.

[100] A. Arima and H. Horie, Configuration Mixing and Magnetic Moments of Odd Nuclei, *Progress of Theoretical Physics*, 12(5):623–641, 11 1954.

[101] N.J. Stone, Table of nuclear magnetic dipole and electric quadrupole moments, *Atomic Data and Nuclear Data Tables*, 90(1):75 – 176, 2005.

[102] A. Voss et al., Nuclear moments and charge radii of neutron-deficient francium isotopes and isomers, *Phys. Rev. C*, 91:044307, Apr 2015.

[103] M. D. Seliverstov et al., Electromagnetic moments of odd-A $^{193-203,211}$Po isotopes, *Phys. Rev. C*, 89:034323, Mar 2014.

[104] M. Seliverstov et al., In-source laser photoionization spectroscopy of Bi isotopes: accuracy of the technique and methods of data analysis, *Hyperfine Interactions*, 241, 12 2020.

[105] Robert J. Hull and Gilbert O. Brink, Hyperfine Structure of ^{209}Bi, *Phys. Rev. A*, 1:685–693, Mar 1970.

[106] Tiago Quevedo Teodoro and Roberto Luiz Andrade Haiduke, Nuclear electric quadrupole moment of bismuth from the molecular method, *Phys. Rev. A*, 88:052504, Nov 2013.

[107] G. Neyens, S. Ternier, N. Coulier, K. Vyvey, R. Coussement, and D.L. Balabanski, Influence of particle-core coupling on the quadrupole moment of 8+ isomers in even-even Po isotopes, *Nuclear Physics A*, 625(3):668 – 674, 1997.

[108] A. Coc et al., Hyperfine structures and isotope shifts of 207–213,220–228Fr; Possible evidence of octupolar deformation, *Physics Letters B*, 163(1):66 – 70, 1985.

[109] T.E. Cocolios et al., The Collinear Resonance Ionization Spectroscopy (CRIS) experimental setup at CERN-ISOLDE, *Nuclear Instruments and Methods in Physics Research Section B: Beam Interactions with Materials and Atoms*, 317:565 – 569, 2013. XVIth International Conference on ElectroMagnetic Isotope Separators and Techniques Related to their Applications, December 2–7, 2012 at Matsue, Japan.

[110] T.E. Cocolios et al., High-resolution laser spectroscopy with the Collinear Resonance Ionisation Spectroscopy (CRIS) experiment at CERN-ISOLDE, *Nuclear Instruments and Methods in Physics Research Section B: Beam Interactions with Materials and Atoms*, 376:284 – 287, 2016. Proceedings of the XVIIth International Conference on Electromagnetic Isotope Separators and Related Topics (EMIS2015), Grand Rapids, MI, U.S.A., 11-15 May 2015.